RUPRECHT-KARLS-UNIVERSITÄT HEIDELBERG

Eva Hennekemper

Simulation and Calibration of the Specific Energy Loss of the Central Jet Chambers of the H1 Detector and Measurement of the Inclusive $D^{*\pm}$ Meson Cross Section in Photoproduction at HERA

Dissertation

HD-KIP-11-68

KIRCHHOFF-INSTITUT FÜR PHYSIK

INAUGURAL - DISSERTATION

zur
Erlangung der Doktorwürde
der
Naturwissenschaftlich - Mathematischen
Gesamtfakultät
der Ruprecht - Karls - Universität
Heidelberg

vorgelegt von
Dipl.-Phys. Eva Hennekemper
aus Dortmund (Nordrhein - Westfalen)
Tag der mündlichen Prüfung: 06. Juli 2011

Simulation and Calibration of the Specific Energy Loss of the Central Jet Chambers of the H1 Detector
and
Measurement of the Inclusive $D^{*\pm}$ Meson Cross Section in Photoproduction at HERA

Gutachter: Prof. Dr. Hans-Christian Schultz-Coulon
Prof. Dr. André Schöning

Kurzfassung

In dieser Arbeit wird die Photoproduktion von D^*–Mesonen in ep–Kollisionen bei HERA untersucht. Die D^*–Mesonen werden anhand ihres 'goldenen' Zerfalls $D^* \rightarrow K\pi\pi_s$ mit dem H1–Detektor nachgewiesen. Gegenüber früheren Analysen konnte der systematische Fehler durch zwei wesentliche Verbesserungen verringert werden. Zum einen ermöglicht die Simulation des Fast Track Trigger, der auf Spuren in den zentralen Spurkammern basiert, eine korrekte Berücksichtigung der Abhängigkeiten der Triggereffizienz von unterschiedlichen kinematischen Grössen. Zum anderen erlaubt die Verwendung des spezifischen Energieverlusts eine bessere Unterdrückung von nicht–resonantem Untergrund. Um die Teilchenidentifikation anhand des spezifischen Energieverlustes in der Analyse verwenden zu können, wurde die Simulation des Energieverlustes in den Spurkammern des H1–Experiments verbessert und die notwendigen Korrekturfunktionen und Kalibrationen bestimmt. Mit dieser verbesserten H1–Detektorsimulation wird der Wirkungsquerschnitt der Photoproduktion von D^* –Mesonen in den HERAII Daten bestimmt. Die Daten ensprechen einer integrierten Luminosität von $113\,\mathrm{pb}^{-1}$. Die Messung erfolgt im kinematischen Bereich von $Q^2 < 2\,\mathrm{GeV}$ für Photon–Virtualitäten und Photon–Proton Schwerpunktsenergien von $100 < W_{\gamma p} < 285\,\mathrm{GeV}$. Einfach und doppelt differenziellen Wirkungsquerschnitte von D^*–Mesonen mit Transversalimpulsen $p_T(D^*) > 1.8\,\mathrm{GeV}$ und im Bereich zentraler Pseudorapiditäten $|\eta(D^*)\ | < 1.5$ werden bestimmt und perturbativen QCD Vorhersagen in führender und nächstführender Ordnung gegenübergestellt.

Abstract

In this thesis the photoproduction of D^* mesons in ep collisions at HERA is analysed. D^* mesons are detected in the 'golden' decay channel $D^* \rightarrow K\pi\pi_s$ with the H1 detector. Compared to earlier analyses, the systematic uncertainty is reduced due to two main improvements. Firstly, the simulation of the Fast Track Trigger, which is based on tracks measured within the central jet chambers, allows the trigger efficiency dependence of various kinematic variables to be evaluated. Secondly, the use of specific energy loss provides the possibility to suppress the non–resonant background. In order to use particle identification with the specific energy loss in the analysis, the simulation of the specific energy loss in the central jet chambers of the H1 detector is improved and the necessary correction functions and calibrations have been determined. This improved final H1 detector simulation is used to determine the cross section of photoproduction of D^* mesons in the HERA II data sample, which corresponds to an integrated luminosity of $113\,\mathrm{pb}^{-1}$. The measurement was performed in the kinematic region of $Q^2 < 2\,\mathrm{GeV}$ for the photon virtuality and photon-proton center of mass energies of $100 < W_{\gamma p} < 285\,\mathrm{GeV}$. Single and double differential cross sections of D^* mesons with transverse momenta above $1.8\,\mathrm{GeV}$ and in the central pseudorapidity range of $|\eta(D^*)| < 1.5$ are determined and are compared to leading and next to leading order QCD predictions.

Contents

Chapter 1

Introduction

In the so called 'Standard Model' (SM) of particle physics, leptons and quarks are grouped into three families. Matter is composed of in total six leptons, the electron, the muon and the tau and the corresponding neutrinos, and six quark flavours, up, down, charm, strange, beauty and top. In addition each particle has a corresponding anti–particle with the same mass and lifetime but opposite charge sign. Hadrons, like protons, are composed of quarks.

The interactions between particles are explained with the electromagnetic, the weak, and the strong forces. The forces are mediated by bosons: in an electromagnetic interaction a photon is exchanged, in weak interactions Z or W bosons and the strong interaction is mediated by gluons. The latter interaction is described successfully by the theory of Quantum–Chromo–Dynamics (QCD).

The HERA collider at DESY is used as a microscope to resolve the building blocks of nature. HERA was the world's first electron–proton collider, where the particles are accelerated and collided in a 6.3km long ring tunnel at a center of mass energy of $319\,\mathrm{GeV}$. The interaction products of the collisions were detected with the H1 experiment. The concept of colliding one fundamental particle with one composite object allows the study of the structure of that object. The HERA collider was in operation until summer 2007. With the HERA machine it was possible to study in high precision many properties of the SM. The measurement of structure functions and the extraction of the parton density functions of the proton provide the necessary knowledge for present high energy experiments like the Large Hadron Collider at CERN where two proton beams are brought into collision, currently at a center of mass energy of $7\,\mathrm{TeV}$.

In this thesis the photoproduction of charm quarks is studied. Photoproduction denotes that the electron is scattered under low angles after the electron proton collision, so that it is not detected within the H1 detector volume and that the exchanged photon in this process has low virtualities. The charm quark pairs are dominantly produced via the boson–gluon–fusion process, where a virtual photon from the electron interacts with a gluon from the proton.

The photoproduction of charm quarks is of particular interest because the heavy charm quark mass provides a hard scale such that it is feasible to apply perturbative QCD calculations. Hence with the experimental results of the measurement of charm quarks in photoproduction it is possible to test the current understanding of perturbative QCD.

Motivation

The use of particle identification with the specific energy loss of particles in material is an elegant method to suppress background, but it requires a good description of the data by the simulation. The Monte Carlo (MC) events have to be generated properly and in addition a detector simulation is needed. The earlier simulation of the specific energy loss in the H1 detector showed discrepancies in the data description, mainly due to not considering the energy straggling in a gaseous absorber material in the required way.

In this thesis, one component of the H1 detector simulation, the simulation of the specific energy loss in the central jet chambers, was studied and simulated anew. The new simulation now takes into account the thickness of the absorber material in an improved way, with the implementation of four different energy straggling models each valid for certain absorber material conditions.

However, the specific energy loss information cannot be used for particle identification directly, because the main detector effects are simulated too. The energy loss simulation needs to be calibrated and corrected for these detector effects. The neccessary correction functions and calibrations have been determined in this thesis.

The measurement of the specific energy loss in data was already studied and calibrated [1]. Since data and MC agree well with the new simulation, the specific energy loss simulation in the central jet chambers was included to the H1 simulation sofware and provides the possibility to use particle identification in the track reconstruction. Particle identification is an important tool in the analysis of heavy quark production, where a large background suppression factor is needed. Examples are the measurement of D^* mesons in photoproduction which is studied in this thesis, or in the measurement of beauty photoproduction using di-electron events [2]. The latter analysis benefits from the new possibility of electron identification with the specific energy loss information, where the background is reduced significantly and a higher rejection is achieved.

In this thesis charm production is studied with the measurement of inclusive cross sections of D^* mesons in photoproduction. Charm quarks are produced in boson–gluon–fusion and fragment into the charmed D^* meson. Here D^* mesons are identified in the so called golden decay channel $D^{*\pm} \rightarrow D^0\pi^\pm_{slow} \rightarrow K^\mp\pi^\pm\pi^\pm_{slow}$. The event selection is performed with the Fast Track Trigger of the H1 detector. Low virtualities, $Q^2 < 2\,\mathrm{GeV}^2$, of the exchanged photon define the photoproduction region of charm production. D^* mesons are measured with transverse momenta above $1.8\,\mathrm{GeV}$ and in the central pseudorapidity range of $|\eta(D^*)| < 1.5$.

With this analysis it is possible to test leading order (LO) and next to leading order (NLO) predictions of perturbative QCD (pQCD), because the high mass of the charm quark provides a hard scale. Furthermore it is possible with this new measurement to investigate phase space regions where previous measurements of inclusive D^* mesons in photoproduction by the H1 [3] and ZEUS collaborations claim to observe discrepancies compared to pQCD predictions. The latest ZEUS publication [4] exhibits an excess in the double differential cross sections in transverse momenta and pseudorapidity of the D^* meson in the forward region of the detector in the highest analysed p_T bin, shown in figure 1.1a).

This excess was not found in the latest H1 publication [7], but this analysis has limited statistics. A recent analysis of inclusive D^* mesons in photoproduction of the HERA II run period was presented at the DIS conference in 2008 [3]. Here a factor eight in statistics compared to the earlier analysis was gained. The excess in the forward region is still observed, see figure 1.1 b).
In this thesis the improved final H1 detector simulation and reconstruction is used for analysing the photoproduction of D^* mesons in the HERA II data anew. This includes the benefit of an improved track reconstruction and particle identification with the specific energy loss measurement as well as the final Fast Track Trigger simulation.

In the analysis of D^* mesons in photoproduction a huge amount of non–resonant background is present at the D^* meson signal extraction. This non–resonant background can be significantly reduced with the usage of specific energy loss information of the decay particles of the D^* meson. In the previous analysis the background reduction was only possible with hard cuts on other quantities which results in a source of systematic uncertainty.
One of the dominant systematic uncertainties of the previous analysis was due to the trigger efficiency. Several studies of the trigger efficiency have been performed to reduce the systematic error. In addition it was assumed in the previous analysis that the trigger efficiency depends only on the transverse momentum of the D^* meson. The trigger efficiency will be presented in

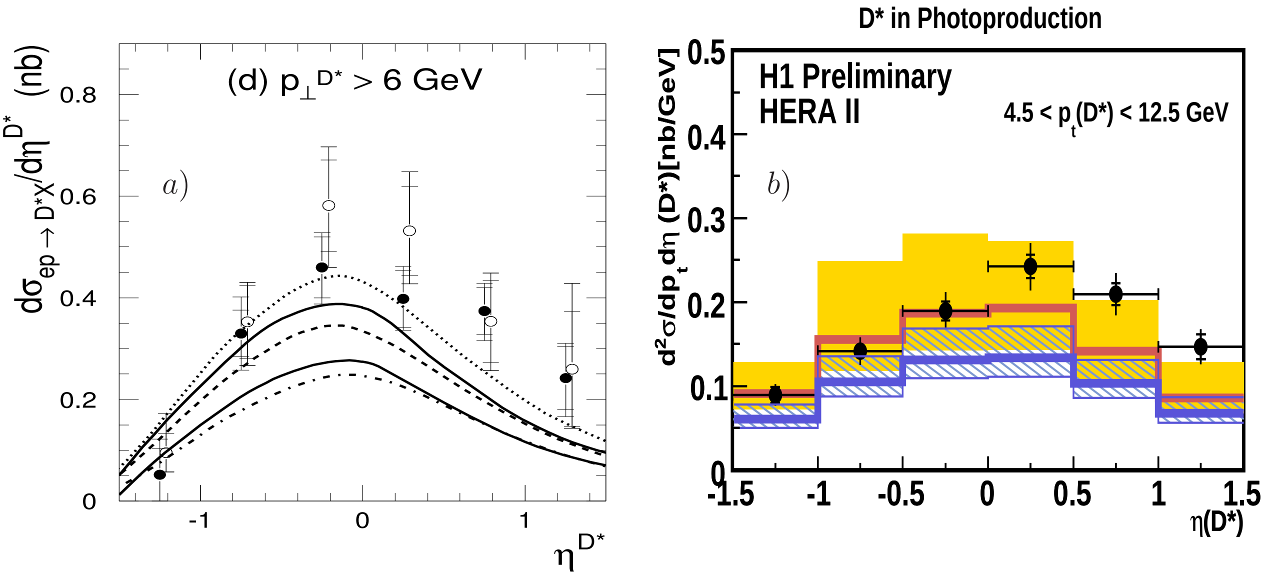

Figure 1.1: *In a) the differential cross section as a function of the pseudorapidity in the highest p_T bin for D^* mesons in photoproduction of the ZEUS publication [4] is shown. Open circles refer to the decay channel $D^* \rightarrow (K\pi\pi\pi)\pi_s$ and full dots for $D^* \rightarrow (K\pi)\pi_s$. The cross sections are compared to next to leading order QCD predictions by the massive charm approach (dash–dotted, dashed and dotted lines) and by the massless approach of [5] (upper curve) and [6] (lower curve). In b) the double differential cross section in pseudorapidity in the highest p_T bin of the H1 preliminary result [3] is presented. In addition the next to leading order predictions by the massive approach (yellow curve and uncertainty band) and by the general mass variable flavor number scheme (blue curve and uncertainty band) are shown.*

this thesis and it shows that this is not the case. In the present analysis the simulation of the Fast Track Trigger is used which allows to consider the dependence of the trigger efficiency on various kinematic variables.

Outline of the Thesis

The kinematics of the electron–proton scattering and more precisely the theory of photoproduction of charm quarks at the HERA collider is introduced in chapter 2. Chapter 3 gives an overview of the HERA machine and the H1 detector. The main detector components used in the present thesis are presented.

Chapter 4 deals with the simulation of the specific energy loss in the central jet chambers of the H1 detector. First a general description of the H1 detector simulation is given. Then properties of the the new simulation of the specific energy loss developed in this thesis are discussed. The calibration of the new simulation and the determination of all corrections needed to consider the simulated detector effects is presented in chapter 5.

The final H1 detector simulation software has major changes in the particle identification with the central jet chambers and uses this information in the tracking. It is used in the following chapters for analysing the HERA II data of D^* mesons in photoproduction anew with the intent to reduce the systematic uncertainties. In chapter 6 the leading order MC generators used in this analysis and next to leading order calculations are introduced. The reconstruction of D^* mesons and the signal extraction is described in chapter 7. Here the particle identification is used to reduce the amount of combinatorial background. The final event selection is presented in chapter 8. The data events are compared in chapter 9 to the detector simulation with control distributions. The trigger efficiency is studied in chapter 10. The detector effects which have to be considered for the cross section measurement together with a detailed presentation of all systematic uncertainties of this analysis are discussed in chapter 11. In the chapter 12 the resulting single and double differential cross sections in comparison to leading order and next to leading order QCD predictions are shown. In addition, the cross section results are compared to the earlier H1 publication of D^* mesons in photoproduction.

Chapter 2

D^* Mesons in Photoproduction in ep Scattering

In collisions of electrons and protons at the HERA collider charm quarks are produced. In this chapter an overview of the theory of D^* mesons in photoproduction is given. In the first part, the physics of electron–proton scattering is introduced and the kinematic variables are defined. Then the basic concepts of QCD are briefly summarized and the production mechanism of charm quarks at HERA is described. In the last section of this chapter the fragmentation of the produced charm quark into the detectable charmed D^* meson is discussed.

2.1 Electron–Proton Scattering

Electron–proton interactions in high energy collisions at the electron[1] proton collider HERA can be described via the exchange of virtual gauge bosons of the electromagnetic or weak force. Figure 2.1 displays the Feynman diagrams of the neutral and charged current processes where the incoming electron with four–momentum k scatters with a proton with four–momentum P. The variable q denotes the transfered momentum from the lepton to the proton. The outgoing electron carries the four-momentum k'.

In neutral current (NC) events, $ep \to e'X$, a photon γ or Z^0 boson is exchanged, figure 2.1 a), whereas in charged current events (CC), $ep \to \nu_e X$, the exchanged particle is a charged $W^\pm$ boson, and in the final state a neutrino is found, figure 2.1 b).

2.2 Kinematics

Three Lorentz invariant kinematic variables are used to describe the the electron–proton scattering process $e + p \to e(\nu_e) + X$: the negative four–momentum transfer squared Q^2, the

---

[1] In the following the term ’electron’ refers to positron and electron.

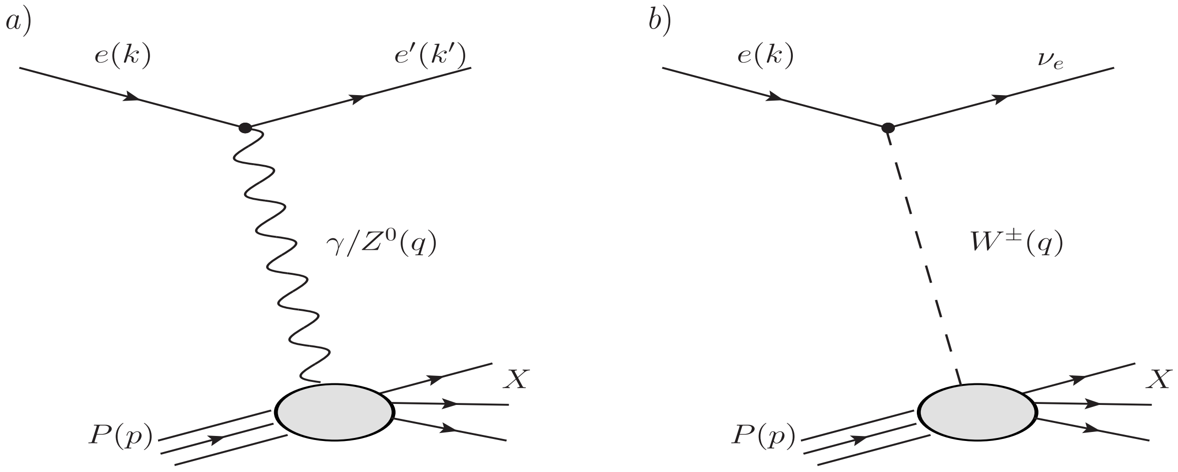

Figure 2.1: *Leading order Feynman diagrams for electron proton scattering for a) neutral current process and b) charged current processes. The quantities in brackets denote the four–momenta of the particles.*

dimensionless scaling variable Bjorken x and the inelasticity y.
Q^2 is defined as

$$Q^2 := -q^2 = -(k - k')^2, \tag{2.1}$$

with the four–momenta of the ingoing and the scattered lepton. If the exchanged gauge boson is a photon, Q^2 corresponds to the virtuality of the exchanged photon. The relative energy loss of the scattered lepton in the proton rest frame is measured with the inelasticity y

$$y := \frac{(p \cdot q)}{(p \cdot k)}, \quad 0 < y < 1. \tag{2.2}$$

The Bjorken variable x is defined as

$$x := \frac{Q^2}{2(p \cdot q)}, \quad 0 < x < 1. \tag{2.3}$$

In the Quark Parton Model [8], more details in section 2.3, the variable x represents the fractional momentum of the proton which is carried by the struck quark.
The definition of the center of mass energy is given by the square root of the Mandelstam variable s

$$s := (k + p)^2. \tag{2.4}$$

For the HERA collider with beam energies of $E_e = 27.5\,\mathrm{GeV}$ and $E_p = 920\,\mathrm{GeV}$, where E_e is the electron beam and E_p is the proton beam, and neglecting the particle masses the center of mass energy is $\sqrt{s} = \sqrt{4 \cdot E_e \cdot E_p} = 319\,\mathrm{GeV}$.

The negative four–momentum transfer squared can be calculated, with again neglecting the rest masses of the particles, with the kinematic variables s, x and y as

$$Q^2 = sxy. \tag{2.5}$$

The center of mass energy of the photon–proton system is defined as

$$W_{\gamma p}^2 = (q+P)^2 = y \cdot s - Q^2 \simeq y \cdot s \tag{2.6}$$

with the four momentum P of the proton and q the four momentum of the photon. At HERA with center of mass energies of $\sqrt{s} \sim 320\,\mathrm{GeV}$ and at low virtualities, Q^2 is negligible for the calculation of $W_{\gamma p}$.

Photoproduction

The scattering processes at HERA can be divided with respect to their virtualities into two kinematic regimes: the photoproduction and the deep inelastic scattering (DIS) regime. The scattered electron of the ep scattering process is used to clearly distinguish the two regions.
In the DIS regime the scattered electron is measured within the detector whereas in photoproduction the electron is not detected because it is scattered into the beam pipe and escapes detection. Hence the acceptance of the H1 detector defines the corresponding virtuallity regions of DIS $2 < Q^2 < 1000\,\mathrm{GeV}^2$ and photoproduction $0 < Q^2 < 2\,\mathrm{GeV}^2$.
In general in ep scattering the exchanged particles are photons, Z^0 or $W^\pm$ bosons. However in photoproduction the four–momentum transfer is too low to produce bosons of the weak force with sufficient probability, $-q^2 \ll m^2(W^\pm, Z^0)$, because Z^0 and $W^\pm$ bosons have high masses. Hence, in the scattering process dominantly photons are exchanged.

Further this low virtualities in photoproduction imply the exchange of a quasi real photon. In the equivalent photon approximation [9–11] the electron–proton interaction is approximated with a photon–proton interaction

$$\sigma_{ep} = \int_{y_{min}}^{y_{max}} dy \int_{Q^2_{min}}^{Q^2_{max}} dQ^2 f_\gamma(y, Q^2) \sigma_{\gamma\ p}, \tag{2.7}$$

with the flux of photons $f_\gamma(y, Q^2)$ originating from the electron and the photon–proton cross section $\sigma_{\gamma p}$. The flux is depending on the energy fraction y of the electron energy which is carried by the photon,

$$f_\gamma(y, Q^2) = \frac{\alpha}{2\pi y Q^2}\left(1 + (1-y)^2 - 2m_e \frac{y^2}{Q^2}\right). \tag{2.8}$$

The ep cross section is proportional to $1/Q^4$. This implies a dominance of the photoproduction over the DIS part of the cross section.

2.3 QCD Models, Factorisation and Parton Evolution

Data from early ep scattering experiments were well described by the naive quark parton model [8]. The constituents of the proton are point-like, spin $1/2$ particles which were later identified with the quarks from QCD. The partons are not allowed to interact. The proton structure is parametrized by so–called structure functions, $F_1(x)$ and $F_2(x)$, which depend only on the scaling variable x. The deep–inelastic ep scattering is the elastic scattering on one of the partons.
However, it was expected in the naive quark parton model that the structure functions depend only on x and not on Q^2, further experimental results, e.g. the scaling violation which shows the additional Q^2 dependence of the structure functions, revealed that this picture is incomplete. Today the gauge field theory of QCD is used to describe high energy collisions. Here each quark carries a color charge. The strong force between the quarks is exchanged via gluons, which are massless bosons. The gluons carry themselves color so that gluons can interact with gluons. They can radiate themselves gluons ($g \rightarrow gg$) or split into quark-antiquark pairs ($g \rightarrow q\bar{q}$). In contrast to the naive quark parton model, where the quarks the constituents of the proton are described as static, in QCD the constituents are allowed to interact via the radiation of gluons. The interaction between two particles is described with the strong coupling constant α_s, which will be discussed in the next section.

The cross section of the neutral current process (see 2.1 a)) in the Born approximation[2] neglecting the contributions from W and Z exchange is defined as [12]

$$\frac{d^2\sigma^{NC}_{Born}}{dxdQ^2} = \frac{2\pi\alpha^2_{em}}{xQ^4} \cdot \left[(1+(1-y)^2) \cdot F_2(x,Q^2) - y^2 \cdot F_L(x,Q^2)\right], \tag{2.9}$$

where α_{em} denotes the electromagnetic coupling constant. The structure function F_2 and the longitudinal structure function F_L are related via the structure function F_1

$$F_2(x,Q^2) - 2x \cdot F_1(x,Q^2) = F_L(x,Q^2). \tag{2.10}$$

The longitudinal structure function takes into account that the exchanged photon can have in addition to the transverse polarizations also a longitudinally polarization[3]. It has only contributions for very large inelasticities y. A recent H1 measurement of the structure function F_2 is given in [13], and for F_L in [14].

The strong coupling constant

During the calculation of gluon radiation and splitting processes in perturbative QCD divergences, the ultraviolet divergences and the collinear divergences, occur. The origin of these divergences and their treatment will be presented in the following.
In quantum field theories like QED and QCD infinities occur during the calculation of interactions. The momenta of the virtual particles in closed fermion loops in QED or gluon loops in QCD are not restricted by conservation laws. This results in divergent integrals of the form

---

[2] This denotes the one boson exchange.

[3] In the naive parton model the longitudinal structure function is zero.

$\int dp/p$, where p is the momentum of the particles in the loop and hence introduce logarithmic divergences, for a more detailed explanation see e.g. [15]. The divergent integrals can be handled with the renormalization method: These so called ultraviolet divergences are solved in the running of the strong coupling constant α_s. Therefore the α_s dependence on the renormalization scale parameter μ_r is introduced. In case $\mu_r \gg \Lambda_{QCD}$, where Λ_{QCD} is the scale where the coupling becomes strong, α_s is small so that pQCD calculations diverge. At $\mu_r = \Lambda_{QCD}$ the strong coupling diverges.
Experimentally with measurements of α_s it is found that Λ_{QCD} is around $200\,\mathrm{MeV}$.
Neglecting the quark masses the renormalization group equations [4] give for the effective coupling constant

$$\mu_r^2 \cdot \frac{\partial \alpha_s(\mu_r)}{\partial \mu_r^2} = \beta(\alpha_s(\mu_r)), \tag{2.11}$$

with the β-function $\beta(\alpha_s(\mu_r))$. This gives in the one loop approximation for the strong coupling

$$\alpha_s(\mu_r) = \frac{1}{\beta^0 \cdot ln(\mu_r^2/\Lambda_{QCD}^2)}, \tag{2.12}$$

with the first coefficient of the beta function $\beta^0 = \frac{33-2\cdot n_f}{12\pi}$, where n_f is the number of active flavors.
In deep inelastic scattering the relevant scale is Q^2 so that $\mu_r^2 = Q^2$. In heavy quark production the quark mass becomes relevant and usually $\mu_r^2 = Q^2 + m_{quark}^2$ is chosen.

For large scales with large μ_r it is possible to use perturbative QCD. In the limit $\mu_r^2 \to \infty$ the coupling between quarks and gluons becomes small, so that the quarks can be regarded as quasi–free particles. This behavior is known as asymptotic freedom.
For small scales ($\mu_r \to \Lambda_{QCD}$) the coupling becomes strong, so that free quarks are not observed but they are always bound as partons of the hadrons. This is known as confinement. The logarithm in the α_s formula goes to 1 and it is not possible to calculate perturbatively.

In deep–inelastic scattering pQCD calculations are applicable above $Q^2 \approx 3 - 4\,\mathrm{GeV}^2$. In photoproduction with low virtualities, Q^2 is not an adequate scale for pQCD calculations. Here possible scales for pQCD calculations are the transversal jet energy or for heavy quarks the high quark mass.

The collinear divergences arise from gluons which are emitted collinearly to the quark. Such gluon radiation and splitting of gluons into quarks can occur several times and are summarized in a parton ladder. The solution is to introduce a cut-off scale, the factorization scale μ_f, which divides the gluon ladder into a long distance (virtualities smaller than μ_f^2) and a short distance (virtualities greater than μ_f^2) regime.
At short distances it is possible to calculate in pQCD. The divergences in the long distance part are absorbed in parton density functions (PDFs) $f_i^p(x, \mu_f^2, \mu_r)$ which represent the probability of finding a parton i with a momentum fraction x of the proton momentum. They depend on the factorization scheme like the minimal substraction scheme ($\overline{MS}$) or DIS which was used. The $\overline{MS}$ scheme is the most common used factorization scheme of the PDF fitting groups (like

---

[4] For reference see e.g. [16]

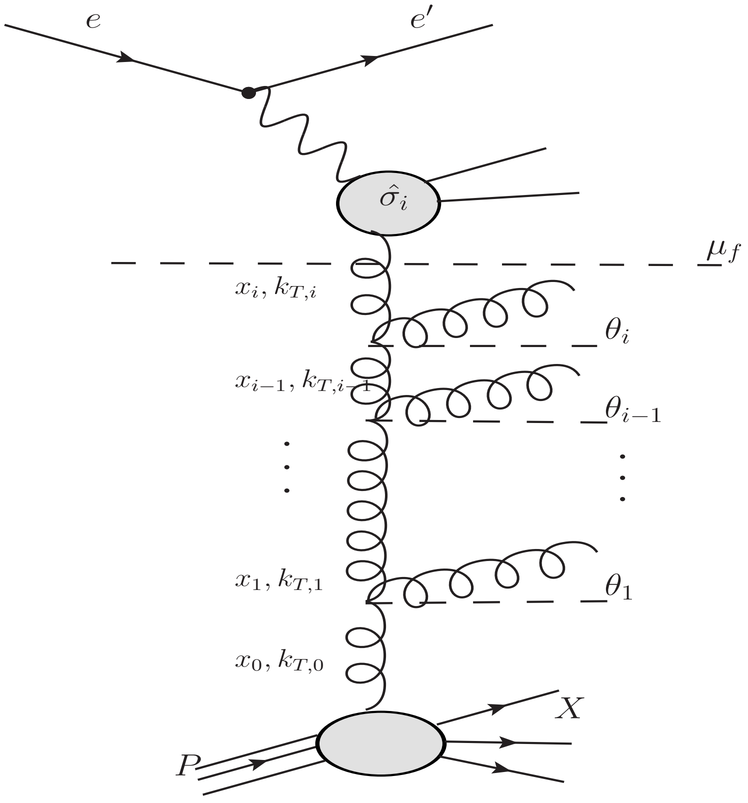

Figure 2.2: *The parton ladder summarising the gluon emission collinear to the quark is shown here. The factorisation scale μ_f is visualized which seperates the hard matrix element $\hat{\sigma}_i$ from the parton evolution. The gluons carry the longitudinal momenta x_i, the transverse momenta $k_{T,i}$ and are emitted under the angle θ_i.*

MSTW and CT). Usually $\mu_f^2 = Q^2$ is chosen. In figure 2.2 the parton ladder and the factorization ansatz is shown.

Parton density functions are not calculable in pQCD. In general two approaches exist to extract the PDFs at a starting scale Q_0 as a function of x from measurements of the function F_2 at e.g. HERA or fixed target experiments. On the one hand global fits of data are performed, e.g. by the CT or the MSTW groups. On the other hand pure DIS data is included in the fits, e.g. in the Alekhin and HERA PDF sets. The recent HERA PDFs, HERAPDF1.0 [17], are shown in figure 2.3. This figure shows that at small x the proton is dominated by gluons.

As long as α_s is small, it is possible to apply perturbative theory to predict PDFs at other scales with evolution equations. The evolution equations evolve the PDFs of quarks $q_i(x, Q^2)$ and gluons $g(x, Q^2)$ from the scale Q_0 to higher Q. Several appoaches of the evolution exist which are valid for different x and Q^2 regimes.

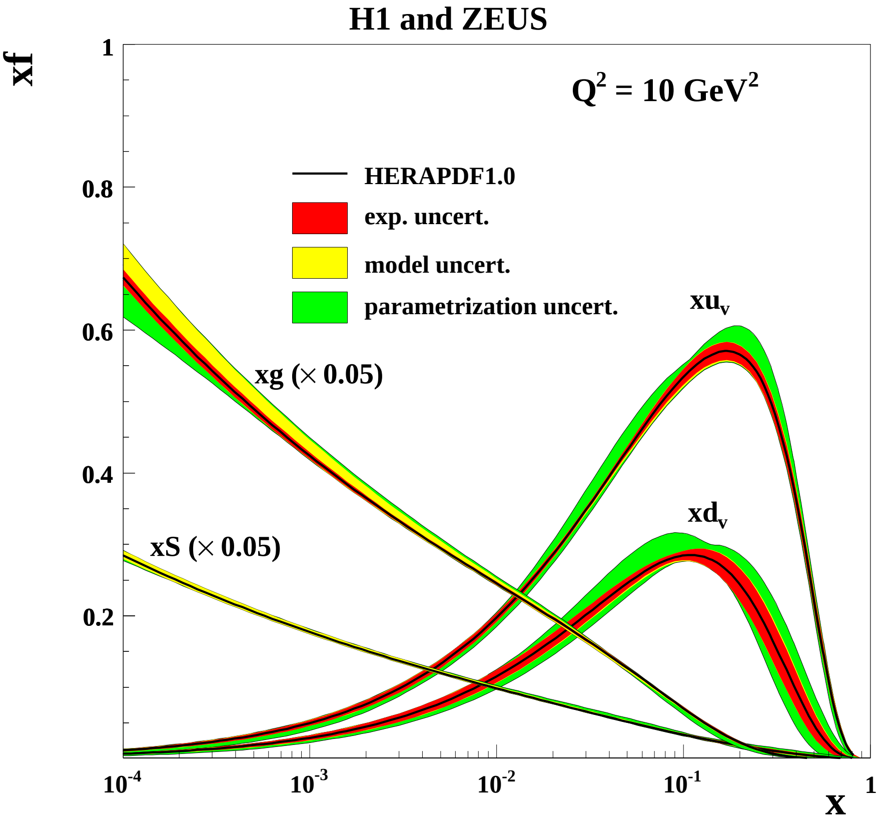

Figure 2.3: *The parton density function HERAPDF1.0 extracted from combined H1 and ZEUS inclusive deep inelastic scattering cross sections of neutral and charged current data [17].* xu_v *is the parton density distribution for u–valence quarks,* xd_v *for d–valence quarks,* xS *for sea quarks and* xg *for gluons.*

DGLAP

The parton evolution can be described with the DGLAP approach from Dokshitzer, Gribov, Lipatov and Altarelli, Parisi [18–22] which is also named collinear factorization. The transverse momenta k_T of the radiated gluons (see figure 2.2) are ordered, e.g. $k^2_{T,i-1} \ll k^2_{T,i}$. In addition the longitudinal momentum of the parton is softly ordered with $x_{i-1} < x_i$ and is restricted to be large compared to the transverse momentum k_T. The radiated partons are demanded to be radiated collinear to the incident ones. The resulting parton densities depend only on x and μ_f and not on k_T. At small x the restriction $x_i \gg k_{T,i}$ might be violated.

BFKL

At small x regimes where the DGLAP ansatz is not longer valid, the BFKL (Balitsky, Fadin, Kuraev, Lipatov) approach can be used [23, 24]. The longitudinal momenta of the emitted partons are ordered $x_i \ll x_{i-1}$ whereas the transverse momenta are not ordered and can be in the same order of magnitude as the longitudinal momenta. For the evolution in the small x regime only gluons have to be considered. In the BFKL evolution the k_T factorization is implemented: The gluon density function depends now on k_T, and the k_T of a parton can be comparable to the size of the transverse momentum of the hard subprocess. Thus it cannot longer be neglected. The BFKL approach does not describe the higher x regime so that it is not used during this analysis.

CCFM

In the CCFM (from Ciafolani, Catani, Fiorani and Marchesi) approach [25–28] the emission angles θ_i of the radiated partons are ordered $\theta_i > \theta_{i-1}$. As in BFKL only gluons are considered in the evolution and k_T factorization is implemented.
The ordering of the CCFM approach becomes similar to the DGLAP ordering in the regime of higher x and small emission angles, where the momentum fraction $x_i/x_{i-1} \sim 1$. However at small x the CCFM evolution results are closer to the BFKL evolution scheme which means a faster rise of the parton density distributions. The gluon density function depends on x, μ_f and on k_T.

With the measurement of structure functions [29, 30] it is possible to study the DGLAP scheme at HERA down to very low x values at around 10^{-4}. The expected DGLAP break down is not observed. In forward jet production indications were found that the DGLAP approach has deficiencies in special event topologies. In addition a better description of three- to four-jet production data at low x from H1 [31] is given by an unordered k_T approach than with DGLAP.

2.4 Photoproduction of Charm Quarks at HERA

In this thesis the charm quark production at HERA is analyzed. Charm quarks are produced in quark and antiquark pairs in open charm production. At HERA heavy quark production includes the production of charm and beauty quarks. The total cross section of charm quark production is two orders of magnitude higher as the total cross section for beauty quark production [32]. This can be explained with the higher mass and lower electric charge of the beauty quark, $m_b \approx 4.75\mathrm{GeV}$ and $q_b = 1/3$, than of the charm quark , $m_c \approx 1.5\,\mathrm{GeV}$ and $q_c = 2/3$. Top quark production is not possible at HERA energies.
In DIS a hard scale is given by the four-momentum transferred Q^2, but in photoproduction Q^2 is around zero, and so cannot be used as hard scale. The heavy quark masses fulfill $m_q \gg \Lambda_{QCD}$ such that the quark mass provides a hard scale and perturbative QCD calculations are possible. Therefore photoproduction of charm quarks provides a test of perturbative QCD. In practice usually in heavy quark production the transverse mass $m_t^2 = m_c^2 + (p_{t,c}^2 + p_{t,\bar{c}}^2)/2$ is used as hard scale where $p_{t,c(\bar{c})}^2$ is the transverse momentum of the charm or anticharm quark, respectively.

The leading order Feynman diagrams for charm production relevant for this analysis of charm quarks in photoproduction are shown in figure 2.4. In these processes the hadronic structure of the exchanged quasi real photon is considered. Before entering the hard interaction the photon can fluctuate into a quark-antiquark pair. The quarks can radiate gluons and in addition gluon splitting may occur. In this way the photon has a hadronic structure. The photon fluctuation causes two different types of processes the direct–photon process and the resolved–photon process. In the direct process the photon from the beam lepton enters directly the hard process, whereas in the resolved process a charm quark or a gluon which originate from the photon takes part in the hard interaction. The energy which goes into the hard interaction is the fraction of the photon energy which is carried by the charm quark or the gluon. At HERA charm quarks are mainly produced in the direct process, the Boson–Gluon–Fusion (BGF) [33], where the exchanged photon and a gluon from the proton side interact via a quark–antiquark pair $\gamma g \rightarrow c\bar{c}$. This direct BGF process is shown in figure 2.4 a). In addition the resolved processes (see figure 2.4 b)-e)) have to be taken into account for the charm production cross section. The resolved process depicted in figure 2.4 b) is called a hadron like process. In figure 2.4 c)-e) the charm excitation processes are illustrated.

A clear separation in resolved and direct processes is possible in leading order, but at next to leading order the classification in direct or resolved is chosen by convention. For example in the next to leading order final state of a BGF process two charm quarks and an additional gluon occur. This leads to the same final state as a resolved process where out of the photon fluctuation two quarks are produced which undergo afterwards a $qg \rightarrow qg$ process, see figure 2.5.

Quarks are additionally produced in the fragmentation[5] process by gluon splitting. For charm quarks this is negligible because of the high quark mass [34].

---

[5] The fragmentation of charm quarks will be discussed in section 2.5.

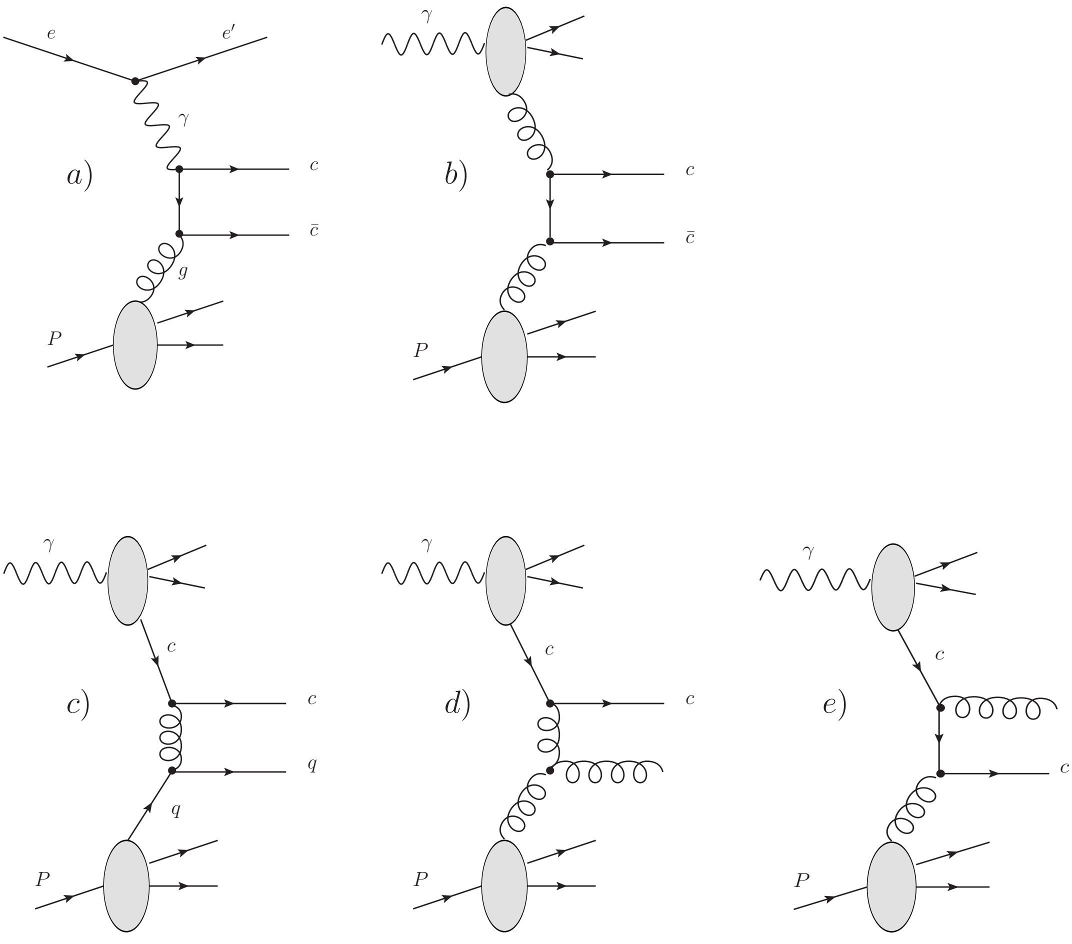

Figure 2.4: *Leading order Feynman diagrams for the production mechanisms of charm quarks in photoproduction relevant in this analysis. In a) the BGF process and b)-e) the resolved processes are depicted. The process in b) is denoted as hadron like and c)-e) are charm excitation processes.*

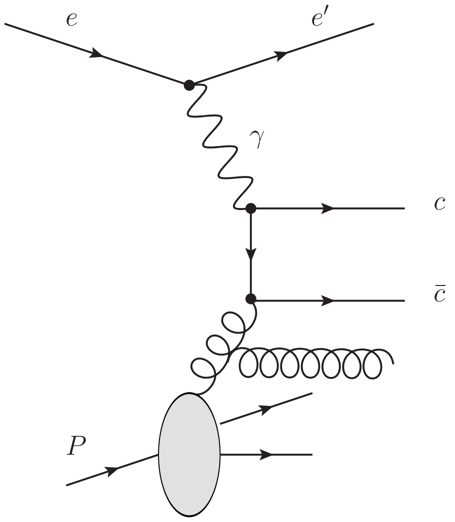

Figure 2.5: *NLO process of a BGF process with two charm quarks and an additional gluon in the final state, or of the process where out of the photon fluctuation two quarks are produced which undergo afterwards a $qg \to qg$ process.*

The factorization theorem [35] allows the photon–proton cross section $d\sigma$ of heavy hadron production, like D^* production, to be written in the following way [36]

$$d\sigma = \sum_{i,j,k} f_i^\gamma(x_1, \mu_f) \otimes f_j^P(x_2, \mu_f) \otimes d\hat{\sigma}_{ij\to kX}(\mu_f) \otimes D_k^H(z, \mu_f), \tag{2.13}$$

where $f_i^\gamma(x_1, \mu_f)$ is the photon and $f_j^P(x_2, \mu_f)$ the proton PDF. The photon parton density function is needed for resolved processes, while for the direct process it is a δ function.
The fragmentation functions $D_k^H(z, \mu_f)$ represent the probability of a quark, with index k, to fragment into a hadron H. The hadron carries the momentum fraction z of the parton momentum. In the next section the fragmentation from quarks to hadrons will be studied further.

Moreover $d\hat{\sigma}_{ij\to kX}(\mu_f)$ is the matrix element of the hard scattering process of the partons i and j. At the factorization scale the collinear divergences are absorbed within the parton distribution functions. Hence it is possible to calculate the matrix element perturbatively. The choice of the scale is not unique, because with the transverse momentum of the charm quark, the charm mass and in DIS also Q^2 several possible hard scales are present. In general, three different heavy flavor schemes exist which treat the multiple scales in a different way. In the following the main properties of the fixed flavour number scheme, the zero–mass variable number scheme and the general mass variable number scheme are discussed. In addition, the different regions of the phase space where these schemes are expected to give reliable results are depicted.

FFNS

In the fixed flavor number scheme (FFNS) only light quark flavors u, d and s and gluons are treated as active constituents of the proton [37, 38]. It is also called massive scheme because the charm and beauty quarks are taken as massive which means the mass is taken into account in the hard matrix element. The heavy quarks are not constituents of the proton or the photon and therefore the final state heavy quarks, e.g. the charm quark relevant for this analysis, are produced via the hard scattering. In the direct case this happens only via BGF. For beauty production the charm quark is assumed to be a light flavor. The FFNS ansatz can be used if p_T, the transverse momentum of the charm quark, is of similar size compared to the charm quark mass m_c. The FFNS cross section calculation diverges logarithmically for $p_T \gg m_c$.

ZMVFNS

The zero-mass variable flavor number scheme (ZMVFNS) is also referred to as massless quark scheme [5, 39]. Here all quarks are treated massless in the hard matrix element although the mass of the heavy quark is higher than Λ_{QCD}. Above a certain scale, which is often set to the mass of the heavy quark $m_{heavyquark}$, heavy quark flavors are switched on as active partons in the proton. Above this scale the heavy quark flavors have an own PDF in the proton and are treated as incoming partons. The resolved processes are taken into account with the heavy quark PDF of the photon which is switched on at the same scale as the proton PDF.

The ZMVFNS approach is a reliable treatment at phase space regions where the transverse momentum is the dominating scale, which means that the transverse momentum of the heavy quarks is at much larger than the heavy quark mass $p_T \gg m_c$.

GMVFNS

The general mass variable flavor number scheme (GMVFNS) [40] is a mixed scheme which tries to unify the massless and the massive schemes to give a description for low and high scales. Gluons, light and heavy quarks are treated as active partons. The general approach is the following [41, 42]: The divergence of the FFNS cross section calculation for $p_T \gg m_c$ can be absorbed into the charm PDF of the proton and the photon and into the fragmentation function of the charm quark to the hadron. The remaining dependence on the charm mass stays in the hard cross section and yields to a good description of the intermediate region $p_T \gtrsim m_c$. In addition in the limit $m \to 0$ the calculation of the ZMVFNS approach should give the same results. To achieve this requirement the finite terms of the cross section must be specified and properly subtracted, too. Such the main feature of the GMVFNS is that it contains the full mass dependence of the massive approach and matches at $p_T \gg m_c$ the massless approach.

PDFs are assumed to be universal for different processes, but they depend on the flavor scheme and the order. The impact of the different schemes on the gluon distribution function is displayed at a scale $Q^2 = 10\,\mathrm{GeV}^2$ in figure 2.6. The CTEQ6L is a leading order PDF where NLO diagrams are missing such that this PDF is not an appropriate choice for a next to leading order prediction.

The NLO PDFs HERAPDF1.0 and CTEQ6.5 are extracted in a general mass variable flavor number scheme and have a similar gluon PDF at this scale. The fourth PDF CTEQ5F3 shown here is a fixed flavor PDF. It is in general higher as the other two NLO PDFs because in the

FFNS charm quarks occur only via BGF and are not constituents of the proton. More gluons are needed for the heavy quark production than in a variable flavor scheme where at a scale $Q^2 = 10\,\mathrm{GeV}^2 > \mathrm{m}_\mathrm{c}^2$ charm quarks from the proton PDF contribute.

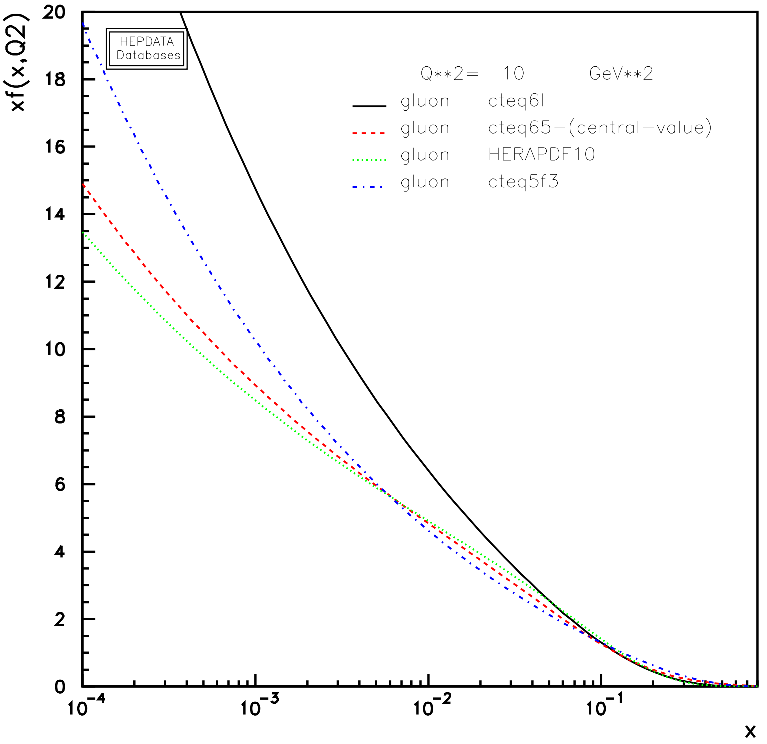

Figure 2.6: *The gluon density functions in the proton from the CTEQ group and from HERAPDF at* $Q^2 = 10\,\mathrm{GeV}^2$.

2.5 Charm Fragmentation to D* Mesons

The produced charm quarks carry color. But in nature only colorless objects are found, because of the confinement in QCD. In a process called fragmentation the charm quarks produced in the hard interaction become colorless charmed hadrons. This process is not calculable perturbatively, but described within the fragmentation formalism with phenomenological models. More precisely this process is divided into the fragmentation and the hadronisation process.

Until their virtuality is small and they become on-shell, partons from the hard process radiate in the fragmentation process. This parton showering can be calculated with perturbative QCD using a DGLAP evolution approach.

The hadronisation process describes the formation of hadrons after the parton showering. For quarks leaving the hard process the strong coupling constant rises with increasing distance from the interaction. At long distances perturbative QCD calculations are not possible.

Phenomenological models like the Lund String model [43, 44], the cluster model [45] or the independent fragmentation model [46] are needed to describe the fragmentation. Most Monte Carlo generators use the Lund String fragmentation. In this model color strings evolve between outgoing, colored particles, quarks and gluons, from the hard interaction. The energy which is saved in this color-string increases with the distance between them. The string breaks if enough energy was stored and a new quark-antiquark pair is formed. This happens until the energy is exhausted.

Furthermore, several phenomenological fragmentation functions $D_Q^H(z)$ are available which describe the longitudinal momentum transfer z from the color string to the final hadron. The fragmentation function represents the probability of the hadron H to carry the energy fraction $z = E_H/E_Q$ of the quark Q. The common approaches are the Peterson [47], the Bowler [48] and the Kartvelishvili [49] fragmentation functions.
They are defined in the following way

$$
\begin{aligned}
Peterson: \quad D_Q^H(z) &\propto \frac{1}{z[1 - 1/z - \epsilon_Q/(1-z)]^2}, && (2.14)\\
Bowler: \quad D_Q^H(z) &\propto \frac{1}{z^{1+br_Q m_Q^2}} \cdot (1-z)^a \cdot \exp\frac{bM_T^2}{z}, && (2.15)\\
Kartvelishvili: \quad D_Q^H(z) &\propto z^\alpha \cdot (1-z). && (2.16)
\end{aligned}
$$

The Peterson and Kartvelishvili parameterizations have one free parameter ϵ_Q and α, respectively, whereas the Bowler function has two free parameters a and b. The value m_Q is the mass of the heavy quark and $M_T = \sqrt{M_H^2 + p_T^2}$ denotes the transverse mass with the mass M_H and the transverse momentum p_T of the hadron. The quark radius parameter r_Q is set to 1 by default. All the parameters depend on the hadron which was considered. The ϵ_Q parameter scales for charm and beauty fragmentation with $1/m_Q^2$ [50]. The heavy quark fragmentation function is expected to be harder than that of light flavors because the formed hadron carries a high momentum fraction of the quarks momentum and for very heavy quarks the fragmentation function peaks near one [16]. The recent H1 measurement of the fragmentation function in $ep \to eD^*X$ processes [51] and its impact on this analysis will be discussed in section 3.2.

The D^* meson

Properties of the D^{*+} meson:
Mass $m(D^{*+}) = (2010.25 \pm 0.14)\,\mathrm{MeV}$
quark content $(c\bar{d})$
$I(J^P) = \frac{1}{2}(1^-)$
Full width $\Gamma = (96 \pm 22)\,\mathrm{keV}$

Table 2.1: *General overview of D^{*+} meson properties [16]. The properties are aquivalent for the charge conjugate D^{*-} meson. I denotes here the isospin, J the spin and P the parity.*

In this analysis the charm production is studied with charm quarks which have fragmented to charged D^* mesons[6]. Here only general properties of the D^* meson are presented, further explanation of the D^* selection will be given in section 7.1.

---

[6] in the following D^* meson represents both charge signs

The fragmentation from a charm quark to a D^* meson has the relative probability of $f(c \rightarrow D^{*\pm}X) = (23.5 \pm 0.7 \pm 0.7)\%$ [52]. In this study the golden decay channel

$$D^{*\pm} \overset{(67.7\pm0.5)\%}{\longrightarrow} D^0\pi^\pm_{slow} \overset{(3.8\pm0.05)\%}{\longrightarrow} K^\mp\pi^\pm\pi^\pm_{slow} \tag{2.17}$$

is used for the D^* selection with a total branching ration of $BR = (2.6 \pm 0.04)\%$ [16]. An overview of the general properties of the D^* meson is given in table 2.1. The mass difference of the decaying D^* meson and the D^0 is just above the pion mass. Hence the produced pion has only a small momentum and is called π_{slow}

Chapter 3

MC Generators

The data results from ep scattering experiments are compared to Monte Carlo (MC) event generators. The calculation of physics processes can be done in leading order or next to leading order of α_s. Events generated by leading order MC generators include the hadronisation to the final state hadrons, whereas the NLO calculations predict only NLO parton level cross sections by fixed order perturbation theory without any non–perturbative hadronisation process. In LO MCs higher order corrections are approximated with parton showers. They can mimic changes in shape but it is not expected to give the correct normalization in contrast to the NLO predictions. For data correction, efficiency determination and uncertainty estimation LO MCs have been used. The measured cross section are compared to LO and NLO predictions. In the following these predictions will be introduced.

3.1 Leading Order MC Generators

The generation of final state particles is factorized in several steps which are related to the QCD factorization theorem. The MC generator starts with the hard interaction process of the ep scattering. The hard matrix element is generated in LO α_s. The event kinematics of the process are set by the hard interaction. The incoming parton from the proton side of the process is represented with the proton PDF. The proton PDF is evolved with DGLAP or CCFM evolution equations to the necessary factorization scale. The hard matrix element is convoluted with the PDF.

In charm quark photoproduction direct and resolved–photon processes occur. In the resolced processes the partons which take part in the hard interaction is emitted by the photon. Because of this hadronic behavior a photon PDF is required. The flux of the exchanged photons is calculated with the Weizsäcker-Williams approximation [9–11].

The MC generators also include initial and final state parton showers evolving with DGLAP evolution equations. Parton shower proceed until no virtual parton is left and all partons are on-shell partons. In the hadronisation step the transition of the colored generated partons to real colorless hadrons is computed. The output of a MC generator are events, four momentum vectors, which have in ideal case the same properties as real data. These events are then passed through the H1 detector simulation, which is based on the GEANT simulation program [53],

see section 3.4.
In the following the two different LO MC event generators, Pythia and Cascade, which have been used in this analysis will be briefly presented.

PYTHIA

The leading order matrix element in the MC generator program PYTHIA [54] includes direct photon–gluon fusion and the resolved photon processes from hadron like and charm excitation processes. The processes are calculated separately and added afterwards. The cross section of the hadron like resolved process is negligible because it is one order of magnitude smaller than the direct or excitation cross section.
In this analysis PYTHIA is used in the massless mode which means that the heavy charm quark is treated as a massless parton.
Furthermore PYTHIA can be run in the massive mode, which is also named full inclusive mode. In this mode the charm quark is treated as a massless parton like the other light flavors in the charm excitation process and in all other processes the charm quark is handled as massive in all steps of the calculation. The massive mode is not used in this analysis.
The PYTHIA program uses the collinear factorization approach. The DGLAP evolution equations were used to calculate parton showers. The initial transverse momenta k_T of the incoming partons, which go into the hard scattering process, are neglected in the further calculation. Transverse momenta have to be generated within the hard interaction. The matrix element does not depend on the transverse momenta of the incoming gluon and is calculated on-shell.
The hadronisation process is performed with the Lund String fragmentation model [43, 44] and with the Bowler fragmentation function for the longitudinal fragmentation of the charm quark into the D^* meson was chosen.
The used proton PDF is CTEQ6L [55] and the photon PDF GRVLO [56, 57].

CASCADE

In the CASCADE [58] MC program the initial state cascade is computed with the CCFM evolution equations [25–28] with an unintegrated parton density function. The CCFM approach includes angular constraints and no ordering in the transverse momentum of the radiated partons. Here incoming gluons can possess finite momentum. Thus the matrix element depends on k_T and has to be calculated off-mass-shell. The charm quark is treated as massive. The used PDF set A0 [59] was fitted to F_2 data from HERA. CASCADE includes only the direct BGF process and not the resolved processes. However, some charm excitation effects are mimicked by the implementation of the unordered k_T approach in the parton evolution. For the hadronisation process of partons to hadrons the the Lund String model is used as implemented in the PYTHIA program. The Peterson parametrization for the longitudinal fragmentation of the charm quarks into the D^* mesons is used.

3.2 Fragmentation

The PYTHIA MC simulation which has been used for the data correction was generated with a Bowler fragmentation function with the fragmentation parameters $a = 0.437$ and $b = 0.850$.
A recent H1 measurement [60] of the fragmentation variable z[1] has observed that the data prefers not one fragmentation function for the whole phase space, but different fragmentation parameters in different regions of photon gluon center of mass energies $\hat{s}$. The fragmentation variable is defined here as the fraction of energy carried by the parton which is transferred to the hadron. Low $\hat{s}$ values imply that the D^* production has happened close to the threshold and that additional particle production in the event is unlikely. In contrast in the high $\hat{s}$ region it is possible that many more particles occur in the event. The parameters α for the Kartvelishvili fragmentation function were determined in this two regions. The threshold between these two regions was set to be near $\hat{s} = 70\,\mathrm{GeV}^2$ [61].
In the PYTHIA MC simulation this $\hat{s}$ dependence is not implemented. Hence the generated fragmentation distribution is reweighted to the Kartvelishvili parametrization [49] with a $\hat{s}$ dependence. Therefore the PYTHIA MC is divided into two samples with events with $\hat{s} < 70\,\mathrm{GeV}^2$ and events which have a photon–gluon center of mass energy above the threshold. The distribution of the fragmentation variable z for the two samples and the total sample are illustrated in figure 3.1.

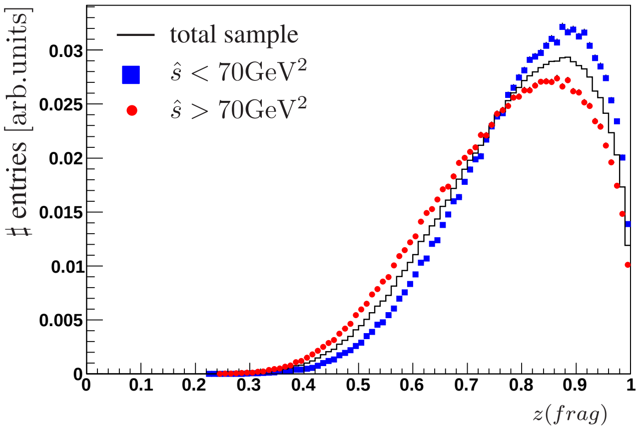

Figure 3.1: *Distribution of the generated fragmentation variable z. The filled dots corresponds to events with $\hat{s} > 70\,\mathrm{GeV}^2$ and the rectangle to $\hat{s} < 70\,\mathrm{GeV}^2$. The generated distribution for the whole sample is drawn as a black solid line.*

Then the distributions of both MC samples are reweighted to follow Kartvelishvili parametrizations which have the same α values ($\alpha = 4.4$ for $\hat{s} < 70\mathrm{GeV}^2$ and $\alpha = 10.3$ for $\hat{s} > 70\mathrm{GeV}^2$) for the corresponding $\hat{s}$ region as measured at H1 [60]. This H1 measurement is a DIS measurement, and in the present analysis the values for RAPGAP MC are used because it is similar to the PYTHIA MC simulation. The used fragmentation parameters α are listed in table 3.1.

---

[1] Please note that the fragmentation variable z and the inelasticity of the D^* meson $z(D^*)$ are different quantities.

$\hat{s}$	α	α *uncertainty*
$< 70\mathrm{GeV}^2$	4.4	$^{+0.6}_{-0.5}$
$> 70\mathrm{GeV}^2$	10.3	$^{+1.9}_{-1.6}$

Table 3.1: *Parameter of the fragmentation function for the corresponding $\hat{s}$ region from [60].*

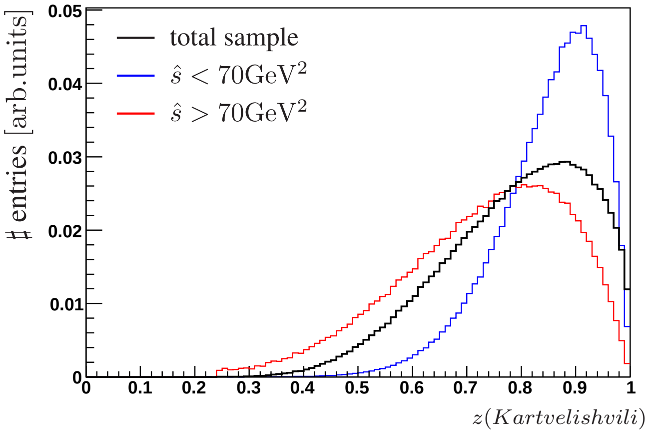

Figure 3.2: *Distribution of the reweighted z to Kartvelishvili. The red line corresponds to events with $\hat{s} > 70\mathrm{GeV}^2$ and the blue line to $\hat{s} < 70\mathrm{GeV}^2$. The obtained value of α parameter amount to 4.4 and 10.37 respectively. The reweighted distribution for the whole sample is drawn as a black solid line.*

In figure 3.2 the distribution of the fragmentation variable after the reweighting is presented for the total MC and for the low and high $\hat{s}$ samples. To check if the reweighting was successfull the reweighted distributions are fitted again with a Kartvelishvili parametrization and the resulting α parameter amounts to 4.4 and 10.37 for the corresponding $\hat{s}$ regions.
Because the CASCADE MC simulation is generated with the same Bowler fragmentation function the same reweighting procedure is needed to achieve a $\hat{s}$ dependent fragmentation function. The reweighting factors for CASCADE and PYTHIA have been calculated separately.

3.3 Next to Leading Order Calculations

For the comparison with next to leading order predictions calculations the FFNS from the FMNR program and calculations based on the general mass variable flavor number scheme are used.

FMNR		
Parameter name	Central value	Variation
Charm mass	$m_c = 1.5$ GeV	$1.3 < m_c < 1.7$
Renorm. Scale	$\mu_r = \mu_0 = \sqrt{m_c^2 + (p_{t,c}^2 + p_{t,\bar{c}}^2)/2}$	$0.5 < \mu_r/\mu_0 < 2$
Fact. Scale	$\mu_f = 2 \cdot \mu_0$	$1. < \mu_f/\mu_0 < 4$

GMVFNS		
Parameter name	Central value	Variation
Charm mass	$m_c = 1.5$ GeV	
Renorm. Scale	$\mu_r = \mu_0 = \sqrt{m_c^2 + (p_{t,c}^2 + p_{t,\bar{c}}^2)/2}$	$0.5 < \mu_r/\mu_0 < 2.0$
Fact. Scale	$\mu_f = \mu_0$	$0.5 < \mu_f/\mu_0 < 2.0$

Table 3.2: *Parameters used in the NLO MC simulations. Shown are the central values and the variations of the parameters.*

FMNR

In the FMNR program [37] a fixed flavor number scheme NLO calculation in the collinear approach is implemented. The program predicts parton level cross sections for heavy flavors, in this case charm quarks, in photoproduction. In contrast to MC event generators, where predictions for the full hadronic final state are given, here weighted parton level events are provided. The FMNR program can be run in a single differential mode where weighted parton level events containing one outgoing quark are generated, or in the double differential mode with two or three final state partons, i.e. a charm quark pair and in addition one light parton. The resolved and direct processes are provided separately and are added afterwards for the comparison with the measurement. The fragmentation from a charm quark to a D^* meson is done by the Peterson fragmentation. The quark momentum is multiplied by a random number which is distributed according to the Peterson function. For the photon PDF the GRV-HO [56, 57] and for the proton PDF the HERAPDF1.0 [17] is used.

The FMNR program requires some steering parameters as program input. For example the value for the Λ_{QCD} parameter has to be set. The Λ_{QCD} parameter is connected to α_s by

$$\Lambda_{QCD} = \mu_r \exp\left[\frac{1}{\beta_0\alpha_s(\mu_r)} - \frac{\beta_1}{\beta_0^2}\ln\left[\frac{-2}{\beta_0\alpha_s(\mu_r)}\right] + C + \frac{1}{\beta_0^3}(\beta_2\beta_0 - \beta_1^2)\alpha_s(\mu_r) + O(\alpha_s^2)\right], \tag{3.1}$$

where C is an arbitrary constant and β_i are parameters of the β-function which depend on the number of flavors n_f [62]. The choice of the Λ_{QCD} value has to be consistent with the value used for the PDF extraction. One has to point out that the FMNR program requires a $\Lambda^5_{QCD,\overline{MS}}$ value [63], which means that the number of active flavors is $n_f = 5$. In the $\overline{MS}$ scheme C is set to 0 and with numbers $\Lambda^5_{QCD,\overline{MS}}$ can be expressed with

$$\Lambda^5_{QCD,\overline{MS}} = \mu_r exp\left[-\frac{6}{23}\left(\frac{\pi}{\alpha_s(\mu_r)} - \frac{29}{23}\ln\left[\frac{12\pi}{23\alpha_s(\mu_r)}\right] - \frac{91581}{152352}\frac{\alpha_s(\mu_r)}{\pi}\right)\right], \tag{3.2}$$

[62]. If a PDF with n_f not equal to 5 is provided by the used PDF table, the Λ_{QCD} value has to be converted to a $\Lambda^5_{QCD,\overline{MS}}$ according to [62]. The impact of the choice of the Λ_{QCD} parameter on the strong coupling α_s is illustrated in figure 3.3. The α_s dependence with the number of flavors $n_f = 3$ and a corresponding Λ^3_{QCD} is totally different at small scales μ_r relevant in this analysis compared to the α_s dependence with a number of flavor $n_f = 5$ and a corresponding Λ^5_{QCD}. At $\mu_r \sim 100\,\mathrm{GeV}$ the two curves will match.

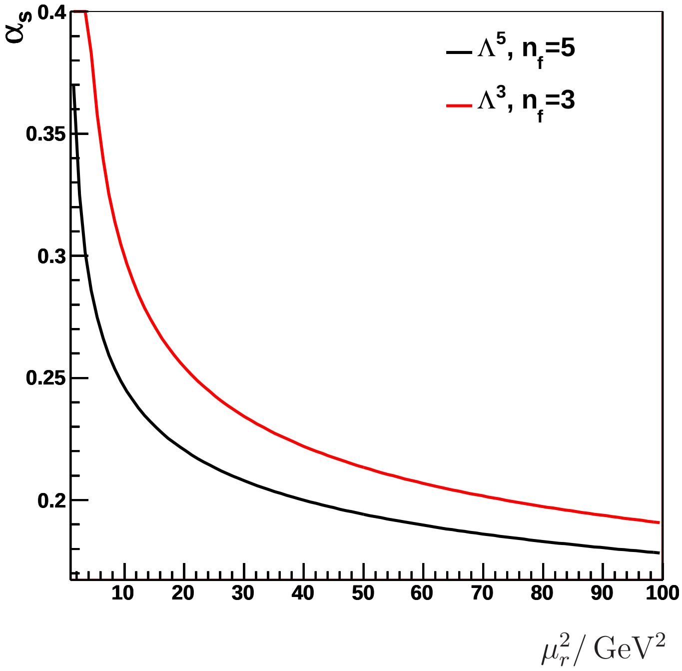

Figure 3.3: *α_s as a function of μ_r^2 for different choices of the Λ_{QCD} parameter. The red curve corresponds to $\Lambda_{QCD,3}$ and the black curve to $\Lambda_{QCD,5}$. For the Λ_{QCD} values used here the $\alpha_s(M_Z)$ amounts to* 0.115 *for* $\Lambda_{QCD,3}$ *and* 0.118 *for* $\Lambda_{QCD,5}$.

For the used PDF HERAPDF1.0 $\Lambda^5_{QCD} = 0.2626$ is given directly in the PDF table.
Another steering parameter is the charm mass value. It is set to $m_c = 1.5\,\mathrm{GeV}$.
In general the charm mass, the transverse momentum of the charm quark and Q^2 are possible renormalization scales. In photoproduction Q^2 cannot be an appropriate choice and a combination of the charm quark mass and the transverse momentum is used as renormalization scale. The renormalization scale is chosen to be the transverse mass $m_t = \sqrt{m_c^2 + (p_{T,c}^2 + p_{T,\bar{c}}^2)/2}$ and the factorization scale is set to $2 \cdot m_t$.
The uncertainties on the FMNR predictions are estimated by varying the charm mass, the factorization and the renormalization scale independently and adding the resulting differences in quadrature. The differences according to the PDF choice are small compared to the scale variation uncertainties. The detailed settings are presented in table 3.2.
The effect of each particular variation is discussed in section 11.

GMVFNS

A next to leading order cross section prediction in the GMVFNS is provided by Kramer, Spiesberger and Kniehl [41, 64]. The main properties of this approach have been presented in section 2.4. Predictions for direct and resolved contributions to the cross section have been calculated in GMVFNS. The transition from quarks to the D^* meson is determined with fragmentation functions from [65] containing recent experimental data from the Belle and CLEO collaborations [42]. The HERAPDF1.0 for the proton PDF and AFG04 [66] for the photon PDF have been used.

The renormalization and factorization scale are set to $\mu^2_{r,f} = p_T^2 + m_c^2$ and the charm mass is $m_c = 1.5\,\mathrm{GeV}$. The uncertainty of the GMVFNS prediction is determined by varying the renormalization, the factorization scale for the initial state and the factorization scale for the final state within $0.5 < \mu/\mu_0 < 2$ with a scale μ. All combinations of variation are studied where the ratio of any two scales is not larger than 2. The combination with the maximal or minimal cross section value is taken as uncertainty, respectively.

3.4 Detector Simulation

MC generators have been used in this analysis to determine the cross section of inclusive D^* mesons in photoproduction. In the data analysis the acceptance, the selection efficiency for selecting events containing a D^* meson and the systematic uncertainties associated with the measurement are determined with LO MCs.

MC programs provide the four vectors of the stable final state particles. In order to compare them to the H1 data, the generated events are passed through the H1SIM package which is a simulation of the H1 detector response based on the GEANT simulation program [53]. In the H1 detector central jet chamber simulation the specific energy loss of particles in the detector volume, particle avalanches and the readout electronics are simulated. All detector components together with their inefficiencies, detector acceptance, dead material and secondary particle production are taken into account in H1SIM. A detailed description of the central jet chamber hit simulation and the specific energy loss in the central jet chambers of the H1 detector is given in section 5.

Moreover for this analysis the H1 trigger simulation of the Fast Track Trigger is used for the D^* event selection. The Fast Track Trigger simulation is not simulated in H1SIM but has to be simulated in a post processing step within the FTTEMU package.

The H1SIM output of the whole event has to pass the reconstruction package H1REC which is the same software as used for data reconstruction of a certain run period. The run period has to be chosen with respect to the run period of the data to which it is compared. For the comparison of cross sections the MC luminosity is required. In a preprocessing step the generated luminosity is distributed over the run period.

Chapter 4

HERA and the H1 Detector

In this chapter first a brief overview of the HERA collider and the H1 detector is presented. Then the main components relevant for this analysis are depicted. This is followed by a description of the H1 luminosity and trigger systems.

4.1 HERA Storage Ring at DESY

The 'Hadron-Elektron Ring Anlage', HERA, is an electron proton collider at DESY (Deutsches Elektronen Synchrotron) in Hamburg. It is located in a $6.3\,\mathrm{km}$ long ring tunnel and was operating from 1992 until 2007. Figure 4.1 illustrates the HERA accelerator together with the two smaller pre-accelerator facilities PETRA and DESY III. Within the HERA machine electrons or

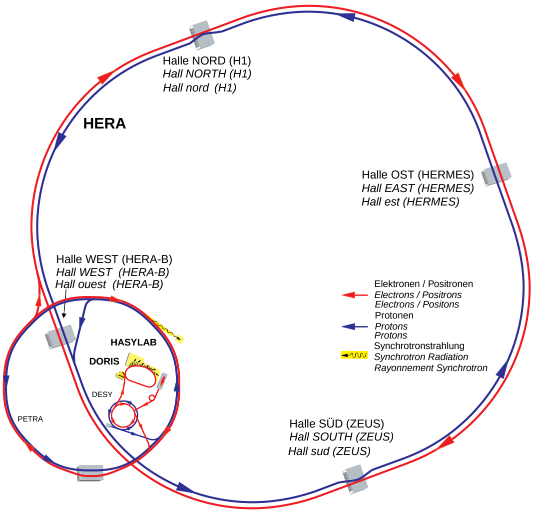

Figure 4.1: *HERA storage ring with the preaccelerators PETRA and DESY and the experimental hall where the experiments H1, ZEUS, HERMES and HERA-B were located. The picture is adopted from [67].*

positrons were accelerated to beam energies of $E_e = 27.6\,\mathrm{GeV}$ and protons to $E_p = 920\,\mathrm{GeV}$[1], with the electrons rotating clockwise and the protons conversely in the accelerator ring. The HERA machine operated with 180 particle bunches, each of them filled with 10^{10} particles. The length of the electron and proton bunches were $\sim 8\ \mathrm{mm}$ and $\sim 30\,\mathrm{cm}$, respectively.
At the HERA machine four experiments were situated. H1 and ZEUS were placed at the two interaction points in the north and south where the beams were brought to collision. The two collider experiments H1 and ZEUS were built as multipurpose detectors, designed for the precise measurement of electron–proton interactions. The bunch crossing rate was $10.4\,\mathrm{MHz}$ which corresponds to a time interval between the bunch crossings of $96.5\,\mathrm{ns}$. The center of mass energy which was available at the collision points at the two collider experiments amounts to $\sqrt{s} \approx 319\,\mathrm{GeV}$.
The HERA experiments HERMES and HERA-B are placed in the west and east halls. These experiments were “fixed target” experiments with special physics programs. At the HERMES experiment the spin structure of the nucleon was studied by colliding the polarized electron beam with a polarized gas target. The purpose of the HERA-B experiment was to study CP violation in decays of B mesons in nucleon proton interactions. This measurement was performed using the proton beam which was collided with nuclei of fixed target wires. Data taking at HERA-B was already finished in 2001.

At H1 the first data taking period from 1992 to 2000 (HERAI) ended with a shutdown of the accelerator in order to perform a machine and detector upgrade to increase the luminosity. In the second running period (HERAII) data for physics analysis were recorded during the years 2004–2007. In figure 4.2 the development of the luminosity collected by the H1 experiment is illustrated. The total luminosity collected by H1 amounts to $0.5\,\mathrm{fb}^{-1}$. In addition the figure displays the luminosity of the low proton beam energy runs, $E_p = 460\,\mathrm{GeV}$ and $E_p = 575\,\mathrm{GeV}$, collected in the last three months, used to measure the structure function F_L [68].

4.2 H1 Detector

The H1 detector is used to study the high energy collisions of electrons and protons. A detector overview is illustrated in the technical drawing of figure 4.3 with the list of the abbreviations summarised in table 4.1.

The H1 coordinate system is chosen as follows: The origin of the H1 coordinate system is located in the nominal interaction point (IP). The direction of the outgoing proton beam defines the positive z-axis (forward region). The x-axis points to the middle of the HERA ring and the y-axis points upwards. The measurement of transverse momenta of particles is performed in the x–y plane. Moreover, the coordinates can be described with the polar angle (θ) and the azimuthal angle (ϕ) which are defined as angle between the trajectory and the z-axis and as angle in the x–y plane, respectively. With this the pseudorapidity is defined as $\eta = -\ln\tan(\theta/2)$.

---

[1] Until 1996 the proton beam energy was $E_p = 820\,\mathrm{GeV}$.

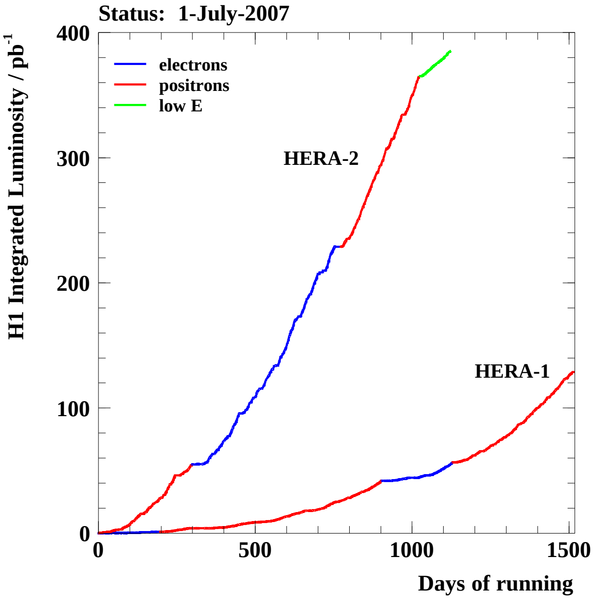

Figure 4.2: *Development of the luminosity collected by the H1 experiment in the years 1992-2007 [67]. The luminosity for the low proton energy run is depicted too.*

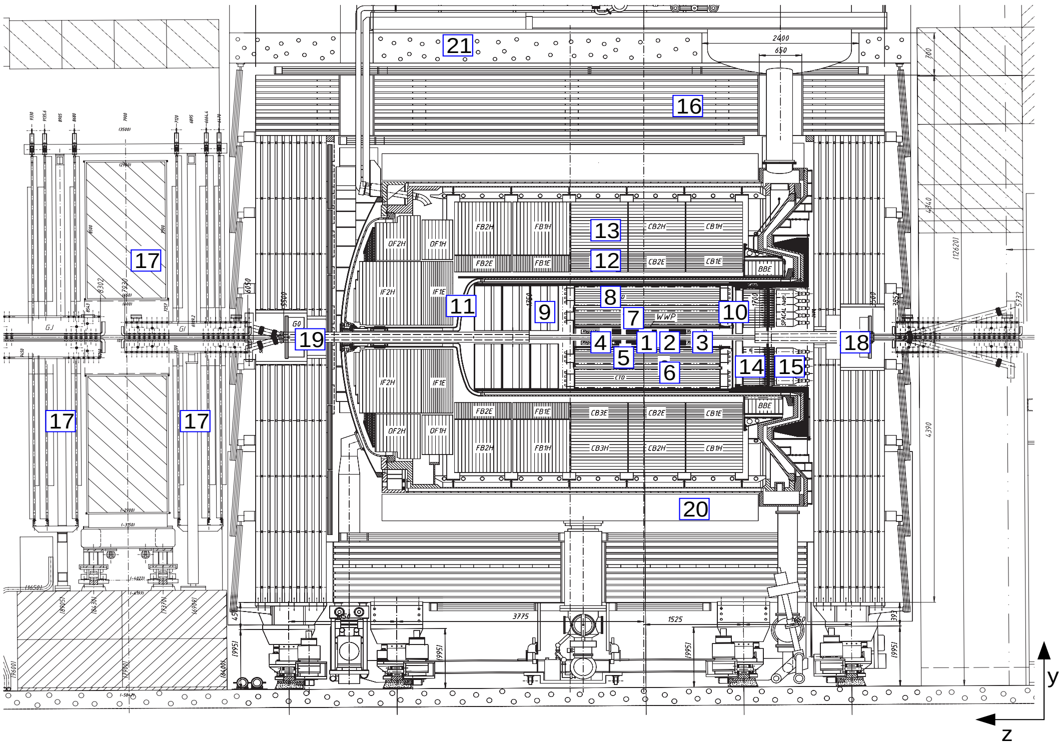

Figure 4.3: *The technical drawing of the H1 detector after the upgrade (from [67]). The numbers are listed and explained in table 4.1.*

Number	detector component	abbreviation
$\boxed{1}$	nominal Interaction Point	IP
$\boxed{2}$	Central Silicon Tracker	CST
$\boxed{3}$	Backward Silicon Tracker	BST
$\boxed{4}$	Forward Silicon Tracker	FST
$\boxed{5}$	Central Inner Proportional Chamber	CIP2k
$\boxed{6}$	Central Outer Proportional Chamber	COP
$\boxed{7}$	Central Jet Chamber 1	CJC1
$\boxed{8}$	Central Jet Chamber 2	CJC2
$\boxed{9}$	Forward Tracking Detector	FTD
$\boxed{10}$	Backward Proportional Chamber	BPC
$\boxed{11}$	Liquid Argon cryostat	LAr cryostat
$\boxed{12}$	electromagnetic Liquid Argon Calorimeter	LAr (el.)
$\boxed{13}$	hadronic Liquid Argon Calorimeter	LAr (had.)
$\boxed{14}$	electromagnetic Spaghetti Calorimeter	SpaCal (el.)
$\boxed{15}$	hadronic Spaghetti Calorimeter	SpaCal (had.)
$\boxed{16}$	Central Myon System	CMS
$\boxed{17}$	Forward Myon System	FMS
$\boxed{18}$	backward super-conducting magnet	GG
$\boxed{19}$	forward super-conducting magnet	GO
$\boxed{20}$	super-conducting coil	
$\boxed{21}$	concrete shielding	

Table 4.1: *Summary of the H1 detector components and their corresponding number in figure 4.3.*

The H1 detector covers nearly the full solid angle (4π). Furthermore the design of the H1 detector takes into account the asymmetry of the electron and proton beam energies. The instrumentation is concentrated predominantly in the proton direction, whereas the less complex instrumentation in the backward region is mainly used for the detection of the scattered electron.

In the following an overview of the detector components is given. A detailed description of the H1 detector can be found in [69, 70].

Silicon detectors surround the IP $\boxed{1}$ to measure the decay vertices from long lived particles. The Central Silicon tracker (CST) $\boxed{2}$ encloses the beam pipe with an angular coverage of $30^\circ \leq \theta \leq 150^\circ$. The angular coverage is completed with the Forward Silicon Tracker (FST) $\boxed{4}$ located in the forward direction and the Backward Silicon Tracker (BST) $\boxed{3}$ placed in the backward direction.

The components of the central tracking detector are located further outward and will be discussed in more detail in section 4.3. The main components are the two Central Jet Chambers (CJC1 and CJC2) $\boxed{7}$, $\boxed{8}$ which are used for track reconstruction. A detailed discussion of the properties of the Central Jet Chambers will be given in section 4.4.

The identification and track reconstruction of hadronic final state particles in the forward direction can be done with the Forward Tracking Detector (FTD) $\boxed{9}$. Tracks of the scattered electron can be detected with the Backward Proportional Chamber (BPC) $\boxed{10}$.
The calorimeter system is located around the tracking devices. The Liquid Argon Calorimeter (LAr) is split into an electromagnetic $\boxed{12}$ and a hadronic part $\boxed{13}$ and covers the forward and central region. In addition the Spaghetti Calorimeter (SpaCal), which consist of an electromagnetic $\boxed{14}$ and hadronic $\boxed{15}$ section, is placed in the backward direction. The calorimeter devices will be explained in detail in section 4.5. A superconducting coil $\boxed{20}$ surrounds this detector components and yields a magnetic field of $B = 1.16\,\mathrm{T}$ in the tracking detector. Muons can be detected with the Forward Muon Spectrometer (FMS) $\boxed{17}$ and the Central Muon System (CMS) $\boxed{16}$ situated in the outer part of the detector. The two colliding electron and proton beams were finally focused by two magnets arranged in the backward $\boxed{18}$ and forward $\boxed{19}$ direction to the IP.
In the following sections the detector components relevant in the present thesis are explained in detail.

4.3 Central Tracking Detector

In the central region of the H1 detector $25^\circ \leq \theta \leq 155^\circ$, corresponding to a pseudorapidity range of $-1.5 < \eta < 1.5$, tracks of charged particles are detected with the detectors of the central tracking system. The central tracking detectors are arranged concentrically around the beam pipe and are presented in figure 4.4. They are all situated in a solenoidal magnetic field of $1.16\,\mathrm{T}$ so that the measurement of transverse momenta of charged particles can be performed. Closest to the beam pipe is the central silicon tracker which is used to measure precisely the primary and secondary vertex of a particle interaction [71]. Then follows the central inner proportional chamber (CIP2k). The CIP2k consists of five cylindrical multiwire proportional chambers. It is mainly used for triggering events from ep interactions and rejects events from beam related background [72].
The two large central jet chambers are separated by the two outer chambers, the central outer z chamber (COZ) and the central outer proportional chamber (COP). The COP was active until 2006. The COZ is a drift chamber which has the wire perpendicular to the beam pipe. Hence it can be use for measuring the z–coordinate of the tracks. The COZ enhances the precision of the z–coordinate measurement and therefore the θ measurement of the particle tracks of the CJCs.

4.4 Central Jet Chambers and Measurement of the Energy Loss

H1 has two central jet chambers, the inner smaller CJC1 and the outer larger CJC2. The CJC has a length of $220\,\mathrm{cm}$ and is designed as follows: The signal wires have been arranged parallel to the z-axis. The smaller inner CJC1 has 30 cells in ϕ, which are tilted by 30 degrees, and

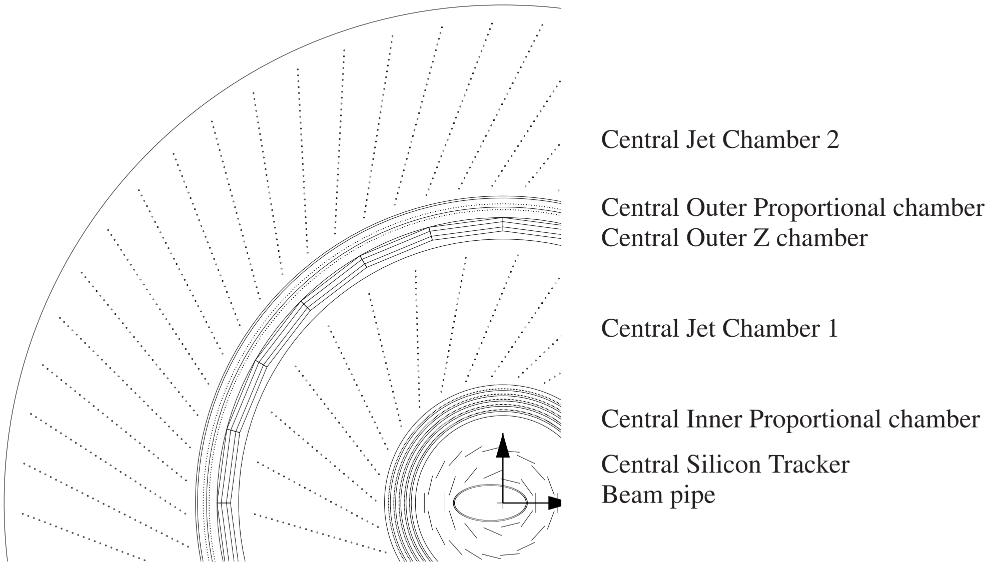

Figure 4.4: *Components of the CTD: The CJCs, CIP, COZ, COP, from [67]*

24 signal wires per cell whereas the CJC2 surrounds the CJC1 and consists of 60 cells with 32 signal wires per cell (see figure 4.4). In total the CJC has 2640 signal wires. The CJC parameters are summarized in table 4.2.

CJC Parameters		
Parameter	CJC1	CJC2
# cells	30	60
# sense wires per cell	24	32
# sense wires	720	1920
total amount of wires	3990	10380
sense wire distance	10.16 mm	
sensitive wire length	2200 mm	

Table 4.2: *Summary of CJC parameters taken from [67] where a more detailed summary of CJC properties can be found. In addition to the sense wire the CJC consists of potential wires, field wires and cathode wires which are not summarized in this table.*

With the CJC it is possible to measure the properties of charged tracks. The tilt of the cells has here two advantages: First, the electrons which have been produced by the particle ionizing the chamber gas drift perpendicular to the track for a wide range of particle transverse momenta. In addition, also large p_T tracks which traverse straight through the chambers are measured in at least two cells.

The CJC wire information is further used for track based triggering by the DC–R/ϕ trigger [73] and in the years 2005-2007 by the Fast Track Trigger [74, 75].

Track reconstruction

The present analysis deals with particle tracks of the decay products of the D^* meson. Hence a precise track reconstruction is needed for a sufficient measurement of the particle properties. In the central jet chambers the momentum of the track is determined by the measurement of the track curvature κ

$$p_T[\mathrm{GeV}] = -\mathrm{Q}\frac{0.3 \cdot \mathrm{B_z[T]}}{\kappa[\mathrm{m}^{-1}]}, \tag{4.1}$$

where Q represents the charge and B_z the magnetic field. Due to the dead material between the two jet chambers the momentum and scattering angle of a track can change during the transition from CJC1 to CJC2. The two track segments of the inner chamber and outer chamber are combined with a broken-line fit [76].

In addition corrections due to the energy loss of particles in material, e.g. the gas of the central jet chambers, are taken into account. These corrections depend on the particle type and are applied to the data summary tapes produced with the final detector simulation and reconstruction software (DST7). The new simulation of the specific energy loss in the CJCs in the H1 detector simulation software and its calibration and correction implemented in the H1 reconstruction software have been developed in this thesis, see chapters 5 and 6. After the first track fit the particle is identified using the specific energy loss dE/dx information. Then the track fit is redone with the correct particle hypotheses. The information is stored in so called non vertex fitted tracks.

In the next step the precision of the track can be enhanced by fitting the tracks to the event vertex. The material in front of the central jet chambers has to be taken into account. Moreover informations from other detector components are used. Additional hits from the COZ lead to a higher θ precision. The vertex information from FST and BST detectors help to get a high precision for the event vertex position. The information of the tracker devices together with the calorimeter devices is used to reconstruct the hadronic final state particles.

The resolution of the transverse momentum for tracks with CJC and CST information is $\sigma(p_T)/p_T \approx 0.015 \oplus 0.002 p_T/\mathrm{GeV}$ determined from cosmic data [77]. For tracks which can be fitted to the vertex the same resolution is found even without the CST information.

Measurement of the energy loss in the CJC

If a particle traverses the CJC it ionizes the chamber gas and produces electrons. During this process the particle looses its energy. The energy loss of a particle depends on the atomic charge and the density of the material it traverses. The chambers work with a gas mixture of argon and ethan $(50 : 50)$ at atmospheric pressure. For argon one has $\frac{Z}{A} = 0.450589$, with the atomic number Z and the atomic weight A, and $\rho = 1.782 \cdot 10^{-3}\,\mathrm{g/cm^3}$. For ethane the values are $\langle\frac{Z}{A}\rangle = 0.59861$ and $\rho = 1.356 \cdot 10^{-3}\,\mathrm{g/cm^3}$. From this, the average is $\langle\rho\,\frac{Z}{A}\rangle = 0.807\,\mathrm{g/cm^3}$, and the quantity characterizing the mean energy loss in the material, here the gas, is

$$K\left\langle\frac{\rho Z}{A}\right\rangle = 0.24791\,\mathrm{keV/cm}. \tag{4.2}$$

with

$$K = 4\,\pi\,N_A\,r_e^2\,m_e = 307.075\,\mathrm{keV\,g^{-1}\,cm^2}. \tag{4.3}$$

Here N_A is Avogadro's constant, r_e is the classical electron radius and m_e is the electron mass.

The electrons produced in the ionization process drift to the signal wires and deposit their charge. The charge deposited on the wires is therefore proportional to the energy loss of the particle.

The charge pulses are digitized and the charge amplitude $A_\pm$ of a signal wire is

$$A_\pm = g_\pm \cdot q_\pm, \tag{4.4}$$

where the $\pm$ denotes the two wire ends. The gain $g_\pm$ represents the electronic amplification whereas the gas amplification is included in the charge $q_\pm$.

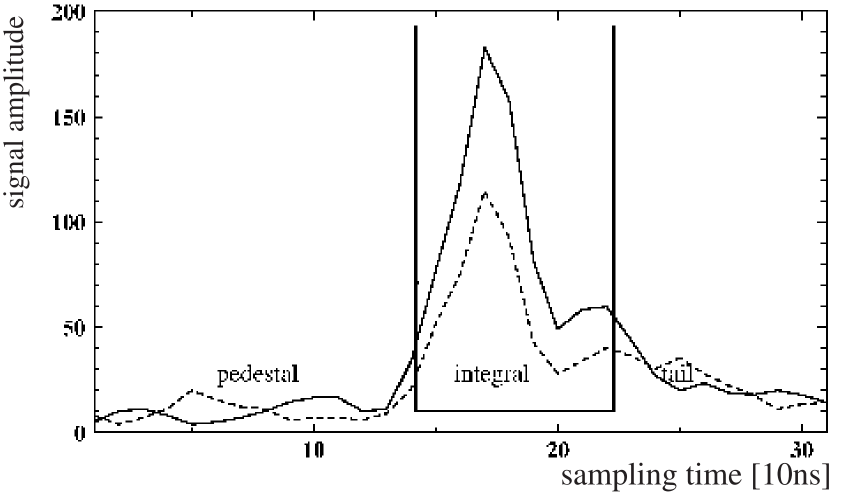

Figure 4.5: *The amplitude of the digitized signal as a function of time in bins of* $10\mathrm{ns}$ *for both wire ends (indicated with the full and the dashed curve), from [1].*

However not every signal on the wire ends is stored as hit. A signal hit after the digitization is depicted in figure 4.5 together with the pedestal on the left and the tail on the right side of the pulse. If the pulse height is above a threshold the 'QT code' integrates a certain interval of the pulse and stores this information. The remaining charge is cut away because of storage limitation. The charge deposited in a cell and the size of a cell are measured. However, the specific energy loss is defined as the energy loss per unit pathlength. With the measurement of the angle θ, the angle between the track and the z-axis, the size of the cell Δr can be converted into the tracklength in the cell by dividing Δr by $\sin\theta$. The relation between the tracklength Δl and the cell size Δr is sketched in figure 4.6.

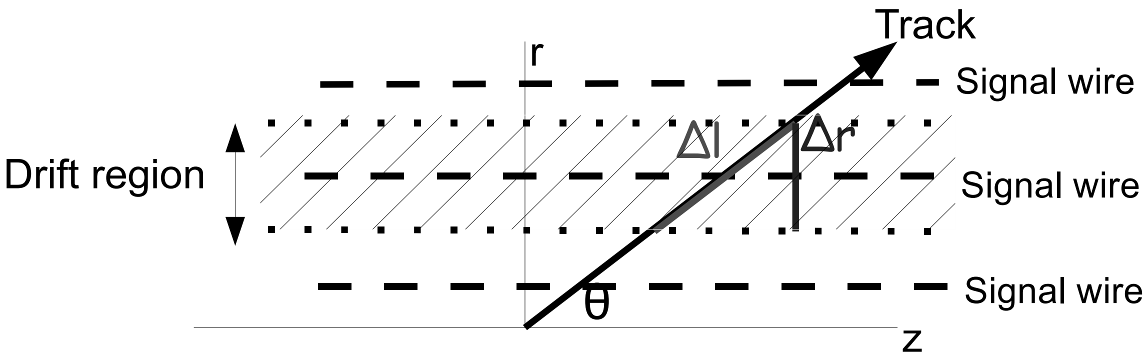

Figure 4.6: *The size of the cell Δr can be converted into the path length Δl by dividing Δr by $\sin\theta$. The cell size is depicted with the dotted lines and the signal wires with the dashed lines. The drift region is illustrated as hatched area. The electrons produced within the drift region drift to the signal wire in the center of the cell.*

From the single hit measurement the mean energy loss is calculated. For this procedure the averaging over $1/\sqrt{\mathrm{d}E/\mathrm{d}x}$ is performed, which is more symmetric function as the $\mathrm{d}E/\mathrm{d}x$ distribution, see section 6.

4.5 Calorimeter

LAr Calorimeter

The forward and central region of the H1 detector is enclosed by the LAr calorimeter. The LAr calorimeter is a non–compensating calorimeter with coverage of $4^\circ < \theta < 154^\circ$.
It consists of an inner electromagnetic (ECAL) $\boxed{12}$ and an outer hadronic (HCAL) $\boxed{13}$ part. The electromagnetic part is used for electron and photon detection. The energy deposit of hadrons is measured in both parts. Both calorimeter parts use as active medium liquid argon. The low temperature needed for the liquid phase of the argon is achieved with a cryostat which surrounds the calorimeter. The absorber material in the ECAL is lead whereas in the HCAL stainless steel was used. The material in the ECAL amounts to 20-30 radiation lengths and in the HCAL to 4.7-7.0 interaction lengths. The LAr has 45,000 readout cells. The precision of the electromagnetic and the hadronic energies was determined in test beam measurements [78, 79]. The electromagnetic shower energy can be measured with a precision of $\sigma(E)/E = 12\%/\sqrt{(E/GeV)} \oplus 1\%$ and the hadronic energy with $\sigma(E)/E = 50\%/\sqrt{(E/GeV)} \oplus 2\%$.

SPACAL

At H1 particles in the backward region $155^\circ < \theta < 175^\circ$ of the detector are measured with the Spaghetti calorimeter (SpaCal [70]). This calorimeter was designed for the detection of charged and neutral particles as a scintillating fibre calorimeter with lead as absorber material. The precise measurement of electrons with a relative energy resolution of $\sigma(E)/E = 7\%/\sqrt{(E/GeV)} \oplus 1\%$ is achived with the electromagnetic part of the SpaCal, see [80]. In addition the calorimeter has a separated hadronic part.

In the present thesis the SpaCal is used for identifying the photoproduction regime with a veto on a scattered electron in the SpaCal.

4.6 Luminosity Measurement

The luminosity measurement is performed with the Bethe–Heitler process, a purely electromagnetic process with a precisely known cross section. In this process the electron and proton scatter elastically and the lepton radiates an additional photon, $ep \rightarrow ep\gamma$.

The radiated photon is used to determine the rate of the Bethe–Heitler process. It is detected with a photon detector at $z = -101.8\,\mathrm{m}$. The photon detector is designed as an electromagnetic, sampling calorimeter. The active medium is composed of scintillating quartz fibres and the absorber is tungsten. In addition, background suppression is reached with a beryllium filter and a water Cerenkov counter.

The charged lepton is not detected within the calorimeter because it is deflected by the magnetic field of the HERA magnets. It is possible to detect the electron with the electron tagger which is located at $z = -5.4\,\mathrm{m}$. The electron measurement is used for cross checks of the luminosity measurement.

Further details of the composition and location of the detectors of the luminosity system can be found in [81].

4.7 Trigger System

In high energy physics trigger systems are used to reduce the data rate to a storable size by selecting the interesting physics events. At the H1 experiment the electrons and protons bunches cross every $96\,\mathrm{ns}$ which corresponds to a bunch crossing rate of $10.4\,\mathrm{MHz}$. A four level trigger system [69] selects events which originate from ep interactions. The final H1 readout rate is around $10\,\mathrm{Hz}$.

On each of the trigger levels a rate reduction is performed. The latency for the decision time and the complexity of the decision algorithms increases towards higher trigger levels. To reject events as fast as possible on each trigger level the readout can be aborted. In figure 4.7 a schematic view of the H1 trigger system is shown.

Level 1

The shortest decision period of $2.3\,\mu s$ is allowed at the first trigger level [82]. The data are stored in a pipeline such that no dead time occurs. The central trigger logic receives the information generated from different subdetectors also called trigger elements. At H1 256 trigger elements

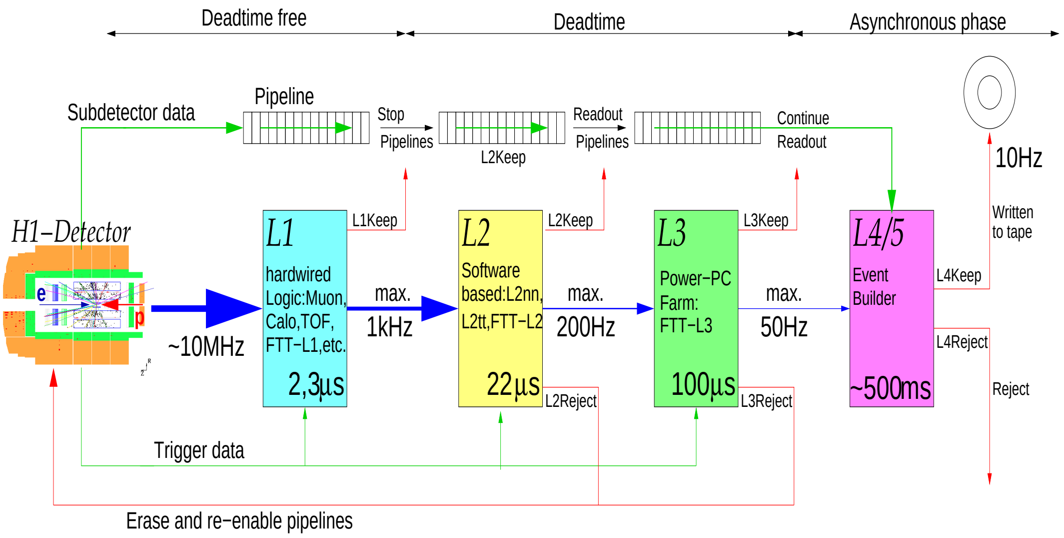

Figure 4.7: *Sketch from [83] of the four trigger layers of the H1 trigger system.*

exist which are combined by the central trigger logic to 128 subtriggers (s1-s128).
If at least one subtrigger condition is fullfilled the central trigger decides $L1Keep$. The pipeline is stopped and the dead time begins. If not the pipelines remain open. After level 1 the data rate is of order 1 kHz.

Level 2

After an $L1Keep$ decision of the first trigger level, the rate is reduced to about 200 Hz at the second trigger level [84]. During $22\,\mu s$ the decision has to be derived. The longer latency is used for further event analysis. The trigger information of the subdetectors were combined at the second level to 96 trigger elements, which were further combined to subtrigger elements in the central trigger logic. Three independent level 2 systems, the topological trigger L2TT [85], the neural net trigger L2NN [86] and the level 2 of the Fast Track Trigger [74] contribute to the L2 decision. A level 2 subtrigger validates certain level 1 subtriggers.
The H1 readout begins if a positive decision was made on level 2, $L2Keep$. In contrast if the event is rejected, $L2Reject$, it will be erased and no longer stored. In addition the pipeline is again activated for the next event.

Level 3

The third trigger level is realized with the third level of the Fast Track Trigger. A detailed description of the third trigger level of the FTT can be found here [83, 87–89]. The level 3 trigger system decides within $100\,\mu s$ if the level 1 and 2 decisions are valid. On this trigger level it is possible to perform searches for special particle decays and event topologies. The FTT analyses track based information together with additional information from the calorimeter and muon systems. After a positive decision of the central trigger logic, $L3Keep$, the event is fully read out. A negative signal, L3Reject, leads again to the erasure of the event and an opening of the pipeline. As soon as an event is rejected the readout is aborted. The output rate is reduced to a rate of maximal 50 Hz.

Level 4

The last step of rate reduction is done on the fourth trigger level and is asynchronous to the HERA clock. It has a latency of $500\,\mathrm{ms}$. The input rate has to be lower than 50 Hz because for higher rates the dead time rises significantly. It is necessary to have a short dead time because it is not possible to record a new event during the dead time such that interesting events may be lost. The event which has passed the lower trigger level is transferred to a PC computer farm. Here the full detector information is available. After passing the H1 reconstruction software H1REC the incoming event is classified into event classes. Remaining events from beam gas and beam wall interaction which have not been rejected earlier by the level one trigger decision with the usage of the CIP2k are removed. After this step the data is written to tape. The output rate is around 10–20 Hz with an event size of 100–150 kByte.

In addition to events which had a positive level 4 decision some other events with a negative level 4 decision are stored too. Very frequent occur events which do not match any of the event classes and have a low Q^2. The rate of such soft physics processes is reduced by prescaling of a factor of 10 such that only every 10th event is recorded.

Prescales

The problem occurs that the input rate for a following higher trigger level is too high or even that the remaining event rate after the use of all trigger levels is not low enough for storage. Then additional rate reduction is achieved by assigning prescale factors. Each of the level 1 subtriggers gets a prescale factor n. The rate reduction for a subtrigger with prescale n is achieved by recording only every n^{th} event satisfying the subtrigger condition. The value of the prescale factor depends on the priority of the subtrigger element. No prescales are assigned to high priority subtriggers. Low prescales of order 1 or 2 get those subtriggers which have high priority but in addition a high rate. An example for such triggers are the FTT L3 photoproduction triggers used in the present thesis. The rate of subtriggers and therefore the prescales depends on the running conditions like beam currents and background rates.

FTT

At small Q^2 the cross section increases strongly which results in high physics rates. For triggering photoproduction events the three level Fast Track Trigger (FTT) [74, 75, 90–93] is used. After the HERA-machine upgrade in the years 2001-2002 a higher luminosity and interaction rate was achieved and a new trigger system, the FTT, was needed for sufficient rate reduction. Since then the third level of the FTT is implemented as the third trigger level of the H1 trigger system. The FTT performs a search for track segments in 12 wire layers of the CJCs. In addition a precise on-line track reconstruction is done on trigger level.

FTT Level 1

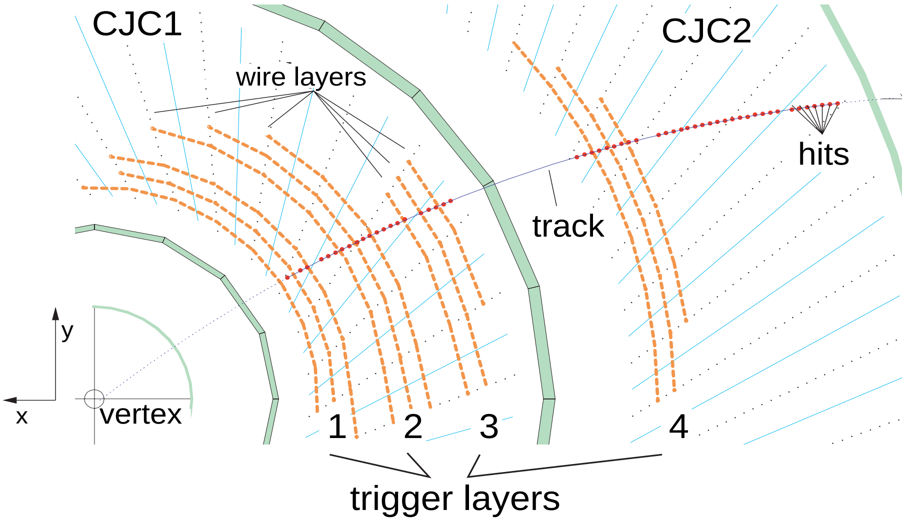

Figure 4.8: *Illustration of the H1 Central Jet Chambers in the xy plane, adopted from [74]. For the Fast Track Trigger 12 of the 56 CJC wire layers were grouped into 4 so–called trigger layers.*

The Fast Track Trigger uses tracking information from the H1 Central Jet Chambers to select events. Therefore a track segment search is performed in four trigger layers. 12 of the 56 CJC wires were used, with three wires organized in one trigger layer, see figure 4.8. Three layers are in the inner chamber CJC1 and the fourth is situated in the outer CJC2. With a rate of 80 MHz the signal of both wire ends are sampled. They are digitized by a fast Qt algorithm. Then the hits are send into shift registers. The method of charge division is used to determine the z position [90].

At the first trigger level the effective sampling rate amounts to 20 MHz. The track segments search is performed by comparing the hit information, which was stored in the shift registers, to pre-calculated masks of possible tracks originating from the interaction vertex. The identified track segments are filled into $\kappa - \phi$ histograms with 16x60 bins. Here κ denotes the track curvature, which can be derived from the measurement of the transverse momentum and the magnetic field in the CJC. The low number of bins of the $\kappa - \phi$ histograms limits the resolution. The linking of track segments to tracks is done with a sliding window technique. If at least two out of the four layers show coincidences the track segments are linked together. The trigger decision takes into account the number of tracks above certain p_T thresholds and decides within a latency of $2.3\mu s$.

FTT Level 2

The second level of the FTT uses information of shift registers which were filled with the full bandwidth of $80\ \mathrm{MHz}$ of the sampling rate. The decision time is $23\mu s$. As at the first trigger level a track finding is performed but now with a much higher resolution. The linking is redone but with a finer binning of 60x640 bins in $\kappa - \phi$. As for level 1 for the linking of track segments coincidences are required in two out of four layers.
The curvature κ and the angles ϕ and θ are determined by fits. For κ and ϕ a non-iterative helix track fit [94] was applied which uses the x,y position of the track segments. The angle θ is found by a linear fit of the z position of the track segment. The FTT was designed for the reconstruction of up to 48 tracks per event on level 2. Searches for exclusive final states can be performed but are limited to a search for particles which decay to two particles because of the short trigger decision time.
The level 2 trigger elements decide with respect to the amount of tracks above a certain threshold in transverse momentum, event topologies and more complex conditions on the invariant mass of two body decays and the track quality. Finally the decision is sent to the central trigger.

FTT Level 3

Events with more complex topologies like charm or beauty production with the reconstruction of particle decays can be selected with the third trigger level. Selection algorithms for D^* , inelastic J/ψ , electron and muon identification are implemented to select the interesting events on-line. On this trigger level not only the CJCs are providing information, other detectors like the muons system are used as well. The trigger decision is made within $130\mu s$ and a negative decision implies an abortion of the H1 readout.
For the present analysis the D^* triggers have been used. In the following the selection algorithm of D^* mesons in the golden decay channel will be explained.
D^* mesons are identified by the three tracks of the three charged final state particles. On-line no particle identification is implemented and the full combinatorics have to be analysed. First the D^0 candidate is reconstructed by combining two tracks with opposite charges under the kaon and pion mass hypothesis. It is required that the transverse momentum of each the two tracks is above a certain transverse momentum threshold. Then the invariant mass is calculated and checked to be within a mass window of $180\ \mathrm{MeV}$ around the nominal D^0 mass.
The tracks of the D^0 candidates are then combined with a third track which corresponds to the π_{slow}. The invariant mass of the D^0 and $K\pi\pi_{slow}$ are calculated. A D^* candidate has to fulfill $\Delta M < 180$ or $\Delta M < 280\ \mathrm{MeV}$ depending on its transverse momentum, where $\Delta M = M(D^*) - M(D^0)$. If the requirement is not fulfilled no D^* is identified and other track combinations are checked.

In particular three D^* triggers with different transverse momenta and invariant mass cuts have been used in the present analysis. Two triggers have the same invariant mass cut of $\Delta M < 180\ \mathrm{MeV}$ but different cuts in the transverse momenta. The low p_T trigger cuts at $p_T > 1.5$ GeV, the medium p_T trigger at $p_T > 2.5$ GeV. The third, high p_T D^* trigger requires $\Delta M < 280\ \mathrm{MeV}$ and $p_T > 4.5$ GeV, for more details see [95].

Chapter 5

Simulation of the Energy Loss of Particles in the CJC

5.1 Specific Energy Loss in the CJC

The two central jet chambers of the H1 central tracking system are designed as drift chambers for the momentum measurement. The momentum p of a charged particle is obtained from the properties of the particle track in the magnetic field in the chamber. In addition the specific energy loss $\mathrm{d}E/\mathrm{d}x$ of particles is measured. The energy loss depends mainly on the velocity $\beta = \frac{v}{c}$ of the particle. The momentum and $\mathrm{d}E/\mathrm{d}x$ information together allow to draw conclusions on the mass of the particle and the particles identity.

Within the software H1SIM the specific energy loss in the CJCs is simulated, and the track reconstruction is performed within the software package H1REC. However not only the theoretical energy loss is simulated, several expected detector effects are simulated too. To identify particles the comparison of the measured and predicted energy loss is needed. The measured $\mathrm{d}E/\mathrm{d}x$ in MC needs corrections for the detector effects. In the following the $\mathrm{d}E/\mathrm{d}x$ simulation and the corrections for detector effects are described.

Mean Energy Loss: The Bethe–Bloch Equation

Within the energy regime studied with the H1 experiment the energy loss of particles traversing through the CJC happens predominantly via ionization or atomic excitation of the material. The mean energy loss $\mathrm{d}E/\mathrm{d}x$ of charged particles can be described by the so called Bethe–Bloch formula [96, 97], [98, eq. 23.1]:

$$-\frac{\mathrm{d}E}{\mathrm{d}x} = \frac{1}{2}\,\frac{K\rho Z}{A}\,\frac{z^2}{\beta^2}\left(\ln\frac{2\,\mathrm{m}_e\,\beta^2\gamma^2\,T_{max}}{I^2} - 2\beta^2 - \delta\right), \tag{5.1}$$

where z is the charge of the incident particle, β is the velocity of the incident particle, $\gamma = (1-\beta^2)^{-1/2}$, Z and A are the atomic charge and atomic mass of the absorber, m_e is the electron mass and K is given by equation 5.2. The constant K is defined as

$$K = 4\pi N_A r_e^2 m_e c^2, \tag{5.2}$$

with the Avogadro number N_A and the classical electron radius r_e. I represents the mean excitation energy and T_{max} is the maximum energy transfer per single collision, which is given by [98, eq. 23.2]:

$$T_{max} = \frac{2\,m_e\,\beta^2\gamma^2}{1+2\gamma m_e/M+(m_e/M)^2}, \tag{5.3}$$

where M is the mass of the incident particle.

Further the Bethe–Bloch formula needs the density correction δ. This density correction has been calculated by Sternheimer [99] and depends on $X = p/M = \beta\gamma$:

$$\delta = \begin{cases} 2\ln 10 \log_{10} X + C + a\,(X_1 - X)^m & \text{for } X_0 < X < X_1 \\ 2\ln 10 \log_{10} X + C & \text{for } X > X_1 \end{cases} \tag{5.4}$$

The parameters C, a, m are material constants. Here it should be noted that $2\ln 10 \log_{10} X = \ln X^2 = \ln \beta^2\gamma^2$.

Therefore the specific energy loss for a particle traversing through matter has the following behavior: First the energy loss falls with $\sim 1/\beta^2$ with increasing $\beta\gamma$. Then, after it has reached the minimum ionization energy, the so called relativistic rise with $\ln \beta^2\gamma^2$is observed. Finally it remains at a constant value at the so called Fermi plateau.

In case that $\gamma \ll M/m_e$, or $M \to \infty$ one can approximate

$$T_{max} \approx 2\,m_e\,\beta^2\gamma^2. \tag{5.5}$$

This approximation is not valid for electrons With this the specific energy can be calculated as

$$\begin{aligned} -\frac{\mathrm{d}E}{\mathrm{d}x} &= \frac{1}{2}\,\frac{K\rho Z}{A}\,\frac{z^2}{\beta^2}\left(\ln\frac{(2\,\mathrm{m}_e\,\beta^2\gamma^2)^2}{I^2} - 2\beta^2 - \delta\right) & (5.6)\\ &= \frac{K\rho Z}{A}\,\frac{z^2}{\beta^2}\cdot\left(\ln\frac{2\,\mathrm{m}_e\,\beta^2\gamma^2}{I} - \beta^2 - \frac{1}{2}\delta\right). & (5.7) \end{aligned}$$

In this approximation the constant plateau value will not be reached, because for very large values of $\beta\gamma$ the relativistic rise term $\ln \beta^2\gamma^2$ is no longer compensated by $\delta/2 = 1/2 \ln \beta^2\gamma^2$. But by using a density correction multiplied by a factor of 2, as was done by e.g. JADE, OPAL [100] and Steinhart [101], this can be prevented:

$$\begin{aligned} -\frac{\mathrm{d}E}{\mathrm{d}x} &= \frac{K\rho Z}{A}\,\frac{z^2}{\beta^2}\cdot\left(\ln\frac{2\,\mathrm{m}_e\,\beta^2\gamma^2}{I} - \beta^2 - \delta\right) & (5.8)\\ &= \frac{K\rho Z}{A}\,\frac{z^2}{\beta^2}\cdot\left(\ln\frac{2\,\mathrm{m}_e}{I} + \ln\,\beta^2\gamma^2 - \beta^2 - \delta\right). & (5.9) \end{aligned}$$

For electrons and positrons the Bethe–Bloch equation has to be modified [102], but this is not implemented in H1SIM.

5.2 Energy Straggling Distribution

When simulating the real behavior of particles depositing energy one has to consider that ionization has a statistical nature, such that the deposited ionization energy fluctuates statistically around the mean value. The fluctuation follows a distribution called energy straggling distribution. For most cases the Landau distribution can be used which has a long tail towards high energies. Hence large fluctuations occur in reality. In H1SIM four approximations which take into account this fluctuations and the configuration of the absorber material are in use and will be presented. For this the quantity κ is introduced with

$$\kappa = \frac{\xi}{T_{max}}, \tag{5.10}$$

where ξ is the mean energy loss in a collision ξ is defined with respect to the Rutherford scattering cross section by

$$\xi = \frac{1}{2} K \left\langle \frac{\rho Z}{A} \right\rangle \frac{z^2}{\beta^2} \Delta x. \tag{5.11}$$

κ denotes the ratio of the mean energy loss to the maximum allowed energy transfer in a single collision with an atomic electron. Here, Δx is the layer thickness of the material.

With this quantity it is possible to distinguish between several approximations for the energy straggling:

- $\kappa > 10$: Gaussian approximation
- $0.02 < \kappa < 10$: Vavilov approximation
- $\kappa < 0.02$: Landau approximation
- very thin layers: Urban Model

In the following the energy straggling approximations will be explained in detail.

Landau Approximation

In H1SIM the Landau approximation is used for $\kappa < 0.02$. For these small values of κ, the probability f for the particle depositing an energy ϵ is given by (see e.g. [103], [53])

$$f_L(\epsilon) = \frac{1}{\xi} \phi(\lambda) \tag{5.12}$$

with the universal Landau function [104] ϕ and the parameter

$$\lambda = \frac{\epsilon - \langle \epsilon \rangle}{\xi} - 1 + \gamma_E - \beta^2 - \ln \kappa. \tag{5.13}$$

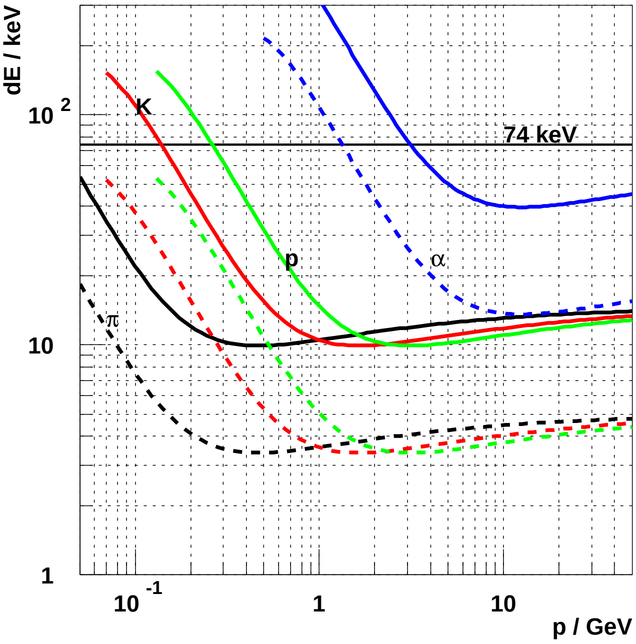

Figure 5.1: *Bethe-Bloch function as used in the H1 detector simulation (in collaboration with [105]). The energy loss* $\mathrm{d}E$ *is depicted for different particles and different absorber thickness of* $1\,\mathrm{cm}/\sin\theta$ *with* $\theta = 90°$*(dashed lines) and* $\theta = 20°$ *(continuous lines). The black vertical line denotes the valid range for the Urban model which is used for energy losses below* $(500 \cdot I) = 74\,\mathrm{keV}$ *with* $I = 147$ *eV.*

Here γ_E is the Euler's constant $\gamma_E = 0.577215$ and the mean energy loss $\langle\epsilon\rangle = -\mathrm{d}E/\mathrm{d}x$ as given by the Bethe–Bloch formula, see equation (5.1).

The computation of the Landau distribution is performed with routines provided by the CERN library [106][1]. With this routines a random variable distributed according to $\phi(\lambda)$ is generated from a random number that is distributed evenly between 0 and 1. As output the inverse of the integral of the Landau distribution is given. The energy loss ϵ can be determined with λ by

$$\epsilon = \xi\left(\lambda + 1 - \gamma_E + \beta^2 + \ln\,\kappa\right) + \langle\epsilon\rangle. \tag{5.14}$$

The Landau formalism reveals a problem when summing up the fluctuations to determine the average value of the Landau distribution. The determined value is not the same as the measured average $\mathrm{d}E/\mathrm{d}x$ value. In order to have the correct average for the mean energy loss, it is required that for the mean value of λ holds [53, sect. PHYS332]

$$\langle\lambda\rangle = -1 + \gamma_E - \beta^2 - \ln\,\kappa. \tag{5.15}$$

For this an upper cutoff λ_{max} for λ is introduced and λ_{max} is set to [53, sect. PHYS332]

$$\lambda_{max} = 0.60715 + 1.1934\,\langle\lambda\rangle + (0.67794 + 0.052382\,\langle\lambda\rangle)\,\exp\left(0.74442 + 0.94753\,\langle\lambda\rangle\right). \tag{5.16}$$

---

[1] Based on the work presented in [107].

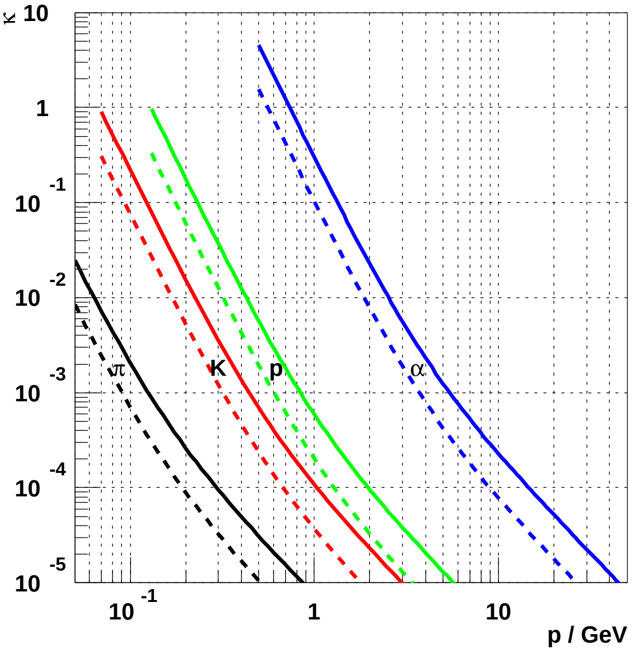

Figure 5.2: *Value of* $\kappa = \xi/T_{max}$ *(see text) for* $1\,\mathrm{cm}/\sin\theta$ *of gas, assuming* $K\langle Z\rho/A\rangle = 247$ *eV*$/\mathrm{cm}$, *for pions, kaons, protons and alpha particles as a function of their momentum* p, *for* $\theta = 90°$*(dashed lines) and* $\theta = 20°$*(continuous line), respectively (in collaboration with [105]). The different colors denote different particle types.*

However, for very thin absorbers additional complications arise: The Landau theory is only valid if the mean energy loss is small compared to the maximal energy loss in a single collision (which corresponds to a small value of κ), but it assumes that the average energy loss is still large compared to the energy levels of the absorber atoms or molecules. Hence the Landau approximation demands that the energy is transferred in many collisions.

In very thin absorbers this assumption is no longer valid. A detailed modelling of energy losses in very thin absorbers, which is typically based on the photo-absorption model, is quite complex and unsuitable for a fast simulation. However, GEANT contains a simplified model from Lassila-Perini and Urban [108], which gives a reasonable approximation sufficient for the CJC simulation.

Urban Model

The Landau approach is not a good approximation for the energy loss in very thin layers. Hence the Landau approximation is not used for the simulation of the specific energy loss in gaseous detectors like the CJCs of the H1 detector. A minimal ionizing particle (MIP) traversing $1\,\mathrm{cm}$ of gas in the CJC deposits around $3.5\,\mathrm{keV}$ of energy and the energy losses are comparable to the binding energies of the inner electrons. An approach which considers the atomic energy levels is needed to get an appropriate simulation. In H1SIM the model of Lassila-Perini and

Urban [108], [53, sect. PHYS332] is used. This model has a smoth transition to the Landau form for mean energy losses which are large comparable to the binding energies of the inner electrons. For the CJC gas mixture of Argon and C_2H_6 the mean ionisation potential I is calculated with the 'mean' Z of the CJC gas mixture: $I = 16eV \cdot 0.5 \cdot (Z_1^{0.9} + Z_2^{0.9})$ with $Z_1 = 18$ for Argon and $Z_2 = 6$ for C. If the energy loss is not much larger than the mean ionisation potential (the cut in H1SIM is $500 \cdot I$) the Urban model is used.

For the Urban model an atom is approximated to have only two energy levels E_1 and E_2. The mean energy loss in a step is here the sum of the excitation and ionization contributions

$$-\frac{\mathrm{d}E}{\mathrm{d}x}\Delta x = [\sigma_1 E_1 + \sigma_2 E_2 + \sigma_3 \int_I^{E_{max}+I} Eg(E)dE]\Delta x \tag{5.17}$$

with the mean ionization energy I, the upper energy cut for δ-ray production E_{max}, the macroscopic cross-section for excitation σ_i (i=1,2) and the macroscopic cross-section for ionization σ_3. The distribution of the energy loss due to the ionization $g(E)$ is proportional to $1/E^2$ and fulfills

$$\int_I^{E_{max+I}} g(E)dE = 1. \tag{5.18}$$

This denotes an ionization with such an energy loss $g(E) = \frac{(E_{max}+I)I}{E_{max}}\frac{1}{E^2}$.

Fig. 5.3 shows the simulated $\mathrm{d}E/\mathrm{d}x$ values for various values of the gas layer thickness and different particles. In the top row the simulated specific energy loss for minimal ionizing pions with a $\beta\gamma$ of 3.5 is presented. The right plot shows the $\mathrm{d}E/\mathrm{d}x$ distribution for different layer thickness of $1\,\mathrm{cm}$, $2\,\mathrm{cm}$ and $4\,\mathrm{cm}$ of gas. The peak gets broader with decreasing layer thickness. In addition the peak position changes. On the left the more symmetric distribution for $1/\sqrt{\mathrm{d}E/\mathrm{d}x}$ is depicted.
The lower row shows the $\mathrm{d}E/\mathrm{d}x$ and $1/\sqrt{\mathrm{d}E/\mathrm{d}x}$ for a layer thickness of $1\,\mathrm{cm}$ gas for pions, protons and electrons.

Vavilov Approximation

In H1SIM the Vavilov approximation [109] is used for values of $0.02 < \kappa < 10$.

The straggling distribution is defined as

$$f_V(\epsilon) = \frac{1}{\xi}\,\phi_V(\lambda, \kappa, \beta^2) \tag{5.19}$$

with the Vavilov function $\phi_V(\lambda, \kappa, \beta^2)$ and the parameter

$$\lambda = \frac{\epsilon - \langle\epsilon\rangle}{\xi} - 1 + \gamma_E - \beta^2 - \ln\kappa. \tag{5.20}$$

Like the Landau distribution it depends on a variable λ , but in addition its functional form depends on β and κ.

The Vavilov function automatically has the correct mean value, so that no cut on λ has to be employed.

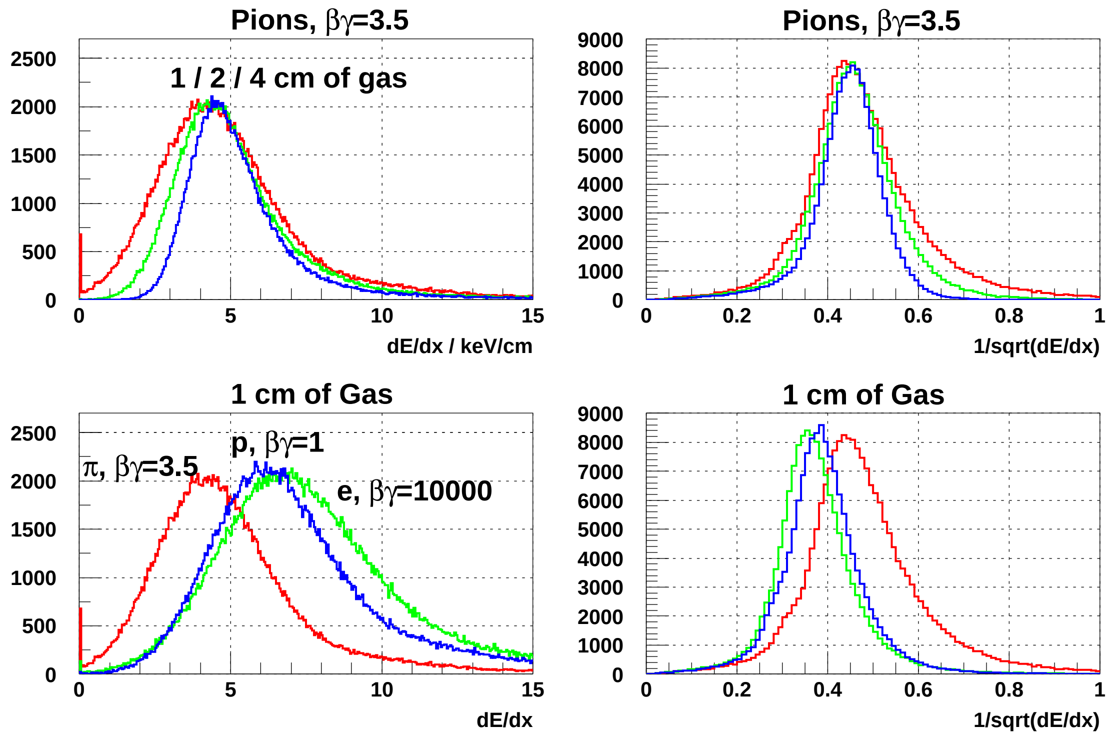

Figure 5.3: The new $\mathrm{d}E/\mathrm{d}x$ distribution for minimal ionizing pions for different values of the layer thickness of $1\,\mathrm{cm}$ (red), $2\,\mathrm{cm}$ (green) and $4\,\mathrm{cm}$ (blue) is depicted in the top row. In the left column the $\mathrm{d}E/\mathrm{d}x$ distribution is illustrated and in the right column the more symmetric $1/\sqrt{\mathrm{d}E/\mathrm{d}x}$ distribution is shown. In the bottom row the $\mathrm{d}E/\mathrm{d}x$ and $1/\sqrt{\mathrm{d}E/\mathrm{d}x}$ distributions for different particle types, pions π, protons p and electrons e, in $1\,\mathrm{cm}$ of gas is presented [110].

Gaussian Approximation

It is possible for large values of κ to approximate the energy straggling function sufficiently by a Gaussian with a width [111, 112]

$$\sigma^2 = \frac{\xi^2}{\kappa}\left(1 - \frac{\beta^2}{2}\right) = \xi\, T_{max}\left(1 - \frac{\beta^2}{2}\right) \tag{5.21}$$

instead of the Vavilov approximation. The appropriate mean value is the mean value predicted by the Bethe–Bloch equation. The Gaussian approximation is used in H1SIM for $\kappa > 10$.

Summary Energy straggling

The new simulation in H1SIM takes into account the thickness of the absorber. This is illustrated in figure 5.1, where the Bethe–Bloch function used in H1SIM is shown for different particle types and for different absorber thickness of $1.\,\mathrm{cm}/\sin\theta$ with $\theta = 90^\circ$ and $\theta = 20^\circ$ as a function of the particle momentum. The Urban model is employed for energy losses in a single cell below $74\,\mathrm{keV}$.

In this diagram particles with energy losses, which are outside the Urban model range, are observed. For the absorber thickness with $\theta = 90°$ the only particles which can reach higher energy losses are α particles with momenta below $1.3\,\mathrm{GeV}$. In addition for the absorber thickness at $\theta = 20°$, also protons with momenta below $0.27\,\mathrm{GeV}$ and kaons below $0.15\,\mathrm{GeV}$ can be located outside the range of the Urban model.

The κ values corresponding to this momenta can be found in figure 5.2. Here the κ values for absorber thickness of $1\,\mathrm{cm}/\sin\theta$ of the CJC gas mixture for different particle types are presented as a function of the particle momentum. The kappa value are shown for angles of $\theta = 90°$ and $\theta = 20°$. It can be observed that for these momenta, the corresponding values of κ are around $0.05 - 1$. In this κ range the Vavilov approximation is valid. In H1SIM the Vavilov approximation is used for κ values between 0.02 and 10.

The Landau approximation is used for κ values below 0.02. Only α particles at shallow angles ($\theta < 20°$) can reach simultaneously κ values below 0.02 and mean energy transfers above $74\,\mathrm{keV}$. Particles with $\kappa > 10$ for which a Gaussian approximation would be applied in H1SIM, are not observed.

In H1SIM the width of the energy straggling function is increased by an additional Gaussian smearing to reach the best agreement with data. The total width is increased with

$$\sigma^2 = \xi\left[(1.7)^2 \cdot 10^{-6}\right]. \tag{5.22}$$

The constant factor was derived with a comparison to the data width.

5.3 dE/dx Parametrization in H1SIM

The parametrization of the specific energy loss distribution in H1SIM is computed with four parameters $PA(i)$ (i=1–4) according to the Bethe–Bloch equation as

$$-\frac{\mathrm{d}E}{\mathrm{d}x} = \frac{PA(3)}{\beta^2}\left(PA(4) + \ln\beta^2\gamma^2 - \beta^2 - \delta\right). \tag{5.23}$$

The density correction is given by

$$\delta = \begin{cases} 2\ln 10(X - PA(2)) + PA(1)\cdot(X_1 - X)^m & \text{for } X_0 < X < X_1 \\ 2\ln 10(X - PA(2)) & \text{for } X > X_1, \end{cases} \tag{5.24}$$

with $m = 3$, $X_0 = PA(2) - PA(1)\cdot\frac{DX^m}{2\ln 10}$, $X_1 = X_0 + DX$
and $DX = \sqrt{\left|\frac{2\ln 10}{PA(1)\cdot m}\right|}$.

The parameter values are taken from the values determined for data in [1] and are summarized in table 5.1.

Parameter	Name	Parameter value H1SIM
a	PA(1)	0.0341
$-C/(2\ln 10)$	PA(2)	-0.442
$K\left\langle\frac{\rho Z}{A}\right\rangle$ [keV/cm]	PA(3)	1.309
$\ln\frac{2\,\mathrm{m}_e}{I}$	PA(4)	6.80
m		3
$I = 2m_e\cdot\exp(-PA(4))$[eV]		569
DX		6.71
X_0		-2.68
X_1		4.03

Table 5.1: *Bethe–Bloch parameters for equation 5.24 used in H1SIM. The parameters are set to the derived values of the data parametrization [1].*

Chapter 6

Calibration and Correction of the Specific Energy Loss

There are several effects which influence the measurement of the specific energy loss and for which the measurement has to be corrected for.

The corrections can be divided into hit level and track level corrections. Hit level corrections are the dependence on the wire layers, on the angle β [1] and the staggering. The threshold effect, the dependence on $\cos\theta$ and for the charge sign of the particle has to be corrected on track level. The saturation effect for which one has to correct in data is not simulated here. In this thesis only the correction for MC simulation are discussed, for data see [1].

6.1 Hit Level Corrections

The measurement of the mean energy loss of a track in the CJC is performed with averaging the single hit charge of the wires. The hit charge originates from particles which have ionized the CJC gas and so have lost energy while passing through the CJC. The electrons which have been produced in the ionization process drift to the wires and deposit their charge, such that the deposited charge is proportional to the initial energy loss of the particle in the CJC. The single hit energy loss follows a Landau distribution with a long tail towards high energies. This implies that large fluctuations can occur for the single $\mathrm{d}E/\mathrm{d}x$ measurement. Hence the mean energy loss is not determined with using the $\mathrm{d}E/\mathrm{d}x$ value but with averaging over $1/\sqrt{\mathrm{d}E/\mathrm{d}x}$, which follows a more symmetric function. Figure 6.1 illustrates the more symmetric shape of the $1/\sqrt{\mathrm{d}E/\mathrm{d}x}$ than of the $\mathrm{d}E/\mathrm{d}x$ distribution.

The raw $\mathrm{d}E/\mathrm{d}x$ measurement has to be corrected for several detector effects. The first correction which has to be applied is the dependence on the wire layers of the energy loss measurement. In the H1 simulation it is considered that the wires close to the edge of the CJCs (wire layer 0, 23-26 and 55) are thicker than the inner wires. In figure 6.2, in the top row, the

---

[1] β denotes the angle between the electron drift direction and the orthogonal to the particle track.

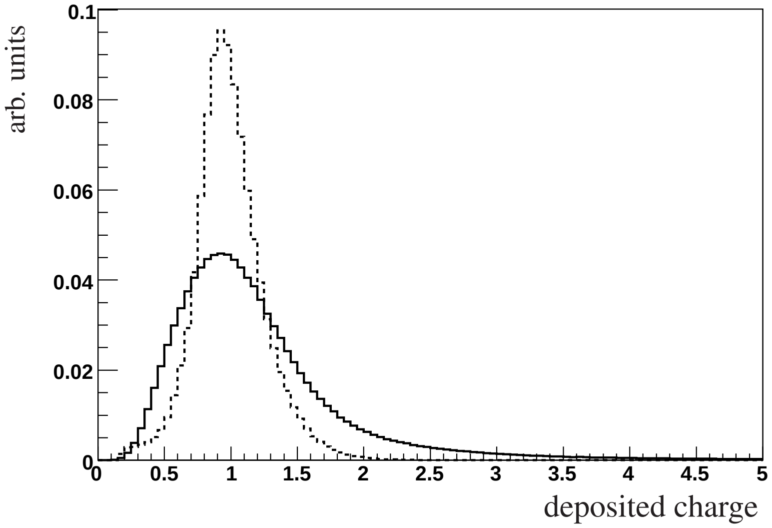

Figure 6.1: *For the determination of the mean specific energy loss the more symmetric* $1/\sqrt{\mathrm{d}E/\mathrm{d}x}$ *(dashed line) instead of the single hit energy loss is used. The* $\mathrm{d}E/\mathrm{d}x$ *(continuous black line) value follows a Landau distribution with a long tail.*

distribution of $1/\sqrt{Q}$, where Q is the deposited charge on the wire, vs wire layer number for single minimal ionizing pions ($\beta\gamma = 3.5$) is shown.

For every wire layer a Gaussian was fitted and the mean of this $1/\sqrt{Q}$ Gaussian distributions is presented in figure 6.2 bottom. This averaging procedure is similar to the determination of the mean $\mathrm{d}E/\mathrm{d}x$ value of a track in the CJC with averaging over the single hits. For the inner wires no correction is necessary; the correction factors for the edge layers are determined from this diagram.

Furthermore the dependence on the angle β, see figure 6.3, and the staggering effect have to be corrected on hit level. This two effects can be studied and corrected together.

β is the angle between the drift direction of the electrons and the orthogonal to the track of the particle. The angle β of a track influences the measured specific energy loss in the following way: If a track is orthogonal to the drift direction then $\mid \beta \mid$ is around zero. All the drift electrons have the same drift length to the wire and reach it nearly at the same time. So the charge pulse is sharp and high and is located fully within the integration interval. If the track has a β different from zero then the electrons arrive at different times on the signal wire. The charge pulse is wider and a larger fraction of the puls is outside the integration interval. So parts of the charge are cut away and the energy loss measurement has to be corrected for this missing charge.

In addition the signal wires do not lay in a line in a layer, they are staggered from the anode layer with $160\,\mu\mathrm{m}$, see figure 6.4. Some of the drift electrons can drift directly to a signal wire but others have to cross the anode layer to reach a signal wire. On this way an electron feels the shielding field from the signal wires in the front of the anode layer. Not all electrons overcome the field and reach the signal wires. So not the whole charge is deposited on the wire.

In figure 6.5 the distributions of the mean $1/\sqrt{Q}$ vs. $\tan\beta$ are presented. It displays the missing of the charge due to the staggering and the dependence on β for electrons which could

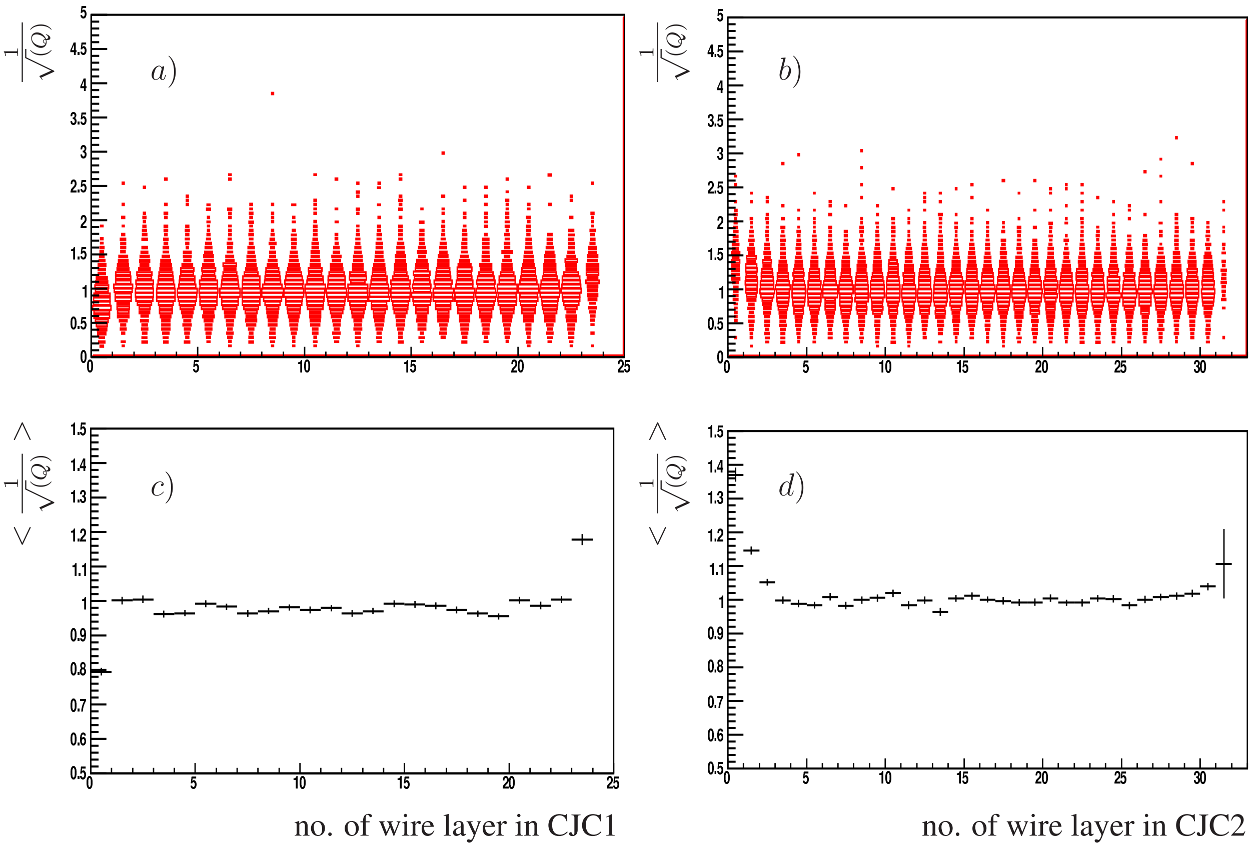

Figure 6.2: *For CJC1(left) and CJC2(right) the distribution of* $1/\sqrt{Q}$*(top) and the mean of this* $1/\sqrt{Q}$ *distributions (bottom) determined with a Gaussian fit vs wire layer numbers, both for minimal ionizing pions (*$\beta\gamma = 3.5$*).* Q *denotes the deposited charge on the wire.*

drift directly to the wire (Figure 6.5 a)) and for electrons which have to cross the wire plane (Figure 6.5 b)). The different height of the minimum of the two distributions exhibits the staggering effect. Electrons which have to cross the wire plane deposit less charge which results in a greater $1/\sqrt{Q}$ value in the minimum than for electrons which can deposit their charge directly. For this diagram single electrons with a momentum in the plateau region of the Bethe-Bloch distribution have been used.

The single hit charge is corrected by a function with the form

$$c_{hit}(\beta, s_{stag}) = (1 + p_1 s_{stag})(1 + p_{2,i} tan\beta + p_{3,i}(tan\beta)^2), \tag{6.1}$$

where the index i accounts for the possibility, that the electrons feel shielding effects because they have to cross the wire plane, or that the electrons can deposit charge directly.

The anode staggering is taken into account with the first parameter p_1 and $s_{stag} = \pm 1$ depending on the position of the wire with respect to the wire plane. The parameters p_2 and p_3 are fitted independently for the two cases that the electrons deposit charge directly or have to cross the plane. Thus in total 5 correction parameters for the single hits are needed.

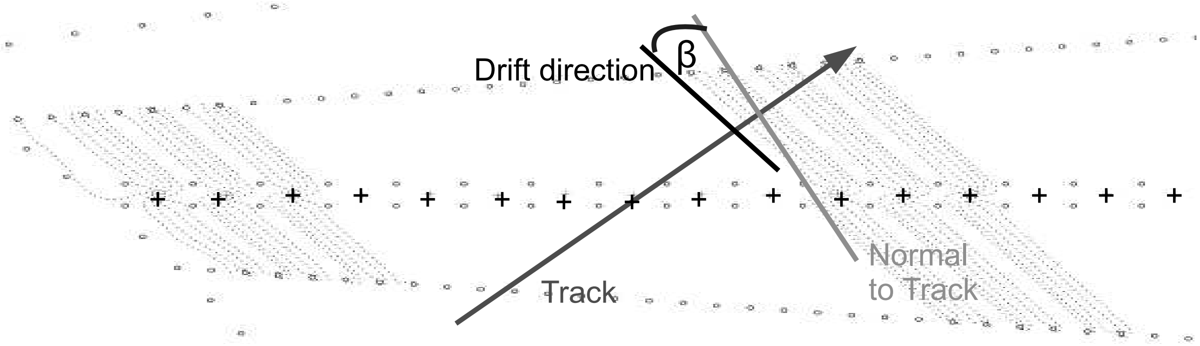

Figure 6.3: *Definition of the β angle in the CJC. The crosses illustrate the signal wires. The open circles are potential and cathode wires. The drift lines of electrons are indicated with the dotted lines.*

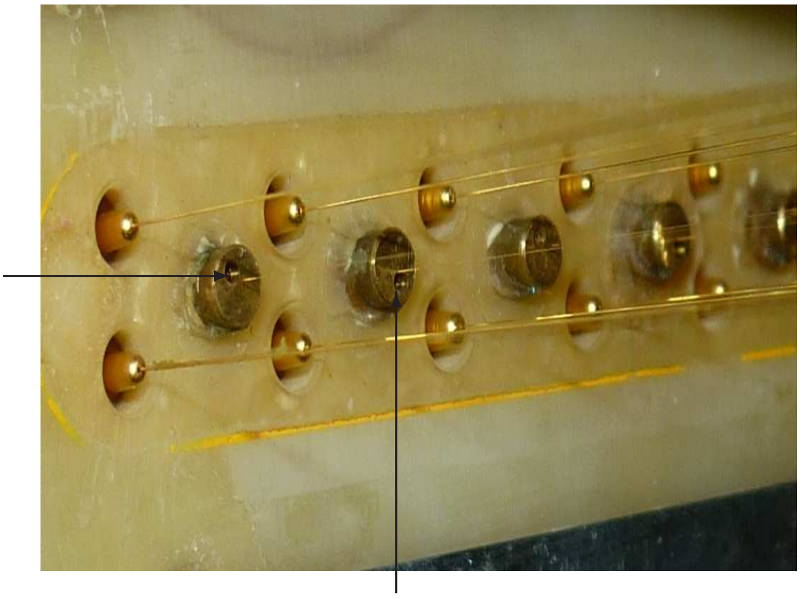

Figure 6.4: *Staggering of the CJC wires [113]*

6.2 Track Level Corrections

The corrections of detector effects on the track level are studied after the correction of the single hits. The first effect which is examined is called threshold effect. In the H1 detector not every hit on a signal wire is detected. For the hit detection it is required that the hit amplitude has to lie above a certain threshold. This results in cutting away an amount of charge from hits which had amplitudes below this threshold. This effect can be studied by plotting the average charge

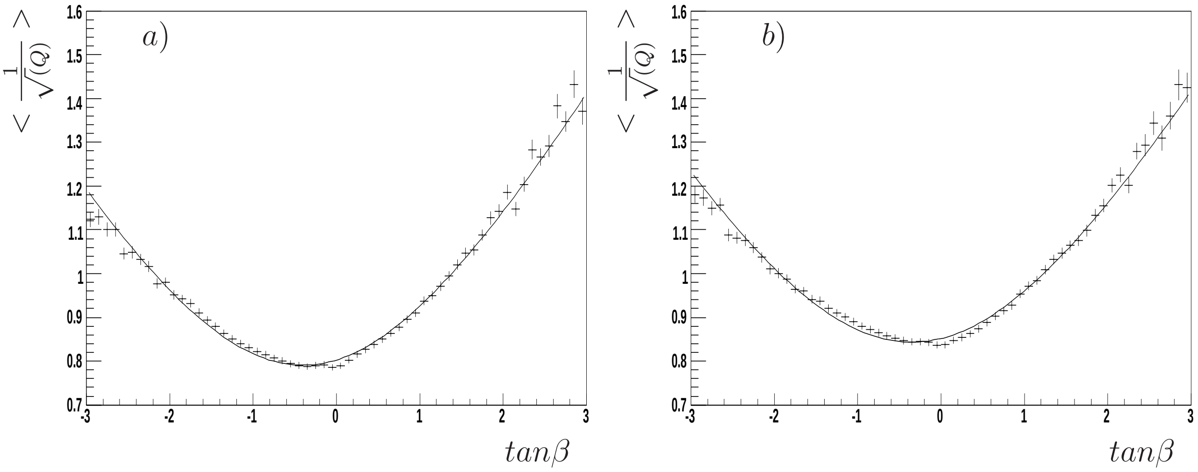

Figure 6.5: *Distribution of* $\tan\beta$ *vs* $1/\sqrt{Q}$ *for electrons which drift directly to a wire in a) and for electrons which have to cross a wire layer in b).*

Q_{mean} of a track divided by the median track charge Q_{med} versus logarithm of the expected charge Q_a. The median of the track charge is determined including the wires crossed by the track without leaving a hit as hits with charge zero. For the calculation of the average charge hits with charge zero are excluded. The expected charge is $Q_a = Q_r \cdot g/\sin(\theta)$, where Q_r denotes the theoretical Bethe-Bloch charge on a wire and g is the CJC gain. The gain includes the gas amplification and has to be chosen with respect to the regarded run period. The default gain for each run period is summarized in table 6.2. The distribution of the ratio of average charge to mean track charge as a function of the logarithm of the expected charge is displayed in figure 6.6 and is fitted with

$$f_{thr}(Q_a) = \frac{Q_{mean}}{Q_{med}} = (1.0 + p_1 Q_a^{p_2}) \qquad (6.2)$$

where the fit results are $p_1 = 0.213$ and $p_2 = -1.228$. As expected the correction is largest for small expected charges Q_a.

The threshold effect can be visualized in addition with another distribution. In figure 6.7 a) the mean energy loss as a function of $\cos\theta$ is shown before the threshold correction. If θ is around 90° the track length within a cell is short. Hence the deposited charge is small and more of the charge is cut away. After correcting for the threshold effect there is no dependence on $\cos\theta$ in the central region with $|\cos\theta| < 0.8$, see figure 6.7b).

In the outer part even after the threshold correction a dependence on θ is visible. This dependence results from the change of the most probable value of the energy loss of a particle which traverses through different thickness of gas. This is displayed in figure 5.3, where straggling distributions for different layer sizes are plotted. The energy loss is corrected for this effect with the fitted polynomial of order 6 with only even orders. The $\mathrm{d}E/\mathrm{d}x$ is corrected for the threshold effect and the parameter values are determined from the $\mathrm{d}E/\mathrm{d}x$ versus $\cos\theta$ distribution with the following fit

$$f_{layerthickness}(cos\theta) = (par1) + (par2 \cdot \cos\theta^2) + (par3 \cdot \cos\theta^4) + (par4 \cdot \cos\theta^6). \qquad (6.3)$$

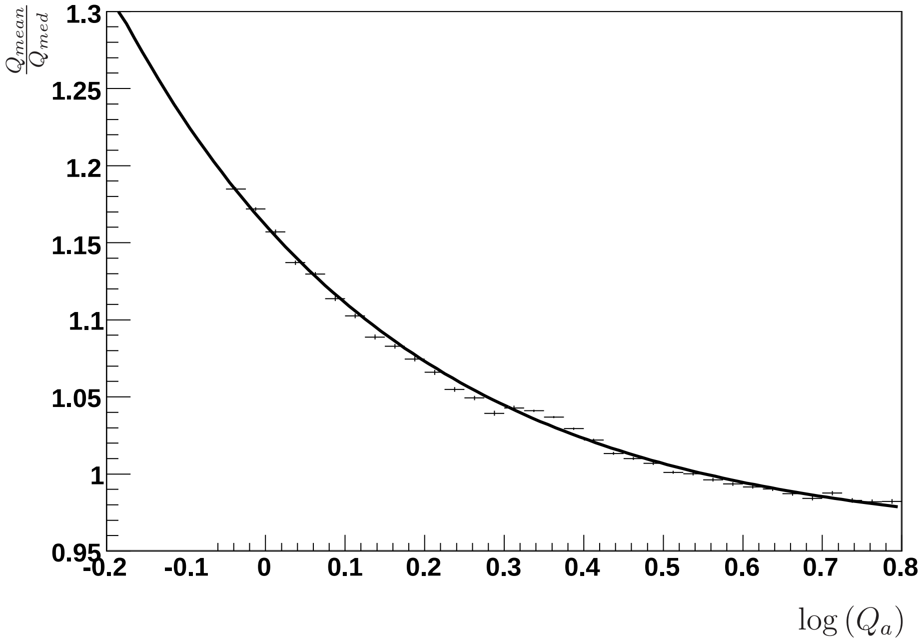

Figure 6.6: *Correction of the threshold effect with the ratio of* Q_{mean}/Q_{med} *as a function of* $\log(Q_a)$. *The fit function is presented in addition.*

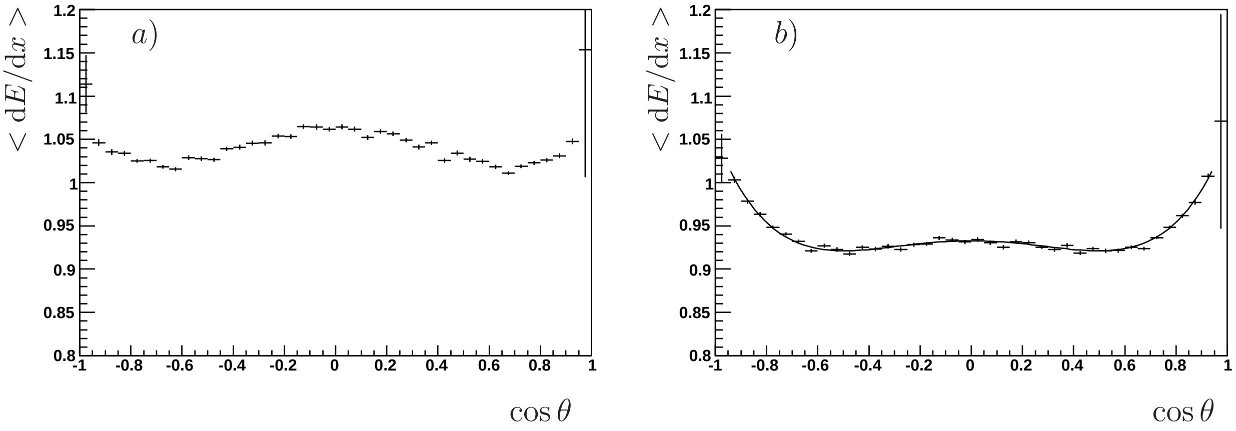

Figure 6.7: *In a) the* $\cos\theta$ *distribution before threshold effect correction was applied is presented. For this figure only negative charged pions of a certain gain period have been used. In b) the threshold effect was corrected. In addition the fit result of the* $\cos\theta$ *correction is shown.*

Run Range	default gain	changes
319331-376810	0.98	
376811-401570	0.98	pressure compensation active
401571-429938	0.95	HV change
429939-433335	1.072	HV change
433336-435283	1.23	HV change
435284-435864	1.23	according to H1 database
435865-445020	1.23	according to H1 database
445021-452777	1.23	according to H1 database + QT code change at run no. 448036
452778-465087	1.19	QT code change
465088-	1.395	HV change

Table 6.1: *Summary of the run periods with constant CJC gain. The HV changes are quoted according to [1].*

Since the CJC cells are tilted, the charge sign of the particles plays a role. Positively charged particles have in the magnetic field the same curvature as the tilt direction of the chamber cells, whereas the negatively charged particles curve in the opposite direction. They have to cross more often the cells than the positive ones. To take into account effects from the charge sign of the particles, the $\mathrm{d}E/\mathrm{d}x$, corrected for the threshold, versus $\cos\theta$ distribution is fitted separately for negative and positive charged particles. In figure 6.7 b) the $\cos\theta$ dependence together with the fit result for negatively charged pions is shown.

During the HERAII run period the high voltage setting of the CJC has changed several times. In addition the QT code was modified twice. These changes are taken into account in the detector simulation. In total 10 different periods have been identified with respect to the gain and QT code changes and according to already existing changes in the H1 database, see table 6.2.

In figure 6.8 the CJC gain in data as a function of the run number for CJC1 and 2 is presented. Before the pressure compensation was operating, before run number 373016, large fluctuations in the gain occur. For each of the constant gain periods the threshold and $\cos\theta$ correction parameters have to be determined separately. The track level correction parameters are stored together with the default gain of the respective run period.

6.3 The Bethe–Bloch Equation in H1REC

Even after all detector effects simulated have been corrected the reconstructed specific energy loss does not follow the $\mathrm{d}E/\mathrm{d}x$ formula used in H1SIM, see equation 5.23. To use the specific energy loss for particle identification a good description of the specific energy loss is required. The parametrisation of the specific energy loss used in H1SIM is modified to describe the MC:

$$\frac{\mathrm{d}E}{\mathrm{d}x} = \left.\frac{\mathrm{d}E}{\mathrm{d}x}\right|_{MIP} \cdot \frac{PA(3)}{\beta^{2PA(5)}} \left(PA(4) + \ln\beta^2\gamma^2 - \beta^2 - \delta\right) . \tag{6.4}$$

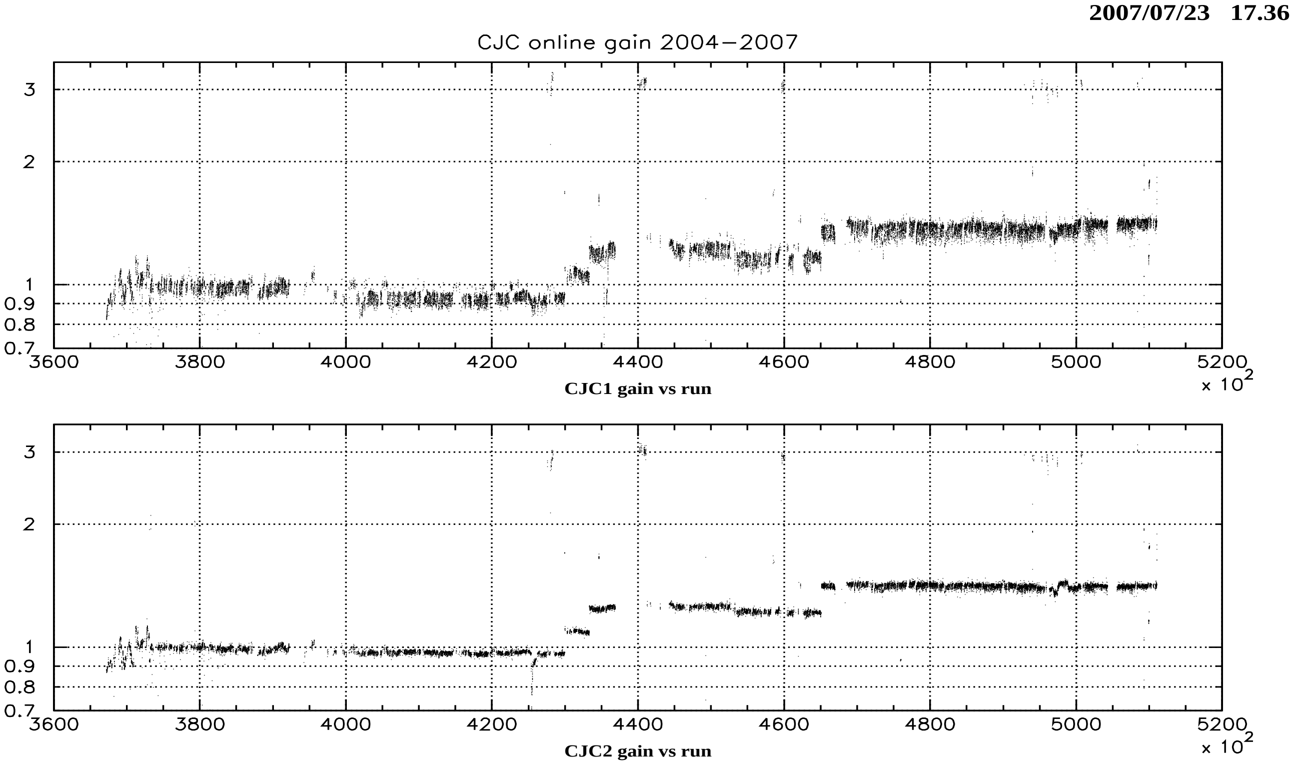

Figure 6.8: *The CJC online gain versus run number for the HERA II run period. Changes due to the QT code version and high voltage settings lead to 10 gain periods, from [67].*

Parameter	Name	parameter for MC	parameter for data
a	PA(1)	0.03167	0.0341 ± 0.0004
$-C/(2\ln 10)$	PA(2)	-0.4495	-0.442 ± 0.009
$K\left\langle \frac{\rho Z}{A} \right\rangle$ $[\mathrm{keV/cm}]$	PA(3)	0.407	0.384 ± 0.006
$\ln \frac{2\,\mathrm{m}_e}{I}$	PA(4)	6.8	6.80 ± 0.04
Exponent of β	PA(5)	1.164	1.10 ± 0.01
Plateau $[\mathrm{keV/cm}]$		1.51	1.44
dE/dx for $\beta\gamma = 3.5$ $[\mathrm{keV/cm}]$		1.00	1.00
Plateau/MIP		1.51	1.44

Table 6.2: *Bethe-Bloch parameters for eqs. 6.4 for the MC parametrization in H1REC and the derived data values from [1].*

An additional parameter $PA(5)$ is introduced to get a better description of the low momenta part of the distribution. The fit parameters of the completely corrected energy loss versus the logarithm of $\beta\gamma$ for the MC simulation have been determined with simulated single protons, electrons, muons, kaons and pions with both charges covering the whole momentum range of particles which could be detected in the CJCs. In table 6.2 the fit parameters for the MC simulation and for comparison for the data are summarized.

The fit parameters of the MC differ slightly from that of the data, although the data values have been used as input for the simulation. The increase from the minimum to the plateau of the Bethe-Bloch distribution amounts in MC to 1.51 and in data to 1.44. In addition an extra parameter $PA(5) = 1.164$ is needed, although a β^{-2} $(PA(5) = 1.)$ dependence was implemented in the simulation. The differences to the simulated specific energy loss can be explained with the additionally simulated detector effects. Overall a good agreement between data and MC is found.

The distribution of the fully corrected specific energy loss as a function of $\log(p)$ is presented with the Bethe–Bloch parametrization in H1REC in figure 6.9 for protons, electrons, muons, kaons and pions. The reference curves for this particle types is shown too.

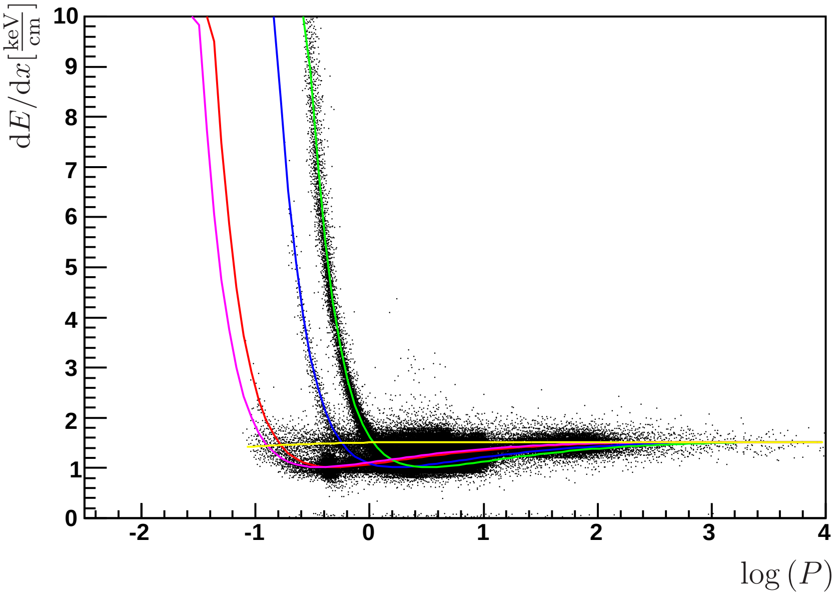

Figure 6.9: *Reconstructed specific energy loss in MC simulation as a function of the logarithm of the particle momentum. The reference curves for electrons (yellow line), protons (green), kaons (blue), pions (red) and muons (pink) are depicted too.*

6.4 Particle Identification in MC

The resolution of the energy loss measurement in MC is determined with all particles used within the Bethe-Bloch fit. The quantity $\Delta(\mathrm{d}E/\mathrm{d}x)$ is defined as $\Delta(\mathrm{d}E/\mathrm{d}x) = \frac{\mathrm{d}E/\mathrm{d}x_{meas} - \mathrm{d}E/\mathrm{d}x_{exp}}{\mathrm{d}E/\mathrm{d}x_{exp}}$ with the measured specific energy loss $\mathrm{d}E/\mathrm{d}x_{meas}$ and the expected $\mathrm{d}E/\mathrm{d}x_{exp}$. It is expected that the resolution has a dependence on the amount of hit counts in the CJCs $\sqrt{N_{hit}}$ as the data. In figure 6.10 the Gaussian fit for $\Delta(\mathrm{d}E/\mathrm{d}x) \cdot \sqrt{N_{hit}}$ for all particles, which are included in the determination of the specific energy loss determination, is presented. The resolution of this Gaussian gives $\sigma = 0.527$. Assuming a typical number of hits $N_{hit} \sim 53.5$ this yields to a relative resolution of $52.7\%/\sqrt{N_{hit}} = 7.2\%$.

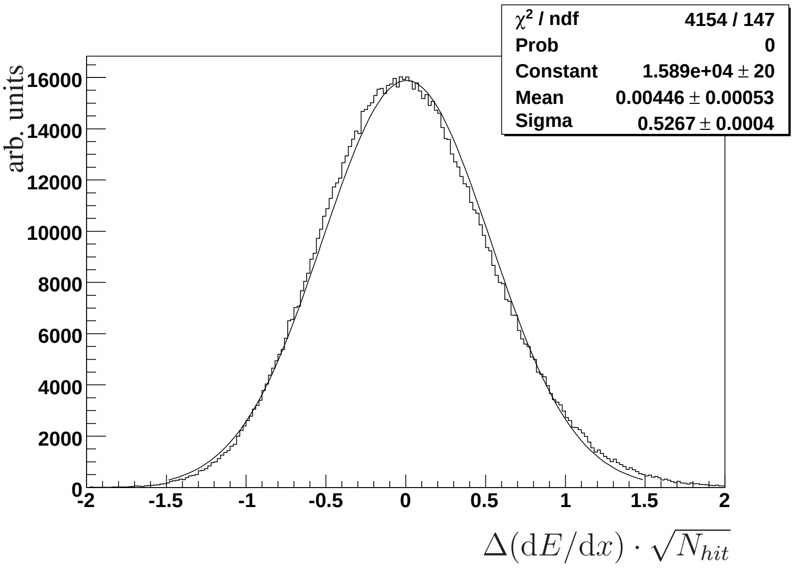

Figure 6.10: *For comparison with data a $\sqrt{N_{hit}}$ dependence of the resolution is assumed. Here $\Delta(\mathrm{d}E/\mathrm{d}x) \cdot \sqrt{N_{hit}}$is fitted with a Gaussian fit for all particles which have been included in the Bethe–Bloch fit determination. The fit result is depicted too.*

In contrast for data a relative resolution of $46\%/\sqrt{N_{hit}} = 6.3\%$ for $N_{hit} \sim 53.5$ was found.

A theoretical prediction of the resolution gives the Lehraus formula [114]

$$\sigma(\mathrm{d}E/\mathrm{d}x)/(\mathrm{d}E/\mathrm{d}x) = 5.7\% L^{-0.37} \tag{6.5}$$

with $L = N_{samp} l_{samp} P[\mathrm{mbar}]$. For data in [1] the number of samples N_{samp} and the sampling length l_{samp} were set to $N_{samp} = 53.0$ and $l_{samp} = 0.87cm$ for long kaon tracks. For a pressure of $P = 1bar$, the $\mathrm{d}E/\mathrm{d}x$ resolution results to 7.6% [1]. Hence the data result is slightly better than the predicted value and the MC result is close to the prediction of the Lehraus formula.

A further study reveales that the assumption of an $1/\sqrt{N_{hit}}$ dependence is not appropriate for the MC. In figure 6.11 the distribution of $\Delta(\mathrm{d}E/\mathrm{d}x)$ as a function of $\sqrt{N_{hit}}$ is presented.

The distribution is fitted with the function

$$f(N_{hit}) = p_1 + p_2/\sqrt{N_{hit}}, \tag{6.6}$$

with the parameters $p_1 = 0.05$ and $p_2 = 0.4684$. This reveals that the resolution has not a $1/\sqrt{N_{hit}}$ dependence as expected. The two resolution paramters are stored in the H1 data base. They are used for the particle identification of a particle track in the CJC which is performed by the determination of the likelihood for the different particle hypothesis.

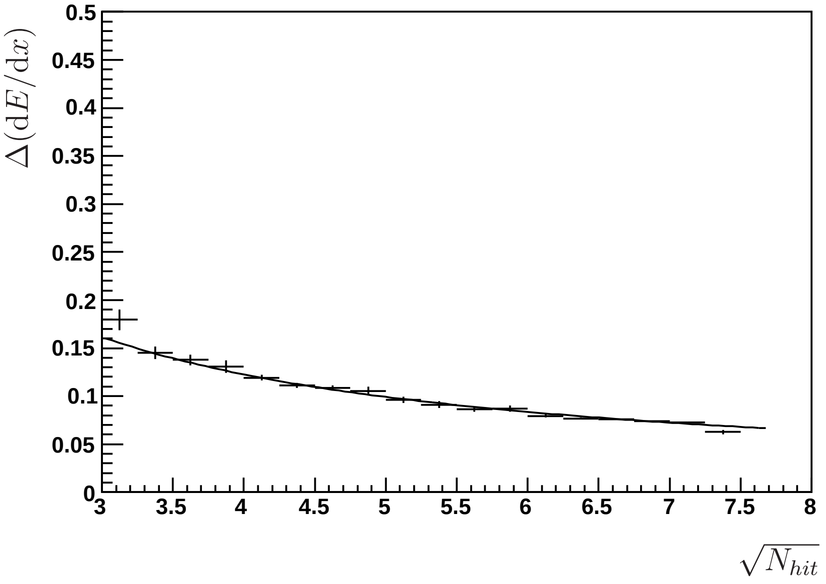

Figure 6.11: $\sqrt{N_{hit}}$ *dependence of the specific energy loss resolution. The fit result is drawn too.*

6.5 Summary Specific Energy Loss Simulation in the CJC

The new simulation of the specific energy loss in the central jet chambers of the H1 was presented in this chapter. The mean energy loss is calculated according to the Bethe–Bloch equation. The energy straggling is implemented with different straggling function which take into account the thickness of the absorber material. The simulated specific energy loss was passed through the H1 detector simulation software. The H1 detector simulation includes the simulation of detector effects too, so that the reconstructed energy loss needs corrections on hit level and on track level. The corrected reconstructed specific energy loss requires a different parametrization as used in the simulation. The resolution follows a slightly different dependence on the amount of CJC hits as the $1/\sqrt{N_{hit}}$ dependence expected from the H1 data.

The new simulation and calibration of the specific energy loss for the HERAII run period improves the H1 track reconstruction with the use of the particle identification information, see section 4.4. Further it has applications in physics analysis, e.g. the electron identification in the measurement of beauty in photoproduction [2]. In the following chapters the analysis of inclusive D^* mesons in photoproduction will be presented. For this analysis the new track reconstruction was used. In addition the background reduction due to the new possibility of particle identification has two main consequences: The D^* signal is improved with the background reduction and the systematic uncertainty is reduced too.

Chapter 7

Event Selection

At H1 data are taken in so called runs. A run is a data taking period during a luminosity fill with stable conditions of the H1 detector. Here a luminosity fill denotes the period from filling electrons and protons into the accelerator to the final beam dump. The runs a categorized into good, medium or poor runs. During a good run the important subdetectors for event reconstruction were operating. For this analysis only good and medium runs are included. In the selected runs high voltage for the following subdetectors are demanded: CJC1 and CJC2, LAr, SpaCal, TOF and the Luminosity system. Moreover it is demanded that the used runs have an integrated luminosity above $0.1\,\mu b^{-1}$.
The selected data sample was taken in the years 2006 and 2007 [1] and corresponds to an integrated luminosity of $\mathcal{L} = 113.14\mathrm{pb}^{-1}$.

To suppress background events coming from satellite bunches, which are located before and after the colliding proton bunch, a cut $|z_{vertex}| < \pm 35\,\mathrm{cm}$ is applied to the z-coordinate of the reconstructed primary vertex. The z_{vertex} distribution is Gaussian and the satellite bunches occur around $\pm 70\,\mathrm{cm}$. The z_{vertex} distribution is simulated run–dependend and can be seen in figure 7.1.

The photoproduction regime is separated by an upper Q^2 cut of $Q^2 < 2\,\mathrm{GeV}^2$ from the DIS regime. This low Q^2 values result in low scattering angles of the scattered electron, such that it is not detected but scattered into the beam pipe. Hence the escaped scattered electron can be used for selecting photoproduction events by requiring a veto on the scattered electron in the calorimeter. In the SpaCal electrons are found and identified by a cluster with an energy deposition greater than $8\,\mathrm{GeV}$ and a radius of less than $4\,\mathrm{cm}$.
In the reconstruction of the hadronic final state (HFS) the problem occurs that some HFS particles are not detected Therefore the reconstruction of the event kinematics is done with the method proposed by Jaquet–Blondel [115] from the hadronic energy flow: The quantity $y_{had} = (E - p_z)_{had}/(2E_e)$ is used, which is insensitive of such losses and can be used to determine the event kinematic properly. Here E_{had} and $p_{z,had}$ denote the energy and the longitudinal momentum of all particles in the HFS and E_e the electron beam energy.

---

[1] In 2006 and 2007 at HERA positrons and protons were collided.

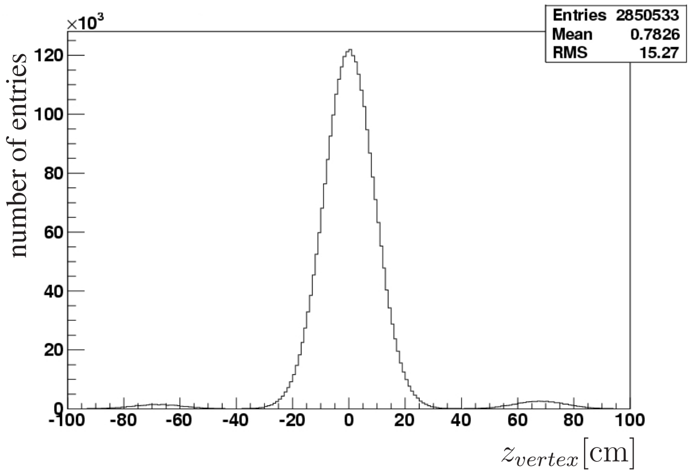

Figure 7.1: *Simulated* z_{vertex} *distribution with satellite bunches around* $\pm 70cm$.

Two cuts restrict the y_{had} range: Events with the final state in the very forward region of the detector are excluded by requesting $y_{had} > 0.1$ and the DIS background is suppressed with $y_{had} < 0.8$. This y_{had} range corresponds to a $W_{\gamma p}$ range of $100 < W_{\gamma p} < 285\,\mathrm{GeV}$.

7.1 Charm Quark Tagging with D^* Mesons

In the present analysis charm quarks in photoproduction are studied. The charm quark in the ep scattering event is identified by reconstructing D^* mesons.
The D^* mesons are reconstructed using the so called golden decay channel $D^{*\pm} \rightarrow D^0 \pi^{\pm}_{slow} \rightarrow K^{\mp}\pi^{\pm}\pi^{\pm}_{slow}$ with a branching fraction of $BR = (2.6 \pm 0.04)\%$ [16]. Because all decay particles are charged it is possible to reconstruct all tracks of the D^* meson decay within the CTD.
The mass difference of D^* and D^0 mesons is close to the π meson mass. This means that the produced pion of the D^* decay has low transverse momentum, it is called slow pion π_{slow}, and can be measured with high precision in the CTD.
In this chapter the ΔM method for the D^* reconstruction will be presented. Further the signal extraction and possibilities for background reduction will be shown.

7.2 D* Recontruction in the Golden Decay Channel

Although the branching ratio of the golden decay channel is relatively small, this decay channel has major advantages: On the one hand the three decay tracks can be measured within the tracking system because every final state decay particle is charged. On the other hand because

of the intermediate D^0 meson and the small mass difference between the D^* and the D^0 meson relatively low background is achieved.
First the $D^0 \rightarrow K^{\mp}\pi^{\pm}$ decay is reconstructed. Two oppositely charged tracks in the event are combined to a pair. The invariant mass is calculated under the kaon and pion hypothesis and is required to be consistent with the D^0 mass, within a certain D^0 mass window.
In the next step an additional track is added under the pion mass hypothesis to the $K^{\mp}\pi^{\pm}$ candidate tracks. This track is demanded to have the same charge sign as the pion from the D^0 decay. The D^* candidates are selected using the mass difference method: The difference of the invariant mass of the D^* and D^0 candidate is determined via the invariant masses of the decay particles $K\pi$ and $K\pi\pi_{slow}$:

$$\Delta M = M(K\pi\pi_{slow}) - M(K\pi). \tag{7.1}$$

For D^* candidates ΔM should be around $145.4\,\mathrm{MeV}$ [16]. The resolution of the mass distributions of the D^* and D^0 separately is given by the large uncertainty of the kaon and pion track. Using the mass difference method the systematic errors from the pion and kaon track measurement cancel to some extend, so that the ΔM resolution is defined by the track measurement of the π_{slow}. This slow particle track can be measured much more accurately, so that the ΔM resolution is much better than of the D^* and D^0 mass distributions.
The tracks which fulfill the charge combination requirement presented so far are called right charge (RC) combinations. In addition, so called wrong charged (WC) combinations exist. Here the kaon and pion tracks from the D^0 decay have the same charge sign and the slow pion has the opposite sign than the pion track. The shape of the WC distribution has a very similar behavior as the non-resonant background shape of the RC distribution.

7.3 Signal Extraction

The number of D^* mesons is determined with a fit to the ΔM distribution. The sum of a signal and a background fit function is used as fit function to discriminate the signal from the sizeable background.
Figure 7.2 reveals that the signal shape is asymmetric and cannot be described by a Gaussian function and a more complicated function is needed.

The tail towards larger ΔM values is due to the slow pion production threshold which can only happen if the mass of the D^* is above the threshold where a pion mass can be produced.

The best parametrization for the signal was found in [116] to be the Crystal Ball [2] function [117]. The Crystall Ball function is a combination of a Gaussian function with a power law. The Gaussian function describes the low ΔM regions and the signal, whereas the power law is demanded by the asymmetry of the peak.
The original Crystal Ball function has the tail on the left side. But here a function is needed with

---

[2] This function was first used at the study of charmonium spectroscopy at the Crystall Ball NaI(Tl) detector at SLAC.

a tail on the other side to describe the ΔM distribution. This Crystal Ball function is defined as a function of the mass difference $m = \Delta M$

$$f(m) = N \cdot \begin{cases} \exp\Big(-\frac{1}{2}(\frac{m-\mu}{\sigma})^2 \Big) & \text{if } \frac{m-\mu}{\sigma} \le -\alpha \\ \frac{(\frac{n}{|\alpha|})^n \exp(-\frac{1}{2}\alpha^2)}{(\frac{n}{|\alpha|} - |\alpha| - \frac{m-\mu}{\sigma})^n} & \text{if } \frac{m-\mu}{\sigma} > -\alpha \end{cases} \tag{7.2}$$

The parameter N corresponds to the normalization parameter, σ is the width and μ the most probable value of the Gaussian function and the parameters α and n set the asymmetry of the tail. The Crystal Ball function is provided by the $RooFit$ package [118].
The background is fitted with a Granet parametrization [119]

$$f(m) = (\delta m)^{p_1} \cdot \exp\big(-p_2 \delta m - (-p_3 \delta m^2) \big) \quad with\ \delta m = (m - m_\pi), \tag{7.3}$$

where p_i are the fit parameters.
It is expected that RC background and WC distribution have the same shape, so that for constraining the shape of the RC background a simultaneous fit of the RC and WC ΔM distributions is performed. Therefore the WC distribution sets the shape of the RC background and the relative normalization of the background function is left free during this simultaneous fit. The WC distribution of the total sample is presented in figure 7.2.

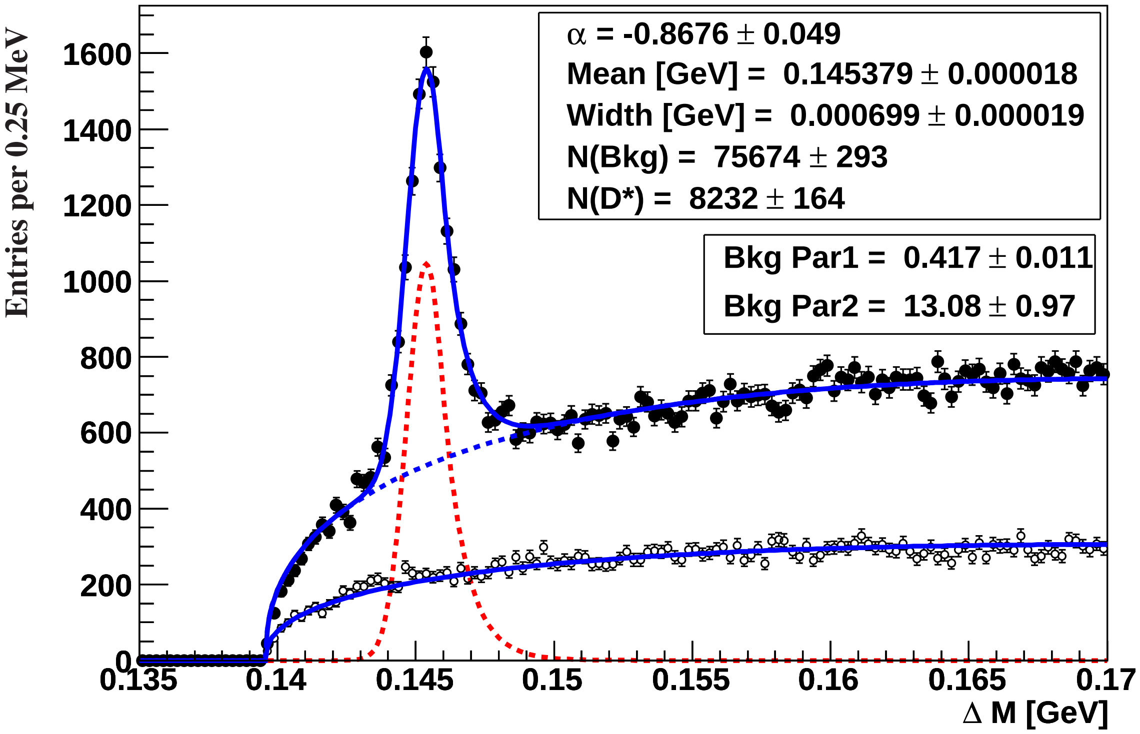

Figure 7.2: *Distribution of ΔM for D^* candidates for RC (filled circles) and WC (open circles). The fit function and parameters of the signal and background are also shown.*

The fit minimization is done with a negative log-likelihood method which is implemented in the $RooFit$ package.
This fitting procedure is applied to every analysis bin. The parameter n is fixed, see [116]. In addition, the parameter α is fixed for the fit of the individual analysis bins to the value determined in a fit to the total data sample to improve the convergence of the fit. The width of the peak is left free because it varies in dependence of the D^* kinematics.
The mass difference $\Delta M = M(K\pi\pi_{slow}) - M(K\pi)$ distribution of the final selected data sample is presented in figure 7.2. A clear peak can be observed around the nominal value of $\Delta M = 145.3\,\mathrm{MeV}$.
A good description is given by the Crystal Ball signal and Granet backgound fit functions and in total 8232 ± 164 D^* mesons have been found.
The systematic error due to the choice of the fit functions used for extraction of the number of D^* mesons is investigated with the usage of different fit functions, see chapter 10.3.
The fitting of the ΔM distribution of the MC used in the analysis proceeds the same way as in data described before [3].

Background reduction

The new detector simulation includes a new simulation and calibration of the specific energy loss dE/dx in the central jet chambers. For data a proper calibration of the specific energy loss was already provided by [1], but the dE/dx information could not be used in analysis case because the detector simulation was not sufficient and not calibrated.
In this analysis the signal to background ratio is improved by applying a particle identification criterion based on the specific energy loss to the kaon candidates. The likelihood of the kaon candidates is shown in figure 7.3. In the analysis the kaon is required to have a likelihood to be

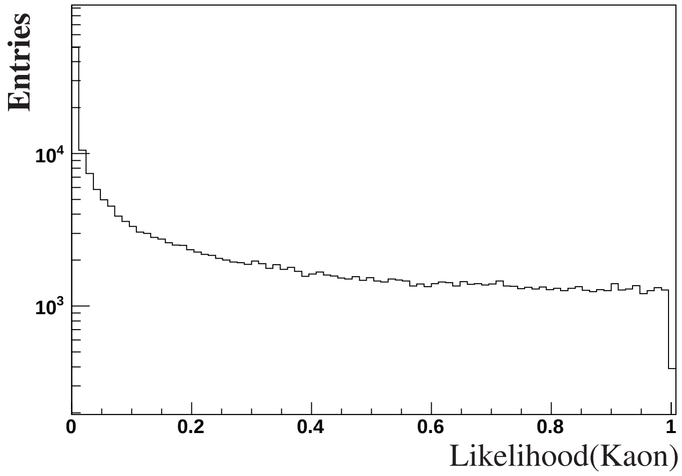

Figure 7.3: *Distribution of the likelihood of kaon candidates.*

---

[3] The same fit procedure is used but the starting value of the background fraction is smaller than in data to take into account that signal MC is used

a kaon of more than 0.02.
In figure 7.4 the reduction of the background is illustrated with the ΔM distribution before and after the cut on the likelihood.

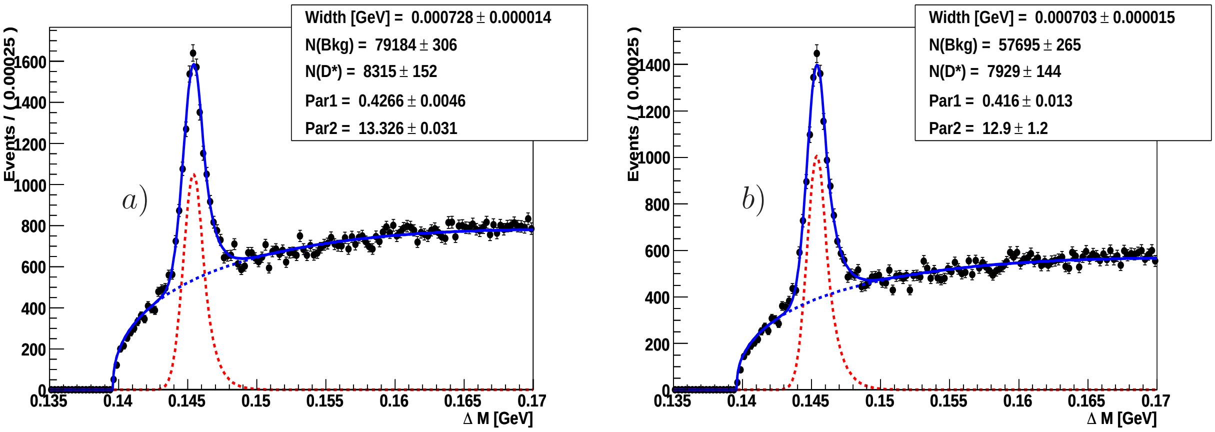

Figure 7.4: *ΔM distribution before a) and after b) the dE/dx cut on the kaon likelihood. Note that in this distribution the inital f cut of $f > 0.13$ was applied.*

The background after the cut is 30% less than before the cut, while the number of D^* mesons in the signal looses 380 D^* candidates (4%) in total. Another advantage is that the simultaneous signal and background fit is stabilized with the cut.
Further background reduction is achieved by an additional cut on the ratio of the transverse momentum of the D^* meson to the sum of the transverse momenta of all particles in the hadronic final state. This ratio is called f and is defined as

$$f = \frac{p_T(D^*\ )}{\Sigma_i^{\theta>10^\circ} E_i sin\theta_i}, \tag{7.4}$$

where E_i represents the energy and θ_i the polar angle of the particle i in the hadronic final state.

The D^* meson which was produced via charm fragmentation carries a large fraction of the charm quark energy because of the hard fragmentation function. For light quark flavors of the combinatorial background the fragmentation function is softer. Thus the quantity f is a suitable cut quantity because it is expected that the D^* meson carries a large fraction of the hadronic final state energy and that the combinatoric background due to light flavors can be suppressed by this cut.
In the previous analysis [120] is was investigated that the best cut value is $f > 0.13$ to reduce the combinatorial background.
But the f cut introduces an inefficiency for signal events, which has to be taken into account in the uncertainty introduced by the model used for the cross section extraction. These MC models have different f distributions and hence the cut in the f distribution can result in an increase of the model uncertainty. Here PYTHIA is used for the analysis and the model uncertainty is

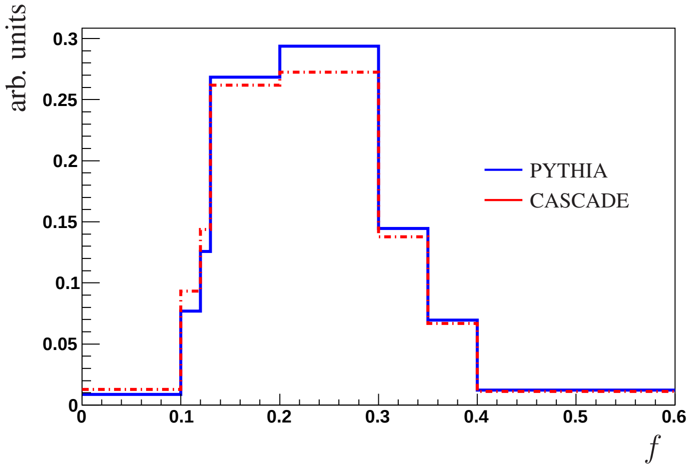

Figure 7.5: *f distribution of PYTHIA (blue line) and CASCADE (red line) signal events.*

determined by the comparison to CASCADE. In figure 7.5 the f distributions for signal events for both MCs are displayed. It can be seen that the f distributions of the two MCs differ above $f > 0.1$. Therefore a cut value below 0.1 is preferable.

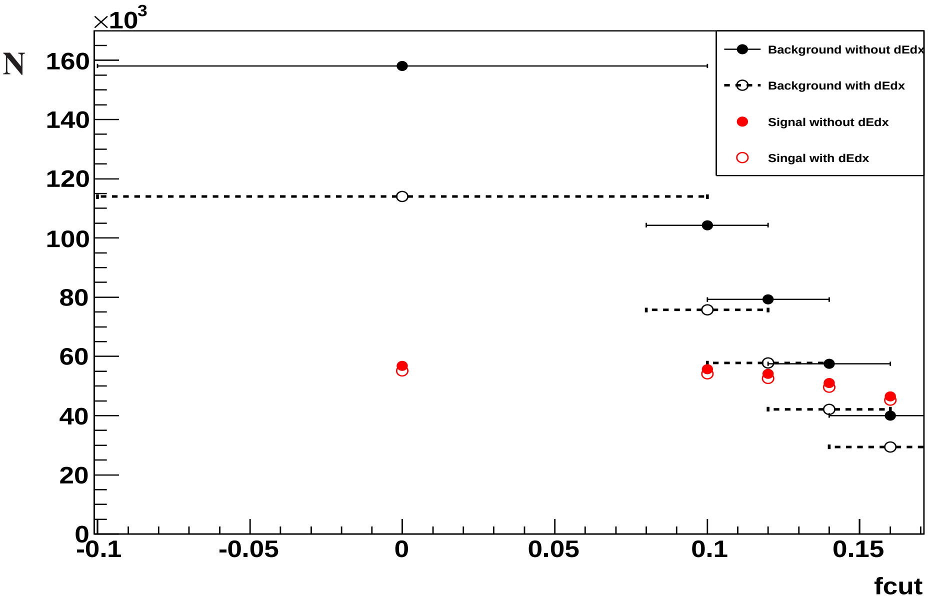

Figure 7.6: *Signal and background behavior due to the cut on the kaon dE/dx-likelihood and the cut value for f, $fcut$. For MC N is $N(D^*)$ and for data $N = N_{Background}$.*

Now with the cut on the specific energy loss described before it is possible to lower the f cut. The lowest possible cut value is investigated in figure 7.6. The signal and background behavior is studied in bins of cut values of the quantity f with and without the cut on the kaon dE/dx-likelihood. The number of D^* mesons in the signal is taken from the signal MC and number of background events is taken from the data background. The number of D^* mesons in the signal shows above $f = 0.1$ a dependence on the f cut which was applied. For the data it can be observed that a similar amount of background reduction can be achieved by applying the likelihood cut together with a cut of $f > 0.1$ as without using the likelihood cut but a cut of $f > 0.13$. Thus within this analysis it is possible to lower the cut value to $f > 0.1$.

In addition to the selection criteria described so far, further selection cuts are applied on the transverse momenta, pseudo–rapidity and invariant masses, see table 7.1.

Selection cuts		
transverse momentum of the D^*	$p_T(D^*)$	$> 1.8\,\mathrm{GeV}$
pseudorapidity of the D^*	$\mid \eta(D^*)\mid$	< 1.5
transverse momentum of the kaon	$p_T(K)$	$> 0.5\,\mathrm{GeV}$
transverse momentum of the pion	$p_T(\pi)$	$> 0.3\,\mathrm{GeV}$
transverse momentum of the slow pion	$p_T(\pi_{slow})$	$> 0.12\,\mathrm{GeV}$
sum of the transverse momenta of kaon and pion	$p_T(K) + p_T(\pi)$	$> 2.2\,\mathrm{GeV}$
pseudorapidity of decay particles	$\mid\eta(K, \pi, \pi_{slow})\mid$	< 1.73
f cut	f	> 0.1
mass window of D^0	$\mid M(K\pi) - M(D^0)\mid$	$< 0.08\,\mathrm{GeV}$
mass difference	ΔM	$< 0.170\,\mathrm{GeV}$
Likelihood of kaon candidates	LH_{Kaon}	> 0.02

Table 7.1: *Definition of the selection cuts on transverse momenta and pseudorapidity of the D^* and the decay particlesand on the invariant masses of the heavy mesons. In addition the cut on the quantity f and the likelihood of the kaon candidates are shown.*

The cut on the transverse momenta of the decay particles of the D^* meson ensures that the track was properly reconstructed. The tracks of the decay particles of the D^* mesons are restricted to the central region with the cut in the pseudorapidity. The D^* meson is required to be in the central region too.
Other cuts on the D^0 mass window, the f cut and the cut on the likelihood of the kaon reduce the combinatorial background.
In addition, a reduction of the background size can be achieved by cutting on the sum of the transverse momenta of the kaon and pion from the D^0 decay. It is expected that the production rate of light quarks rises steeper towards low momenta than the production rate of heavy flavors. This is observable in the background size of the ΔM distribution, which increases towards low momenta and in the forward region of the H1 detector. Because the slow pion has a small transverse momentum, for the region $p_T(D^*) > 1.8\,\mathrm{GeV}$ the transverse momentum of the D^* is carried by the pion and the kaon. In [120] it was found that the cut $p_T(K) + p_T(\pi) > 2.2\,\mathrm{GeV}$ on the sum of the transverse momenta of pion and kaon is a suitable compromise between the reduction of the background size and the signal.

7.4 Trigger Selection

The H1 trigger system provides 128 subtriggers for the selection of the different physics channels. For selecting D^* events in photoproduction three D^* triggers s55, s53 and s122 have been used. The so called high p_T trigger s122 was active during the whole data taking range of this analysis corresponding to the run numbers 477240–500611. The other two triggers have been commissioned after the run number 482535 and 489125 for s53 and s55, respectively. This corresponds to a prescale corrected luminosity of $\mathcal{L}_{s55} = 30.68\,\mathrm{pb}^{-1}$ for s55, $L_{s53} = 68.23\,\mathrm{pb}^{-1}$ for s53 and $\mathcal{L}_{s122} = 93.39\,\mathrm{pb}^{-1}$ for subtrigger s122. The main components of the subtriggers are FTT triggers, but they have additionally CIP trigger conditions. In table 7.2 the trigger conditions are summarized.

All used subtriggers have the same level 1 conditions of FTT and CIP triggers. The CIP trigger elements are used to select D^* events which have a high track multiplicity in the central region of the detector. For example the trigger condition $CIP\_sig > 2$ requires that two times more tracks are in the central than in backward and forward regions together. The other CIP trigger element CIP_mul fires above a certain number of central tracks in the CIP.
The FTT level 1 trigger elements used here select only events which have a certain track multiplicity above a threshold in transverse momentum. All trigger conditions are connected by a logical AND operation.
On the second trigger level the three subtrigger have the $FTT\_zvtx\_hist \geq 2$ and $FTT\_mul\_Te \geq 2$ conditions in common. The trigger condition $FTT\_zvtx\_hist \geq n$ requires that the vertex was determined from tracks and segments with a sufficient good quality [121]. A higher n value corresponds to a better quality of the vertex. In addition it is ensured that only events with at least two tracks above $p_T > 800\mathrm{MeV}$ are selected with $FTT\_mul\_Te \geq 2$. Because of the rise of the data rate of photoproduction events towards lower $p_T(D^*\ )$, the low and medium p_T subtriggers reduce the input rate for level 3 with further conditions on the total transverse energy of all tracks. Also here all trigger conditions are connected by a logical AND operation.
On the third trigger level the selection algorithm for D^* mesons is performed. The subtriggers s53, s55 and s122 use different trigger elements with constraints on the transverse momentum of the D^* meson and the ΔM range which is acceptable.
Even after the trigger selection the rate is too high, such that prescale factors have to be assigned. The high rate includes for example beam–gas background which can have high track multiplicities so that the selection is sensitive to it. The prescale factors depends on the magnitude of the output rate. The low p_T subtrigger s55 had a mean prescale factor of $P(s55) = 2.01$, s53 of $P(s53) = 1.33$ and s122 of $P(s122) = 1.21$.

For the analysis of the data seen by the three subtriggers one has to combine the subtriggers. Two methods are used by the H1 collaboration for the combination of independent subtriggers. A detailed discussion of the combination of triggers in data analysis can be found in [122] and in [2].
The first method assigns priorities to the subtriggers according to their prescale factors with the highest priority for the subtrigger with the lowest prescale factor. Each of the level one subtriggers is implemented as a raw and as an actual bit. The raw trigger bit of the subtrigger is set to 1 if the event fulfills the level 1 condition. For a subtrigger with prescale n the actual bit is set to 1 only for every n^{th} event where the raw bit was set. For the selection of an event it is now checked gradually if the actual bit is set beginning with the highest priority subtrigger. If the actual bit was not set at the first subtrigger the next highest priority subtrigger is regarded until

Trigger conditions			
Trigger level	Subtrigger	trigger element	cut defintion
Level 1	s55,s53,s122	$CIP\_sig > 2$	$\#(cen.tracks) > 2 \cdot (\#(forw. + backw.tracks))$
		$CIP\_mul > 4$	$\#(tracks) > 10$
		$FTT\_mul\_Ta > 5$	$\#(tracks) > 5$ with $p_T > 100\,\mathrm{MeV}$
		$FTT\_mul\_Tc > 2$	$\#(tracks) > 2$ with $p_T > 400\,\mathrm{MeV}$
		$FTT\_mul\_Td > 1$	$\#(tracks) > 1$ with $p_T > 900\,\mathrm{MeV}$
		$FTT\_mul\_Te > 0$	$\#(tracks) > 0$ with $p_T > 1.8\,\mathrm{GeV}$
Level 2	s55	$FTT\_et\_20 > 0$	$E_T > 5.0\,\mathrm{GeV}$
		$FTT\_mul\_Te \geq 2$	$\#(tracks) > 2$ with $p_T > 800\,\mathrm{MeV}$
		$FTT\_zvtx\_hist \geq 2$	vertex quality > 2
	s53	$FTT\_et\_26 > 0$	$E_T > 6.5\,\mathrm{GeV}$
		$FTT\_mul\_Te \geq 2$	$\#(tracks) > 2$ with $p_T > 800\,\mathrm{MeV}$
		$FTT\_zvtx\_hist \geq 2$	vertex quality > 2
	s122	$FTT\_mul\_Te \geq 2$	$\#(tracks) > 2$ with $p_T > 800\,\mathrm{MeV}$
		$FTT\_zvtx\_hist \geq 2$	vertex quality > 2
Level 3	s55	low p_T D^* finder	$p_T(D^*) > 1.5$GeV with $\Delta M \leq 180\,\mathrm{MeV}$
	s53	medium p_T D^* finder	$p_T(D^*) > 2.5$GeV with $\Delta M \leq 180\,\mathrm{MeV}$
	s122	high p_T D^* finder	$p_T(D^*) > 4.5$GeV with $\Delta M \leq 280\,\mathrm{MeV}$

Table 7.2: *Summary of the trigger conditions required by s55, s53 and s122.*

a subtrigger has set the actual bit. The event is then weighted with the prescale factor of the subtrigger where the actual bit was set. If the actual bit was not set at all the event is rejected.
In the second method all subtriggers have the same priority and an averaged weight is applied to the events. For both methods it is required that the subtriggers are statistically independent.
The subtriggers s53, s55, s122 used in this analysis have identical level 1 conditions. Hence they are not independent and none of the two methods can be applied. Therefore a different strategy is used for combining the subtriggers in this analysis.
A combination of the subtriggers is possible if their event samples are separated in different regions of phase space with no overlap regions. This can be reached with a restriction of the transverse momenta of the D^* mesons to a certain range for each subtrigger. Although this restriction to phase space regions leads to the exclusion of events, it is expected that these losses are marginal because of the original high event overlap of the subtriggers.
The selection of appropriate phase space regions for each subtrigger was done with respect to the best possible statistics of the D^* mesons and a good trigger efficiency.

Subtrigger	$p_T(D^*)$ range [GeV]	run range	Luminosity [pb^{-1}]
s55	1.8–2.5	489125–500611	30.68
s53	2.5–4.5	482535–500611	68.23
s122	4.5–12.5	477240–500611	93.39

Table 7.3: *Phase space regions, active run ranges and prescale corrected luminosity for s55,s53 and s122.*

It was found in [120] that the following phase space regions are an appropriate choice: The subtrigger s55 is used in the low transverse momentum range and is restricted to the range of $1.8 < p_T(D^*) < 2.5\,\mathrm{GeV}$.
The lower border of the transverse momentum range of s55 is defined by the s55 p_T threshold and the signal to background ratio. The upper border is set by the transverse momentum threshold of s53. In principle it would be possible to extend the transverse momentum range of s55 because the subtrigger has no intrinsic upper cut on p_T.
But the prescale corrected luminosity of s55 is a factor two lower than the luminosity of s53, because s53 was commissioned earlier and thus has seen a larger run range. Thus higher statistics is reached by choosing s53 at the lowest possible transverse momentum.
The $p_T(D^*)$ range of the medium transverse momentum subtrigger s53 is selected to be $2.5 < p_T(D^*) < 4.5\,\mathrm{GeV}$. The upper border is defined with respect to the transverse momentum threshold of subtrigger s122. In the same manner as for s55 it would be possible to extend the p_T range, but s122 was active over the full analysis run range and has a higher prescale corrected luminosity than the medium p_T subtrigger.
The transverse momentum range, the prescaled corrected luminosity and the active run range for the three used subtriggers are summarized in table 7.3. More details of the individual trigger elements can be found in [95, 123, 124].

7.5 Data Stability

A good estimate for the stability of the data selection is the flatness of the production yield for each subtrigger which was used in the analysis. The production rate $N(D^*)/\mathcal{L}$ in bins of integrated luminosity is studied separately for each subtrigger for the selected data sample. The number of D^* mesons is extracted by fitting simultaneously the Crystal Ball signal and Granet background functions as described in section 7.3. For this purpose the luminosity intervals have to be defined such that the signal in each bin is sufficiently large.
The low and medium p_T subtriggers are studied in intervals of $6\,\mathrm{pb}^{-1}$ and the high p_T subtrigger in intervals of $8\,\mathrm{pb}^{-1}$.

The production rates as a function of the run number are displayed in figures 7.7. The different run intervals correspond to intervals of equal integrated luminosity. The distributions start at different run numbers which is due to the different commissioning times for the subtriggers. As expected the low p_T subtrigger s55 has the highest production rate because of the rise of the photoproduction cross section towards lower transverse momenta.
The distributions are flat within statistical fluctuations for all subtriggers.

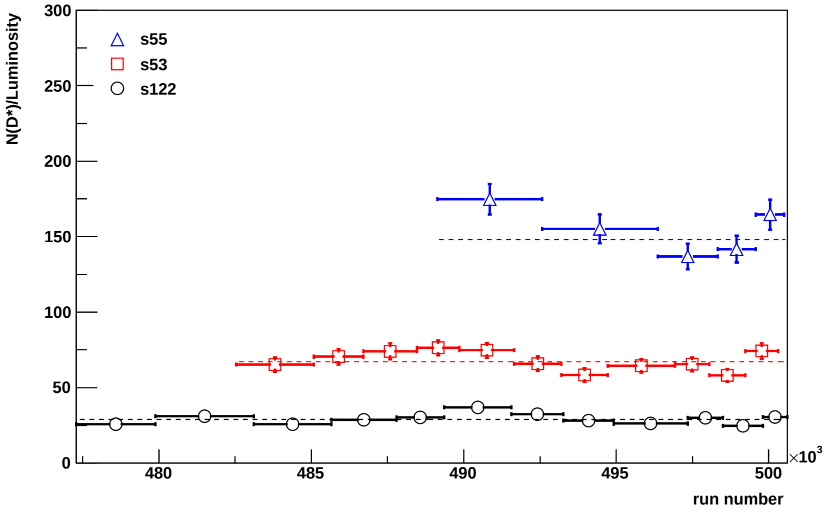

Figure 7.7: *Production yield of D^* mesons as function of constant luminosity for the subtriggers $s55$, $s53$ and $s122$. All selection cuts are applied. The signal is fitted.*

Chapter 8

Control Distributions

Two MC generators are used in this analysis to generate events. The resulting PYTHIA and CASCADE events are passed through the complete H1 detector simulation. Hence the goodness of the data description by the simulated detector response can be studied with control distributions. The final H1 detector simulation and final reconstruction version, DST7, is used for comparison with the data.
A good agreement between data and simulation is required because the measured data cross section is corrected for detector effects with PYTHIA MC and the best possible agreement between data and PYTHIA control distributions must be reached. The cross section is corrected with the bin by bin correction method, see section 10.2, which demands a good discription of the data by the MC simulation.
Discrepances can occur because either the MC distribution can be generated not appropriately or the detector response may be simulated wrongly. If the generated events disagree with the measured distribution, the MC has to be adjusted to give a good data description, or the not sufficient described phase space regions have to be excluded.
In this chapter control distributions for z_{vertex}, $p_T(D^*)$, $\eta(D^*)$, $z(D^*)$, and $W_{\gamma p}$ are studied. The control distributions of $p_T(D^*)$, $\eta(D^*)$, $z(D^*)$ reveal that a correction of the MC is needed. For this a reweighting of the MC in $p_T(D^*)$, $\eta(D^*)$, $z(D^*)$ one after another was performed. The trigger efficiency was studied and corrected before.

CASCADE was not used for the data correction but to study the model dependence of the measurement. The reweighting was done in the same variables as for PYTHIA but the reweighting functions have been determined separately.
In each analysis bin in data and MC a simultaneous Crystal Ball signal Granet background fit was performed to extract the number of D^* mesons.

Distribution of the event vertex

A distribution which benefits from the new detector simulation is the distribution of the z position of the event vertex z_{vertex}. It is well described by the latest run dependend vertex simulation and no reweighting is needed as in earlier analyses, see figure 8.1. PYTHIA and the data points are both fitted with Gaussian functions. Both fits are well in agreement and the resulting fit parameters of the data are displayed. The position is close to zero ($0.17\mathrm{cm}$) and the width amounts to $9.07 \pm 0.01\mathrm{cm}$.

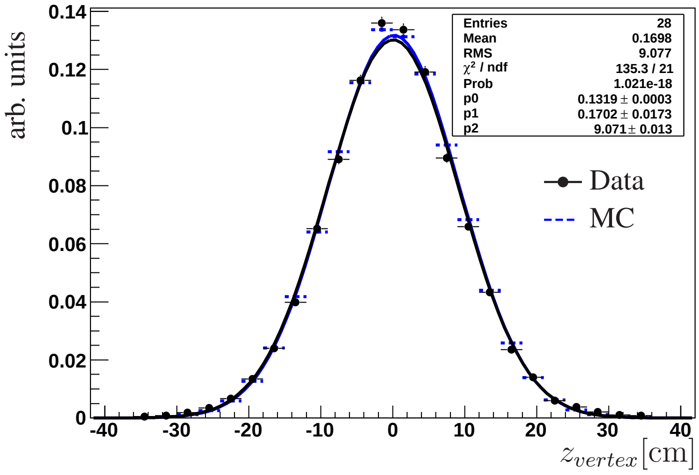

Figure 8.1: z_{vertex} *control distribution for data (black circles) and PYTHIA MC (short blue dotted line) together with the gaussian fit functions for data (full black line) and for MC (full blue line). Since both fit functions are nearly the same only the data fit result parameters are displayed.*

Control distributions of D^* meson and decay particle quantities

In other variables some disagreement between data and the MC distributions have been found. In figure 8.2 a), c) and e) the data, PYTHIA and CASCADE MC distributions for $p_T(D^*)$, $\eta(D^*)$ and $z(D^*)$ are shown and disagreement between data and both MC predictions is visible.

The inelasticity $z(D^*)$ is defined according to [4] by $z(D^*) = P \cdot p(D^*)/(P \cdot q)$ with P, $p(D^*)$ and q being the four–momentum of the incoming proton, the D^* meson and the exchanged photon. With this quantity it is possible to measure the fraction of the photon energy transferred to the D^* meson in the proton rest frame and it is expected that it is sensitive to the production mechanism and to the $c \rightarrow D^*$ fragmentation function [4]. The inelasticity can be reconstructed as $z(D^*) = (E - p_z)_{D^*}/(2yE_e)$.
Since the trigger efficiency is corrected and the reconstruction efficiency is understood, see section 10.2, disagreement is attributed to the generated distributions. Therefore a reweighting

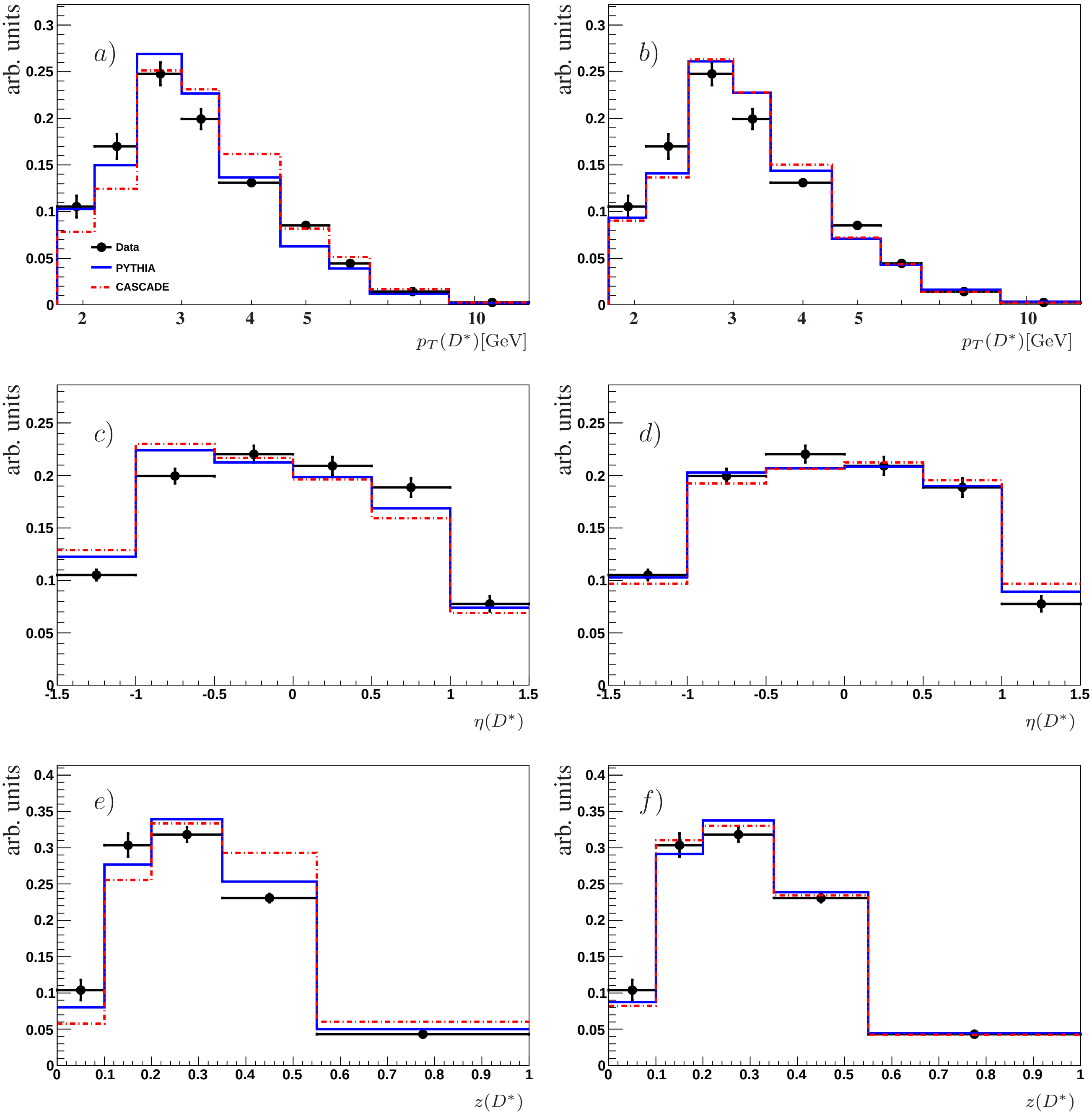

Figure 8.2: *Control distributions for data, PYTHIA MC (blue line) and CASCADE MC (red line) in variables of the* D^* *meson* $p_T(D^*)$*,* $\eta(D^*)$ *and* $z(D^*)$*. In the left column the distributions before and in the right column after the reweighting in all variables are shown.*

can be applied to improve the agreement. To determine the function and parameters for the reweighting of the MC distribution the ratio of Data to MC is studied in figure 8.3 for PYTHIA and CASCADE separately. The reweighting is done successively. First the $p_T(D^*)$ ratio of data and MC is fitted and the reweighting function is determined, see figure 8.3 a) and b). Then this weight is applied to the MC and the control distributions are studied again. In a second step the $\eta(D^*)$ reweighting is performed and at last the $z(D^*)$ reweighting was done. The ratios and fit functions for the $\eta(D^*)$ and $z(D^*)$ reweighting are illustrated in figure 8.3 c) to f).

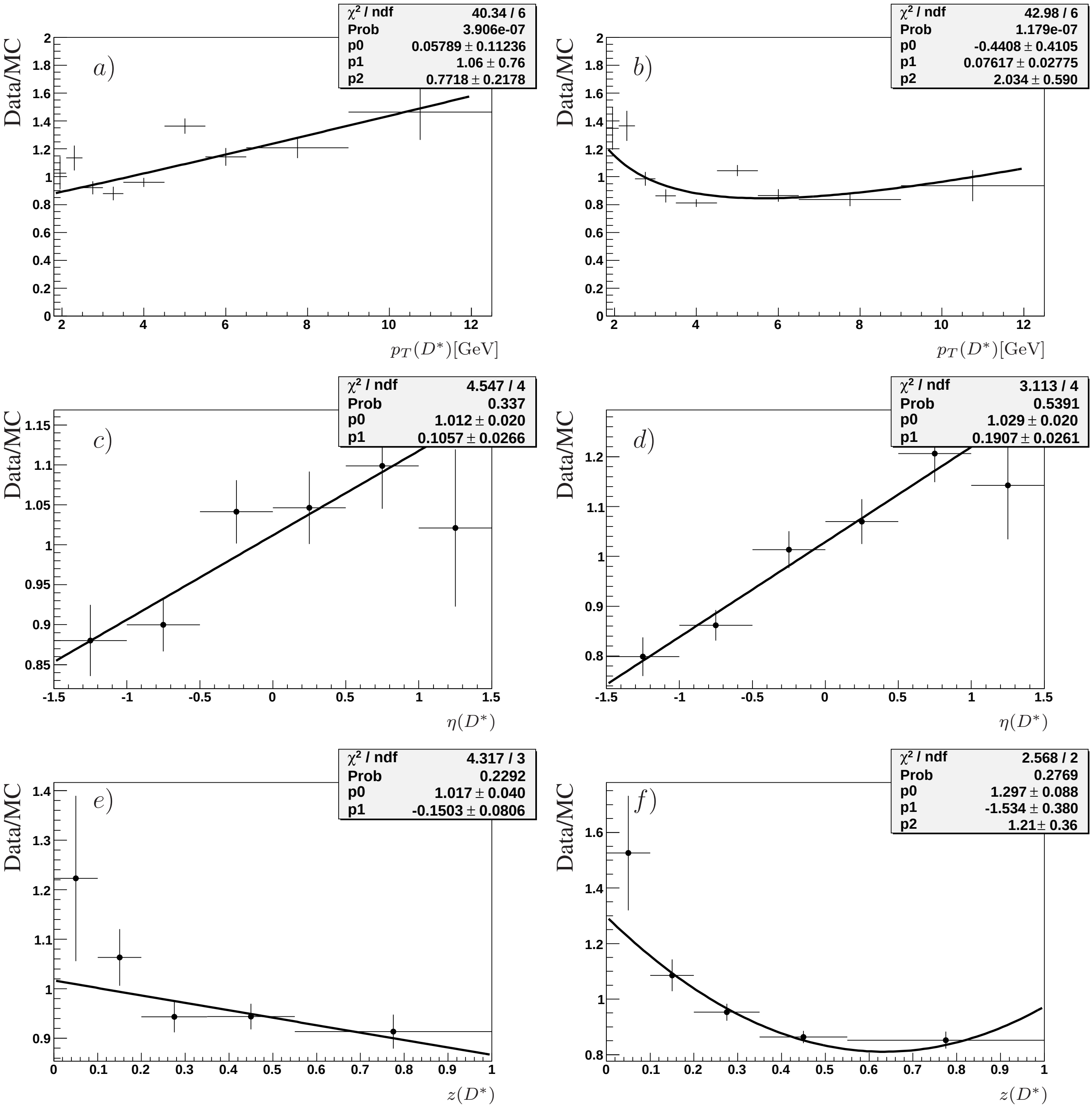

Figure 8.3: *Ratio of data and MC in variables of $p_T(D^*)$, $\eta(D^*)$ and $z(D^*)$ for PYTHIA left column and for CASCADE in the right column. In addition the fit function is shown.*

The distribution of the D^* variables $p_T(D^*)$, $\eta(D^*)$ and $z(D^*)$ after the reweighting procedure can be seen in the right column of figure 8.2. A good agreement is observed between data and the generated distributions.

The control distribution of the center of mass energy of the photon proton system before the reweighting in the other variables is depicted in figure 8.4 a). For this quantity no reweighting was applied. Moreover it is tested that the reweighting in the other variables does not spoil the $W_{\gamma p}$ control distribution. The $W_{\gamma p}$ control plot after the reweighting procedure is presented in figure 8.4 b).

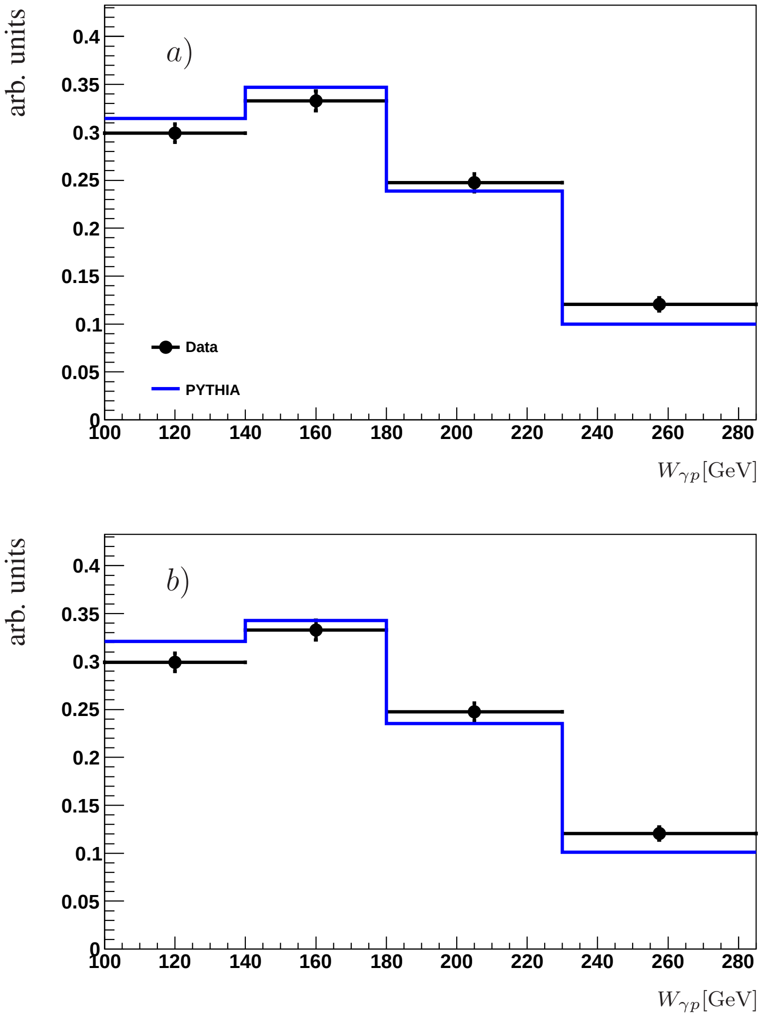

Figure 8.4: *Control distribution for the center of mass energy of the photon proton system for data and PYTHIA before the reweighting procedure in a) and after it in b).*

In addition the polar angle and the transverse momentum of the tracks of the decay particles of the D^* meson decay have been studied. The distribution of the transverse momentum of the kaon and pions are used to test the implementation of the central jet chambers and the

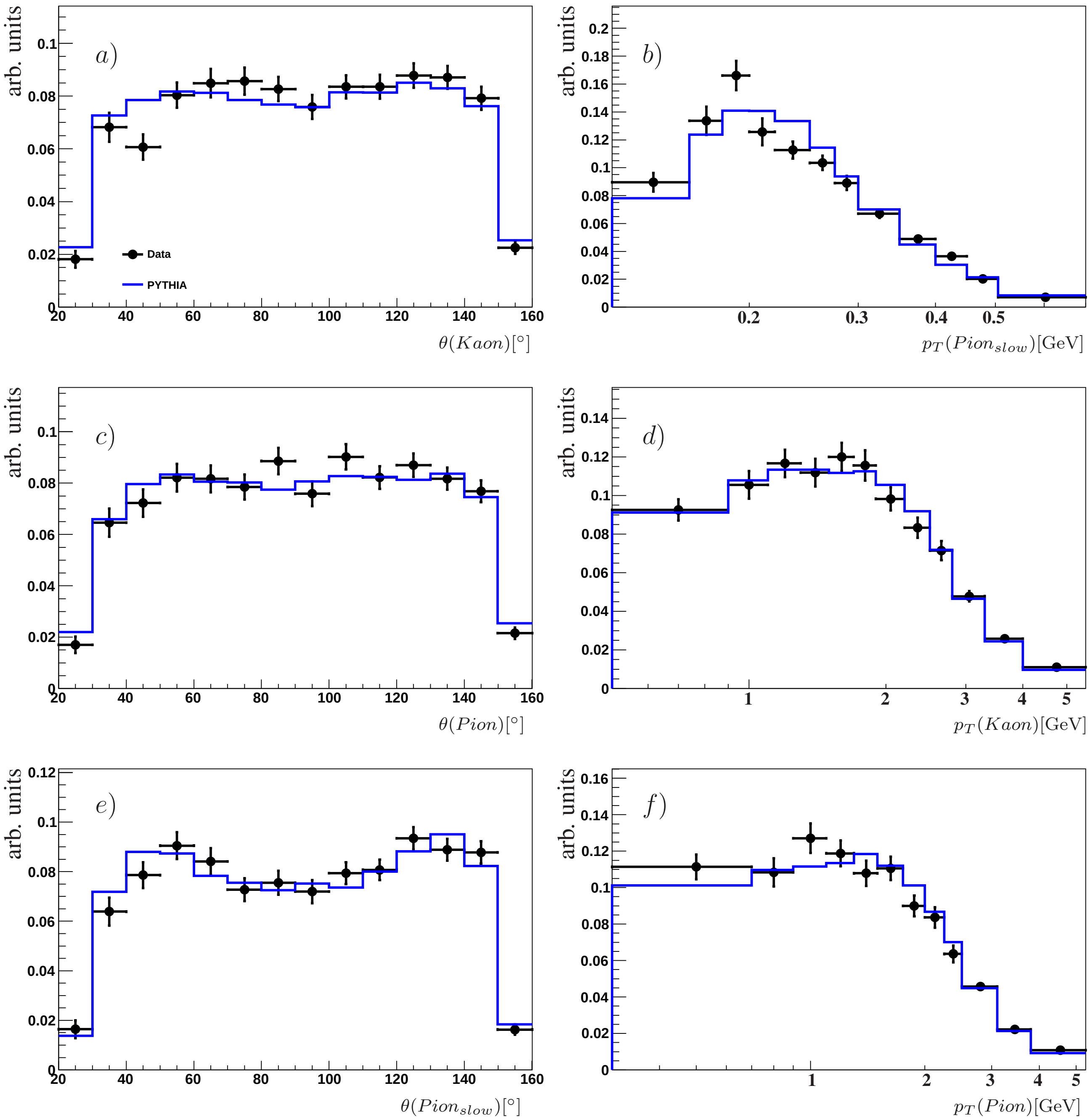

Figure 8.5: *Control distributions for the polar angle and the p_T of the tracks for the decay particles for data and PYTHIA after the reweighting.*

dead material. With the polar angle it is possible to localize inefficiencies. Again the number of D^* mesons in each bin is extracted by fitting the signal and background simultaneously. The control distributions for data and PYTHIA after the reweighting in $p_T(D^*)$, $\eta(D^*)$ and $z(D^*)$ are illustrated in figure 8.5 and show a reasonable good agreement.

Chapter 9

Trigger Efficiency

The measured number of D^* mesons includes detector effects like acceptance, efficiencies and resolutions for which one has to correct the data. One of this detector corrections needed is due to the efficiency of triggers which have been used in the analysis.
The distribution of the amount of events per run in MC is the same as in data. It is possible to perform the same run selection as for the data sample. The prescaling of the subtriggers in MC is done by down weighting the events with mean prescales corresponding to the p_T region. The trigger efficiency is taken fully from the photoproduction MC by requiring that the reconstructed MC events have been excepted by the subtriggers s55, s53 and s122. For this strategy a good agreement between the data trigger efficiency and the simulated trigger efficiency is demanded.

In photoproduction it is only possible to trigger on the hadronic final state, since the electron is scattered in the beam pipe. Typically D^* events have a too low energy deposite in the calorimeter to be used for triggering. Therefore all triggers for D^* events in photoproduction have FTT conditions.

For the determination of the trigger efficiency independent monitor triggers are required which do not contain FTT trigger elements. In DIS independent monitor triggers are available due to the scattered electron which is detected with the SpaCal. Therefore the trigger efficiency is determined using deep inelastic scattering events with a virtuality of $Q^2 > 5\,\mathrm{GeV}^2$. Here the monitor triggers s0 and s3 have been used. The MC trigger efficiency which was simulated with FTTemu is compared to the data trigger efficiency and corrected to reach a good description of the data. In the analysis the photoproduction MC trigger efficiency is used which was simulated with the corrected simulation.

The available amount of statistics of events which have been triggered with s55 and s53 is low, because of the late commissioning time. However, already before s55 and s53 were commissioned the information needed to determine the FTT trigger elements have been stored in data. Since run number 477240, which is the begin of the s122 subtrigger run range, the information is available. Therefore it is possible to increase the statistics for the determination of the trigger efficiency by extending the active run range of the subtriggers s55 and s53 to begin at run number 477240. Tracks from the FTT were used and the trigger elements of s53 and s55 were rebuilt. The rebuilding was tested with events where s55 and s53 were active. The trigger decision was found to be identical.

First it was studied in data if the trigger efficiency is the same for real D^* mesons as on the combinatorial background, which was assumed in [120]. In figure 9.1 the trigger efficiency dependence on $\eta(D^*)$ is displayed for the whole ΔM region and for the signal region. In data the trigger efficiency in the whole ΔM histogram is different from the trigger efficiency in the signal region only. This is due to the combinatorial background. Since for the data correction only the trigger efficiency of the signal is relevant, fits are used to determine the number of D^* mesons. To make the fits in data and MC similar, inclusive charm RAPGAP MC is used.

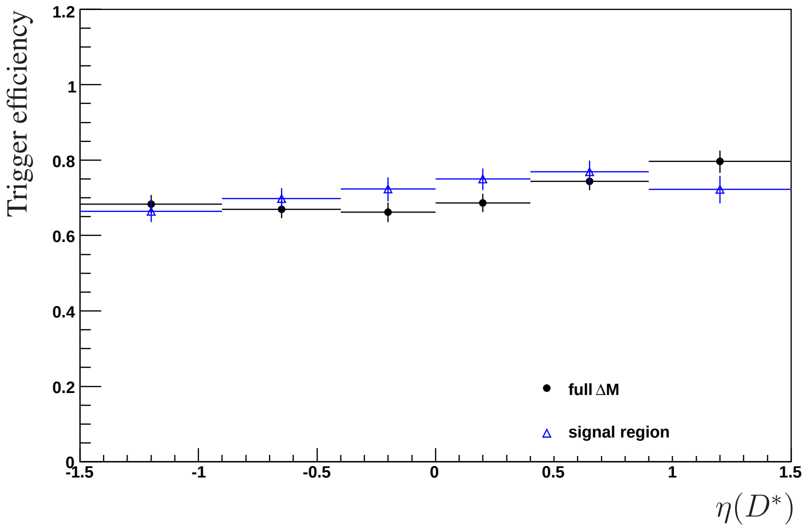

Figure 9.1: *Trigger efficiency for data for the whole ΔM region (full circles) and only the signal region (open triangles).*

To study the dependence of the trigger efficiency on $p_T(D^*)$, $\eta(D^*)$, $W_{\gamma p}$ and $z(D^*)$, in each bin the ΔM histogram of MC and data is fitted with a simultaneous Crystal Ball signal and Granet background fit. Further the ΔM distributions of the rejected and accepted events of the trigger are fitted simultaneously with only one additional fit parameter ϵ which is the trigger efficiency. All other fit parameters like the D^* peak position and width are forced to agree between the accepted and rejected sample. It is required that the number of accepted events, $N_{accepted}$, fulfills the condition $N_{accepted} = N_{total} \cdot \epsilon$ and that the number of rejected events satisfies $N_{rejected} = N_{total} \cdot (1 - \epsilon)$ with $N_{total} = N_{rejected} + N_{accepted}$. Because of the decrease of statistics with each of the trigger levels of the accepted histogram it is a major advantage to fit the histograms of the accepted and rejected events simultaneously. Thus always the full statistics is used to determine the shape of the fit functions.

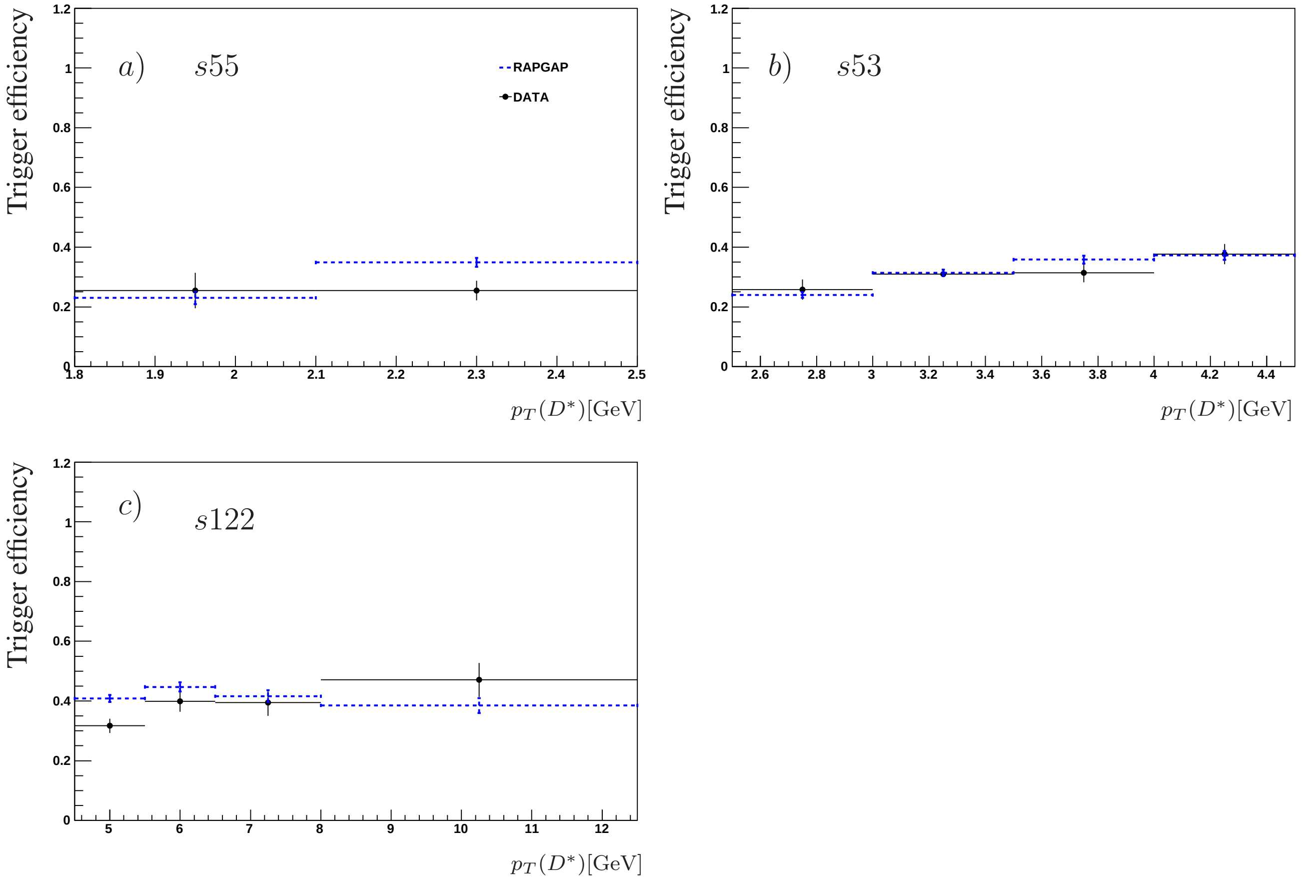

Figure 9.2: *Trigger efficiency dependence for subtriggers s55, s53 and s122 on the transverse momentum of the D^* meson. The error bars show the statistical uncertainty of the fit result.*

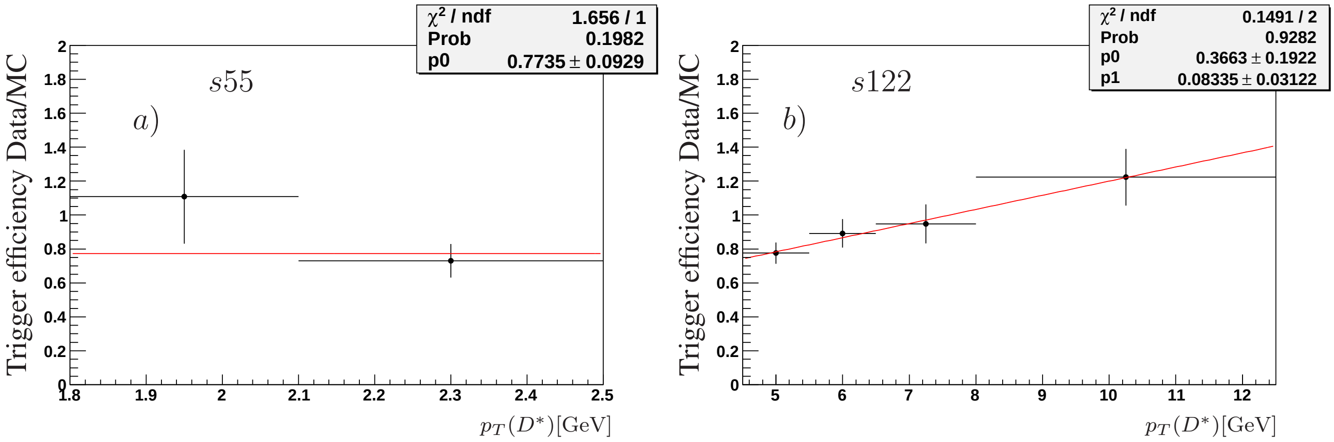

Figure 9.3: *The ratio of data to MC trigger efficiency together with the fit result are displayed.*

The dependence of the trigger efficiency separately for the subtriggers s55, s53 and s122 on the transverse momentum of the D^* meson is shown in figure 9.2.

The MC trigger efficiency of the medium p_T trigger s53 is in good agreement with the data. But the trigger efficiency of the low p_T and the high p_T trigger of data and the simulation show some discrepancies.
In order to correct the simulation the ratio of the data trigger efficiency to the MC trigger efficiency is calculated for each bin and fitted. The ratio for s55 is fitted with a constant and the ratio for s122 with a polynomial of first order. The data to MC ratio together with the fit result can be regarded in figure 9.3. Then the trigger efficiency in MC events is reweighted with respect to the D^* transverse momentum and the corresponding subtrigger phase space.

The resulting trigger efficiency for data and the reweighted MC as a function of $p_T(D^*)$, $\eta(D^*)$, $W_{\gamma p}$ and $z(D^*)$ are displayed in figures 9.4 and 9.5.
The efficiency is around $40 - 30\%$ in all D^* variables and is not flat in the pseudorapidity of the D^* as assumed in [120] but has a $\eta(D^*)$ dependence.
After the reweighting procedure a reasonable agreement is observed. Thus the trigger efficiency can be taken from simulation of the photoproduction MC, in which the same correction as a function of $p_T(D^*)$ is applied.

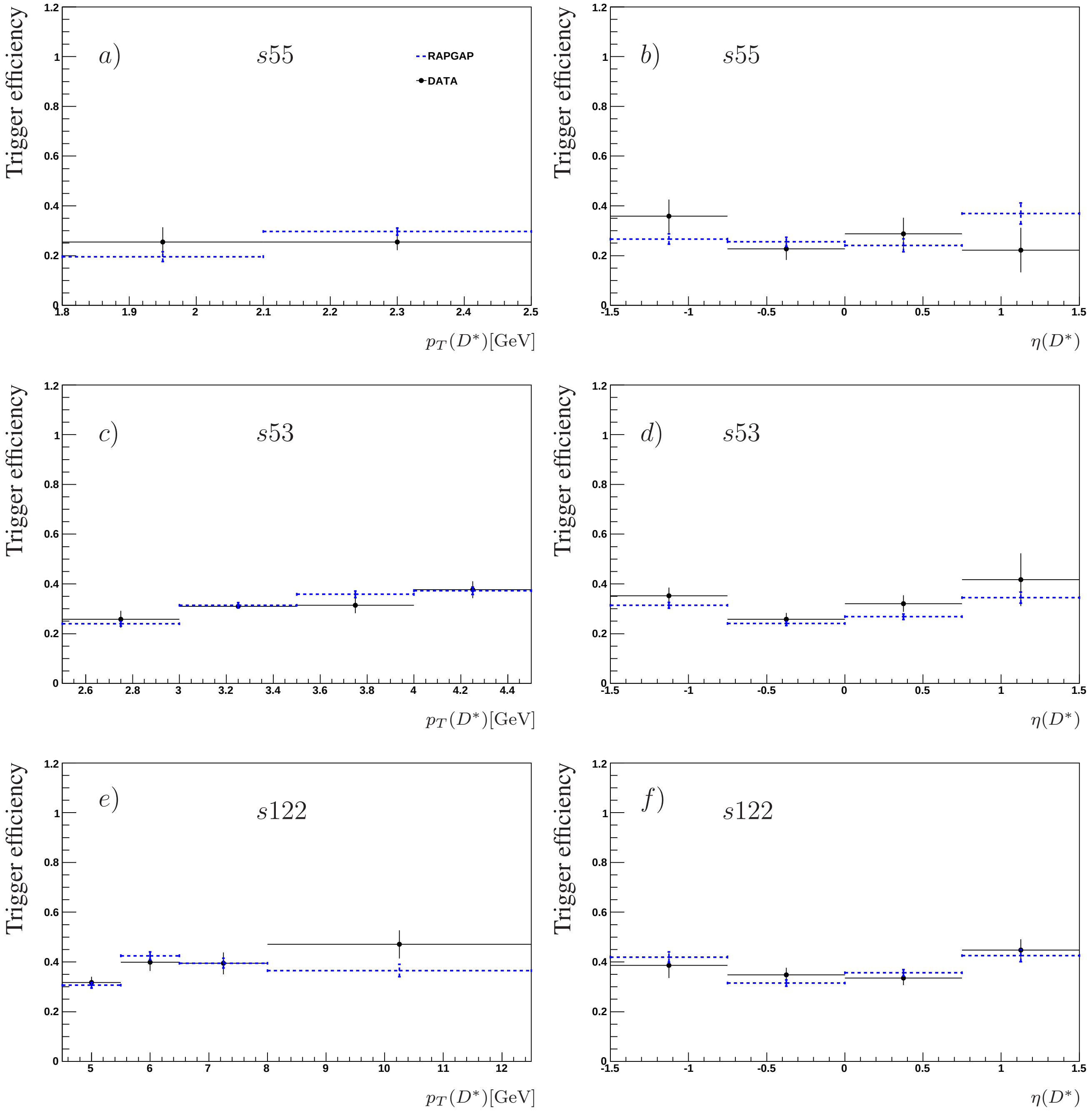

Figure 9.4: *Trigger efficiency for subtriggers s55, s53 and s122 for data and reweighted MC in dependence of $p_T(D^*)$ and $\eta(D^*)$. The error bars show the statistical uncertainty of the fit result.*

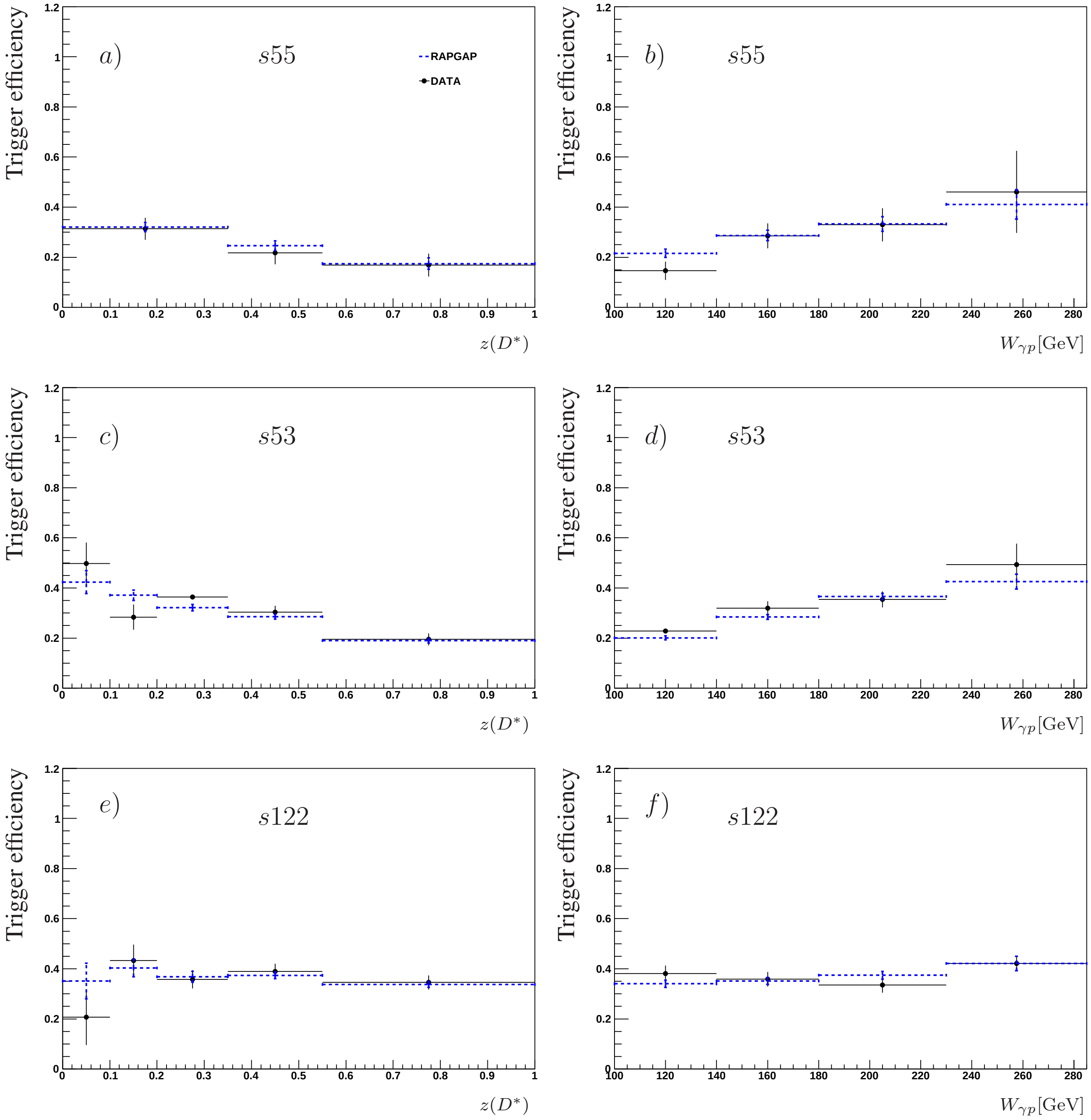

Figure 9.5: *Trigger efficiency for subtriggers s55, s53 ans s122 for data and reweighted MC in dependence of* $z(D^*)$ *and* $W_{\gamma p}$*. The error bars show the statistical uncertainty of the fit result.*

Chapter 10

Cross Section Determination and Systematic Errors

In general the cross section σ is defined as the number of events N per luminosity $\mathcal{L}$ to $\sigma = \frac{N}{\mathcal{L}}$. But the measured number of events is too low because of detector inefficiencies. Thus the number of events has to be corrected with a factor ϵ which includes all the detector effects. In addition the uncertainty of the measurement has to be taken into account. The uncertainties are divided into statistical and systematic uncertainties. In the next chapter the sources of uncertainties will be studied in detail.

10.1 Calculation of the Cross Section

In this analysis the cross section for D^* mesons in the golden decay channel
$D^{*\,\pm} \rightarrow D^0\pi^\pm \rightarrow K^\pm\pi^\mp\pi^\pm_{slow}$ will be measured. The extraction of the number of D^* mesons $N(D^*)$ is described in section 7.3. The correction factor ϵ includes corrections for acceptance, reconstruction efficiency and trigger efficiency and can be separated to $\epsilon = A \cdot \epsilon_{rec} \cdot \epsilon_{trig}$ where A represents the acceptance, ϵ_{rec} the reconstruction efficiency and ϵ_{trig} the trigger efficiency. The acceptance and reconstruction efficiency will be studied in the next sections.
The cross section in the visible range for the D* meson production is calculated with the following formula

$$\sigma_{vis}(ep \rightarrow eD^*\,X) = \frac{N(D^*)(1-r)}{\mathcal{L} \cdot \mathcal{BR}(D^* \rightarrow K\pi\pi_{slow}) \cdot \epsilon} \tag{10.1}$$

where $\mathcal{BR}(D^* \rightarrow \pi\pi_{slow})$ is the branching ratio of the analysed decay chain.

The number of D^* mesons must be further corrected for reflections from other D^0 decays with the correction factor $(1-r)$. The contribution of D^* mesons from b–quark decays is expected to be small and is included in the cross section.

The visible region, in which the D^* cross section is measured, is restricted to $p_T > 1.8\,\text{GeV}$ and $|\eta| < 1.5$. A summary of the visible kinematic range of the measurement is presented in

Visible kinematic range	
$p_T(D^*)$	$> 1.8\,\mathrm{GeV}$
$\|\eta(D^*)\|$	< 1.5
Q^2	$< 2\,\mathrm{GeV}^2$
$W_{\gamma p}$	$(100 - 285)\,\mathrm{GeV}$

Table 10.1: *Definition of the visible kinematic range*

table 10.1. The transverse momentum of the D^* mesons is required to be greater $1.8\,\mathrm{GeV}$ due to the trigger selection and a sufficient ratio of signal to background, which gets worse towards lower transverse momenta. In addition the D^* meson has to be in the pseudorapidity range of $|\eta(D^*)| < 1.5$ to ensure that it is in the central region and that the tracks of the decay particles are in the acceptance of the CJC and the FTT. To select photoproduction events by requiring a veto for the scattered electron in the SpaCal the Q^2 range is restricted to be lower than $2\,\mathrm{GeV}^2$. The limited range of the center of mass energy of the photon-proton system suppresses DIS background and excludes events from the very forward region of the detector in order to guarantee good event reconstruction.

The differential cross section for the measured quantity Y is calculated as

$$\frac{d\sigma_{vis}(ep \to eD^*\,X)}{dY} = \frac{N(D^*)(1-r)}{\Delta Y \cdot \mathcal{L} \cdot \mathcal{BR}(D^* \to K\pi\pi_{slow}) \cdot \epsilon} \tag{10.2}$$

but here the number of D^* mesons $N(D^*)$ and the efficiency ϵ are determined in the interval ΔY.

10.2 Detector Effects

In the present analysis it is assumed that the migration between bins are so small that the bin-by-bin method can be used. As described in the last section correction factors are needed to correct the extracted number of D^* mesons for detector effects. In the bin-by-bin method these correction factors are applied bin wise. The corrections are determined with MC simulation, here PYTHIA is used. The initially generated events are compared to the events which have passed through the simulated detector response and correction factors for the acceptance and the reconstruction efficiency are determined. The migrations between the bins are quantified by the quantity called purity. In the following paragraph the purity, acceptance and reconstruction efficiency are studied.

Purity

First it must be checked if it is feasible to apply bin wise corrections to the cross section measurement. This is the case if the migrations between the bins are small. In the H1 collaboration two definitions of the purity are common [125]. The first definition of the purity includes migration from outside into the visible range: Here the purity P is defined as the ratio of the number of events, $N^{vis}_{gen\&rec}$, which have been generated and reconstructed in the same bin in the visible range to the number of reconstructed events in this certain bin, N_{rec},

$$P = \left.\frac{N^{vis}_{gen\&rec}}{N_{rec}}\right|_{bin}. \tag{10.3}$$

The migration from outside into the visible range are taken into account by not requiring any of the visibility range conditions for N_{rec}. For using the bin–by–bin method only small migrations are allowed. and a purity above $\sim 70\%$ is demanded commonly in the H1 collaboration. Below this value too many migrations occur and the uncertainties would be significantly underestimated by the bin–by–bin method. Then other methods like unfolding have to be adopted.

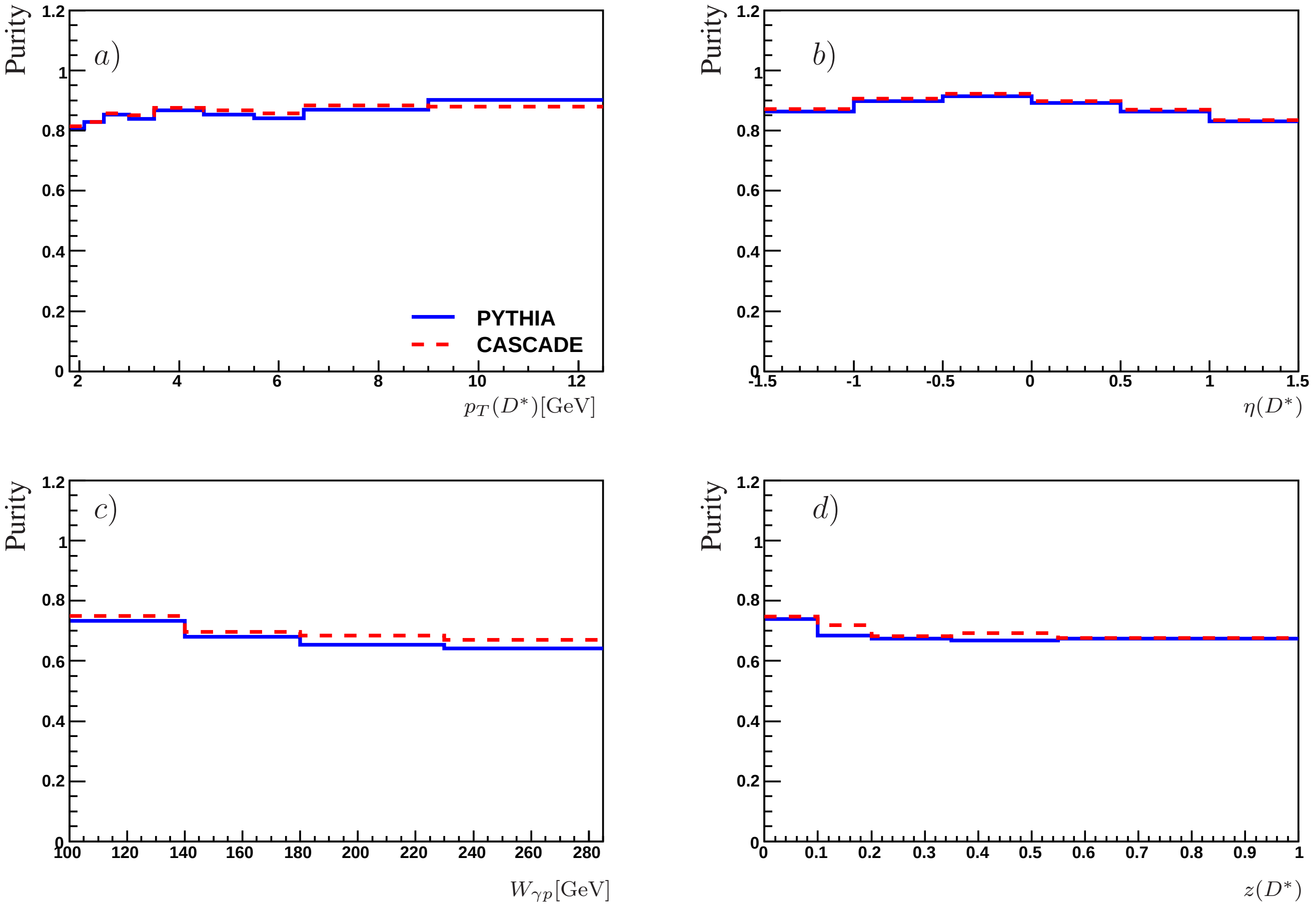

Figure 10.1: *Purity as a function of $p_T(D^*)$, $\eta(D^*)$, $W_{\gamma p}$ and $z(D^*)$ for the leading order MC PYTHIA (blue line) and CASCADE (red line).*

The migrations are studied for the PYTHIA and CASCADE MC simulations in all the quantities in which the cross section measurement is performed. The purity as a function of the transverse momentum, the pseudorapidity and the inelasticity of the D^* meson and the γp

centre–of–mass energy $W_{\gamma p}$ are presented in figure 10.1. In $p_T(D^*)$, figure 10.1 a), and $\eta(D^*)$, figure 10.1 b), the averaged purity lies above 80%. For $W_{\gamma p}$ and $z(D^*)$ the purity is around 10% lower , between 75% and 70%. A very similar behavior for PYTHIA and CASCADE distributions can be observed.

The second way to define the purity includes only migrations between the bins inside the visible range [125] and can be used to study if the binning was properly chosen: In this case the purity P' is the ratio of the number of events which have been generated and reconstructed in the same bin in the visible range to the number of reconstructed events in this certain bin in the visible range, N_{rec}^{vis}:

$$P' = \left.\frac{N_{gen\&rec}^{vis}}{N_{rec}^{vis}}\right|_{bin} . \tag{10.4}$$

The purity P' as a function of $p_T(D^*)$, $\eta(D^*)$, $W_{\gamma p}$ and $z(D^*)$ is shown in figure 10.2. In $p_T(D^*)$ and $\eta(D^*)$ almost no migrations between the bins are observed. In these variables the purity P is lower as the purity P'. This can be explained with the phase space cut in $W_{\gamma p}$. The $W_{\gamma p}$ bins from $140-240\text{GeV}$ show nearly no changes in comparison to the purity P, because

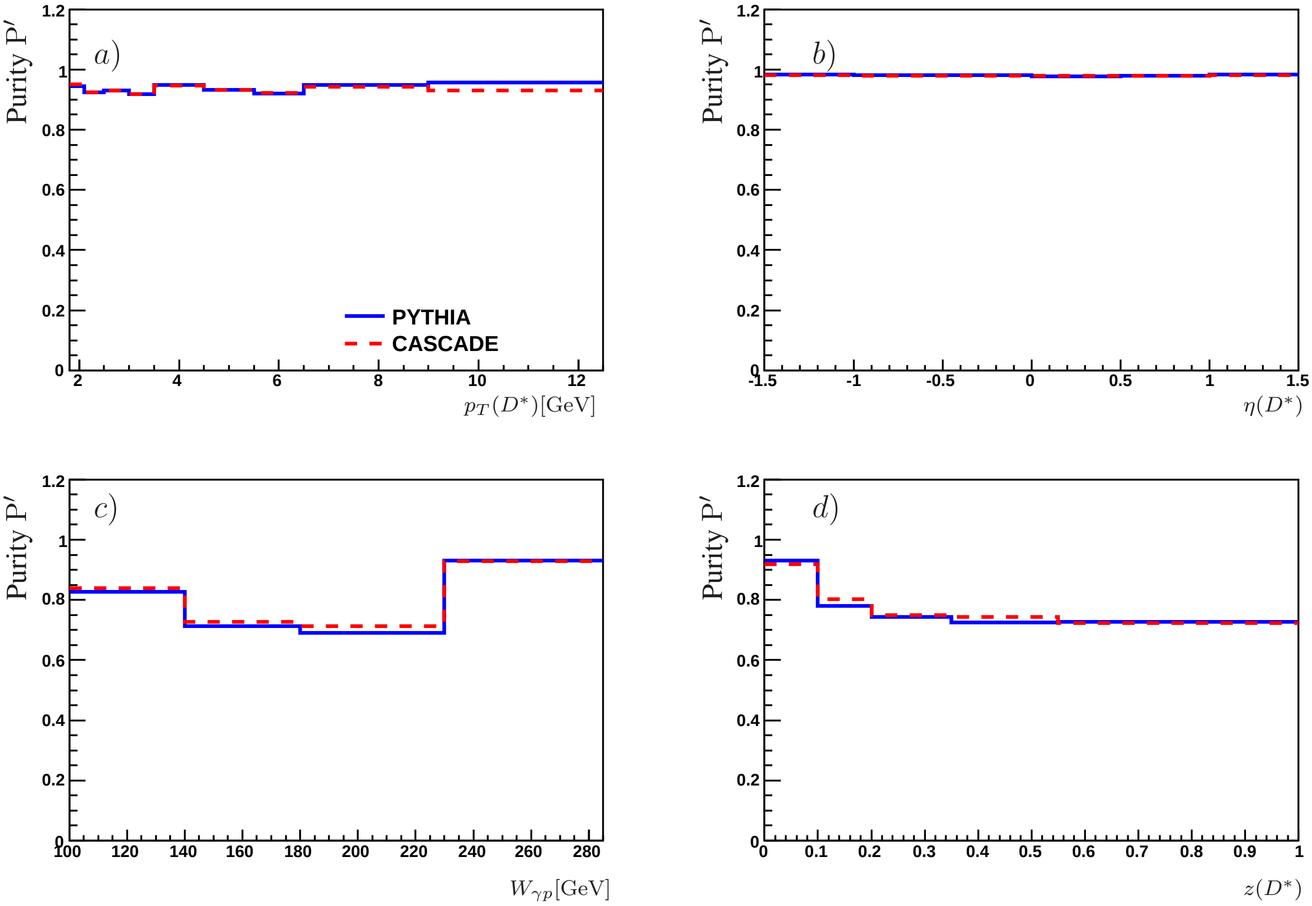

Figure 10.2: *Purity P' as a function of $p_T(D^*)$, $\eta(D^*)$, $W_{\gamma p}$ and $z(D^*)$ for the leading order MC PYTHIA (blue line) and CASCADE (red line).*

of the bad resolution. In contrast the purity in the border bins is now much higher. The purity P' is calculated after the phase space cuts and so no migration inside the phase space are possible which leads to a higher purity in the border bins. $z(D^*)$ has again a bad resolution and the higher purity can be explained similar to the rise of the purity P' in comparison to the purity P in $W_{\gamma p}$.

Acceptance

The ratio of the number N_{gen}^{acc} of generated D^* events in the visible range which have passed the acceptance cuts to the initial number N_{gen} of generated D^* mesons in the visible range is an estimate for the fraction of event losses due to the detector geometry. $p_T(D^*)$ and $\eta(D^*)$ are reconstructed from D^* decay particles only, while for $W_{\gamma p}$ and $z(D^*)$ all particles of the hadronic final state have to be reconstructed, and losses out of the detector play a larger role. It is expected that differences between models (e.g. used in PYTHIA and CASCADE MC simulations) have an influence on the acceptance, while for events within the acceptance range the reconstruction efficiency should be very similar for all models. But the reconstruction efficiency, which is studied in the next section of this thesis, reveals differences between the models, although only events in the acceptance range have been regarded. The acceptance A is defined as

$$A = \left.\frac{N_{gen}^{acc}}{N_{gen}}\right|_{vis} . \tag{10.5}$$

The acceptance cuts applied to the generated events are summarized in table 10.2. The limited

Acceptance cuts	
$p_T(K)$	$> 0.5\,\mathrm{GeV}$
$p_T(\pi)$	$> 0.3\,\mathrm{GeV}$
$p_T(\pi_{slow})$	$> 0.12\,\mathrm{GeV}$
$p_T(K) + p_T(\pi)$	$> 2.2\,\mathrm{GeV}$
$\lvert\eta(K, \pi, \pi_{slow})\rvert$	< 1.73
f	> 0.1

Table 10.2: *Definition of the acceptance cuts on transverse momenta and pseudorapidity of the tracks of the decay particles are shown.*

range in pseudorapidity ensures that the tracks can be detected with the central tracking devices and the cuts in the transverse momenta of the decay particles ensure proper track reconstruction. The cuts on the sum of kaon and pion transverse momenta and on the quantity f reduce the combinatorial background.

The distribution of the acceptance in dependence of the D^* quantities $p_T(D^*)$, $\eta(D^*)$, $z(D^*)$ and of $W_{\gamma p}$ for PYHTIA and CASCADE MC predictions are presented in figure 10.3. The PYTHIA MC is used for data correction and the histogram bins here correspond to the analysis bins for the cross section measurements. The acceptance correction factor is applied bin by bin to the cross section calculation. In addition the CASCADE MC is shown because it is used for the determination of the model uncertainty.

The acceptance decreases rapidly towards low $p_T(D^*)$. The cut $p_T(\pi_{slow}) > 0.12\,\mathrm{GeV}$ ensures

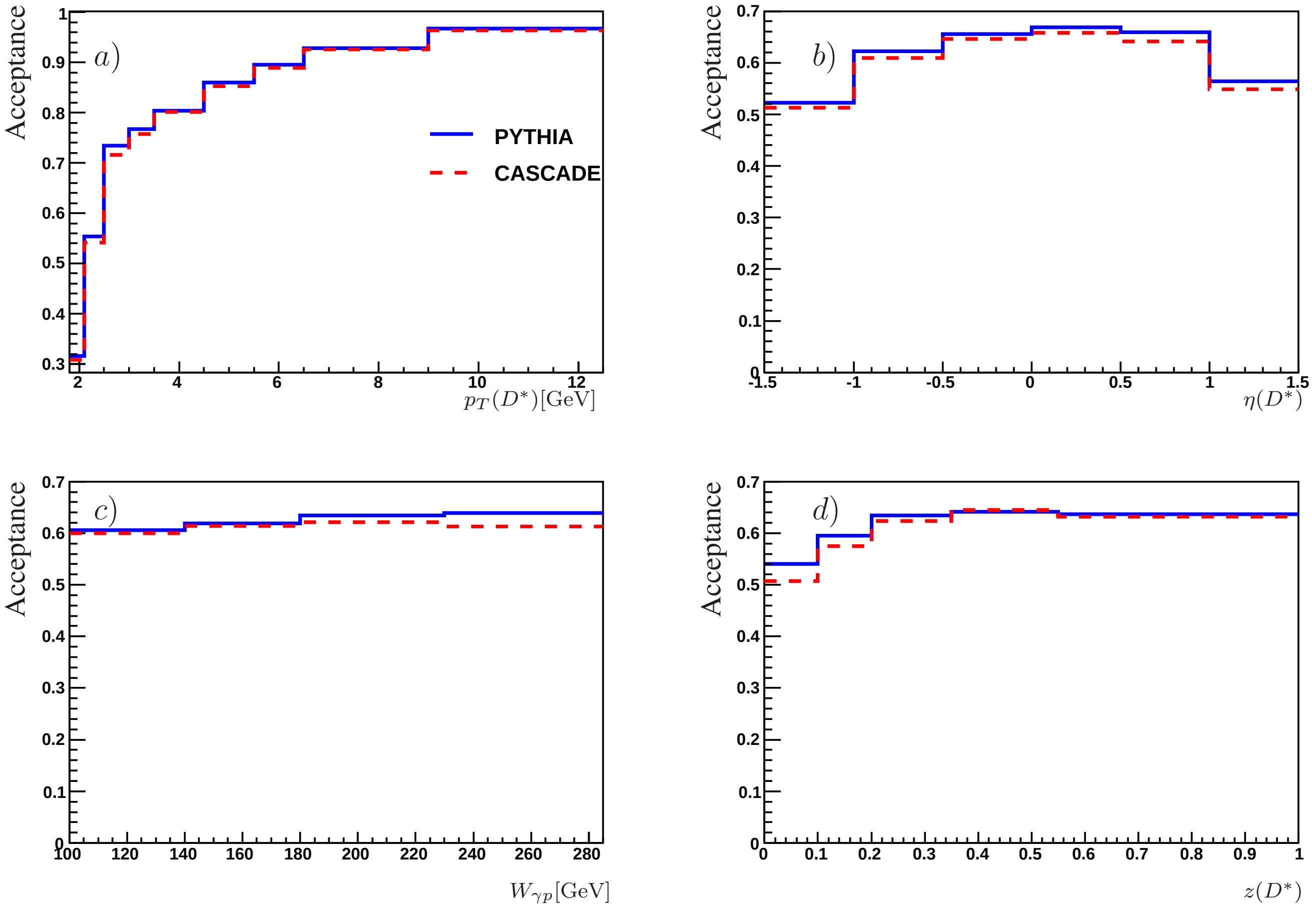

Figure 10.3: *Acceptance as a function of $p_T(D^*)$, $\eta(D^*)$, $W_{\gamma p}$ and $z(D^*)$ for the leading order MC PYTHIA (blue dashed line) and CASCADE (red continous line).*

a good track measurement in the central jet chambers but is relatively high and leads to particle losses in the low p_T regime. The acceptance in the forward and backward regions in the pseudorapidity distribution are around 10% lower than in the central region because the D^* decay particles may leave the CJC. Although the quantities $W_{\gamma p}$ and $\eta(D^*)$ are correlated, the acceptance in $W_{\gamma p}$ is nearly flat whereas the acceptance in $\eta(D^*)$ shows a dependency. The absence of such a dependence is due to the coarse binning used in $W_{\gamma p}$.
The inelasticity $z(D^*)$ reveals a decreasing acceptance to low inelasticities. The less energy transfer to the D^* correspond to low transverse momenta of the D^* where the acceptance is low. At low $z(D^*)$ less energy from the photon is transferred to the D^* mesons, which means that in the hard process or in the fragmentation many additional particles are produced.
When comparing the distributions of the two MC simulation small differences are observed which are taken into account in the model uncertainty.

Reconstruction Efficiency

The cross section formula 10.1 includes the reconstruction efficiency which is defined as the ratio of the number of reconstructed D^* mesons to the number of generated accepted D^* mesons in the visible range

$$\epsilon_{rec} = \left.\frac{N_{rec}}{N_{gen}^{acc}}\right|_{vis} . \tag{10.6}$$

The number of reconstructed D^* mesons N_{rec} after the full detector response is determined with a simultaneous signal and background fit, see section 7.3.

The reconstruction efficiency is depicted for PYTHIA and CASCADE for all measured quantities in which the cross section is extracted in figure 10.4.

The reconstruction efficiency as a function of the transverse momentum of the D^* meson reveals lower efficiencies towards small and high $p_T(D^*)$. Low $p_T(D^*)$ corresponds to very low transverse momenta of the slow pion at which the limit of track measurement with the CJCs is reached. Hence in the low $p_T(D^*)$ bins the efficiency worsens. At high momenta the track resolution deteriorates and the track separation worsens because the tracks are close together. This leads to a lower reconstruction efficiency. Overall the reconstruction effiency is around 70%.

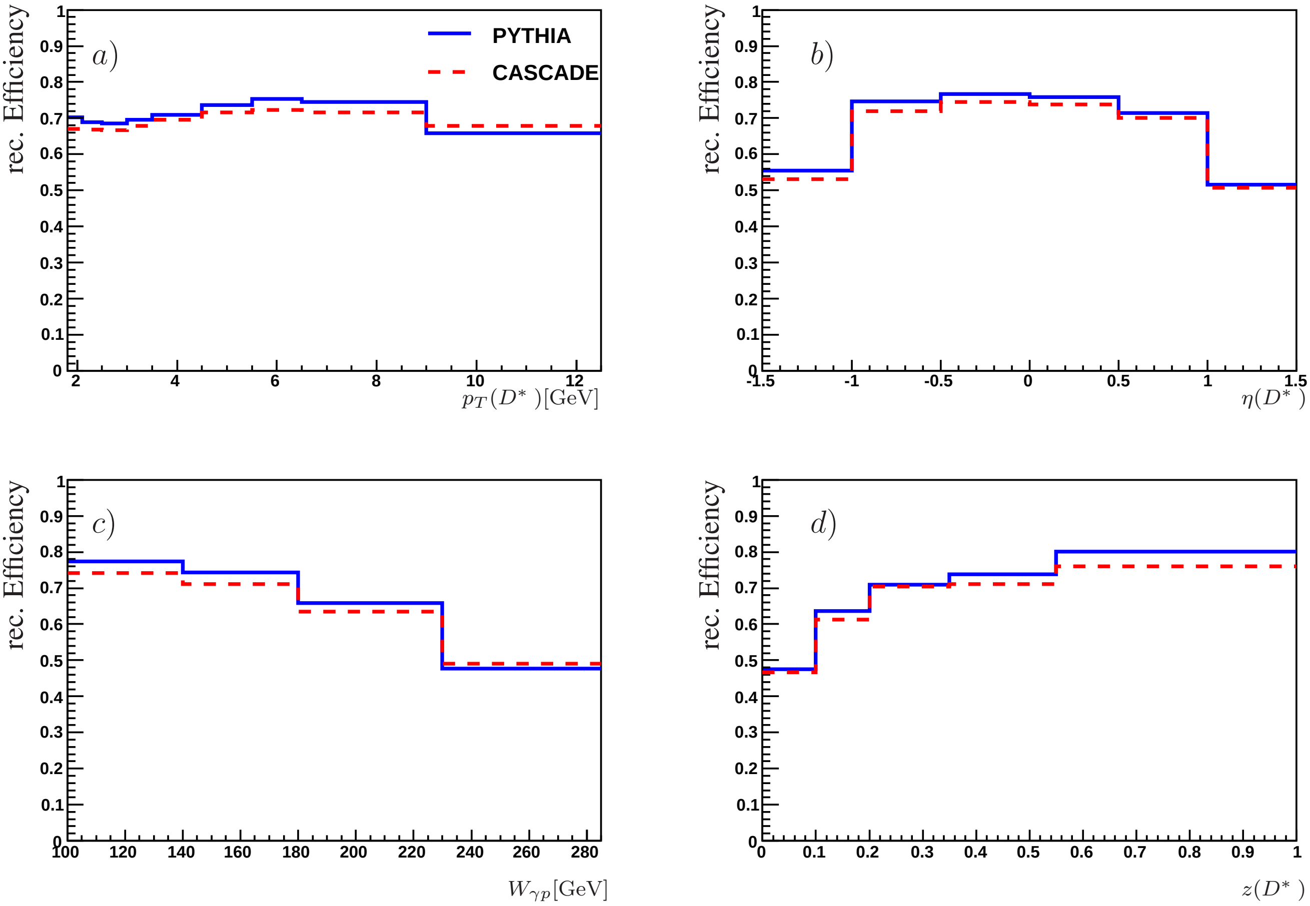

Figure 10.4: *Reconstruction efficiency as a function of* $p_T(D^*)$, $\eta(D^*)$, $W_{\gamma p}$ *and* $z(D^*)$ *for the leading order MC PYTHIA (blue line) and CASCADE (red line).*

The pseudorapidity of the D^* shows in the central region a reconstruction efficiency of 75%. In the forward and backward regions a decrease to an efficiency of 50% is observed. In this regions particle traverse only small parts of the CJC which leads to worse track reconstruction

than for particles which cross the CJC in the central region.
The reconstruction efficiency as a function of $z(D^*)$ increases from 50% at low D^* inelasticities up to 80% in the last bin which corresponds to a high energy transfer. The increase of the efficiency is due to the decrease of the number of additional tracks towards higher $z(D^*)$. Less particles are in the CJC which results in a simpler track reconstruction than for events with many tracks.
Further the dependence on $W_{\gamma p}$ is studied. The reconstruction efficiency falls towards high $W_{\gamma p}$ from 75% to 50%. This is a similar effect as in $z(D^*)$, large $W_{\gamma p}$ correspond to higher track multiplicities. Like in the acceptance distributions the two MC simulations from PYTHIA and CASCADE have overall a similar reconstruction efficiency and the minor differences which are visible are considered in the model uncertainty.

10.3 Systematic Uncertainties

The major sources of systematic uncertainty in this measurement are the luminosity measurement, the trigger efficiency and the track finding efficiency. All sources of systematic errors are added in quadrature which results to 10.3% systematic error in total. The effects of the individual uncertainties are summerized in table 10.3.
In general the systematic uncertainties are grouped to bin-to-bin uncorrelated, bin-to-bin correlated uncertainties and to uncertainties which only have influence on the pure normalization of the cross section.

The uncertainties due to the signal extraction, the D^0 meson mass cut, the reflections, the DIS background and the dE/dx cut are assumed to be bin-to-bin uncorrelated. For example, with the uncertainty of the D^0 meson mass cut the possible dependence on other, so far not considered, kinematic variables is taken into account. The track finding efficiency has a correlated and an uncorrelated part. In data and MC the track finding efficiency can be slightly different, because in data the determination of the track finding efficiency is difficult due to the statistical limitation. This leads to a correlated part of the uncertainty of the track finding efficiency, which only effects the normalization. In addition, the simulation of the dependence on the momentum, the transverse momentum and on the angle θ is not properly, which leads to an uncorrelated part of the uncertainty. It is assumed that the track finding efficiency is half bin-to-bin correlated and half uncorrelated.
The uncertainties of the trigger efficiency, the model, the fragmentation and the hadronic energy scale are expected to be bin-to-bin correlated. The trigger efficiency is assumed as bin-to-bin correlated for the following reason. The dependence on all studied kinematic variables in data and MC agree after the correction of trigger simulation. Therefore it is assumed that the trigger efficiency uncertainty is mainly related to the total trigger efficiency and effects different bins in a correlated way. The uncertainty due to the fragmentation arises due to the statistical uncertainty of the H1 measurement [60]. The 'true' value is expected to be within the statistical uncertainty of this measurement and a change of the true value has a correlated effect on each distribution.

The uncertainty of the luminosity and the branching ratio do purely effect the normalization of the cross section measurement.

In the following the sources and size of each uncertainty is studied and the numbers for the uncertainties are given in per cent of the cross section values. First the bin-to-bin uncorrelated uncertainties will be discussed, then the ones which are correlated between the bins and at last the normalization uncertainties.

Uncorrelated uncertainties

Signal Extraction

The number of D^* mesons is determined with a fit of the sum of signal and background functions. For the signal fit a Crystal Ball function and for the background a Granet parametrization was used. To estimate the uncertainty due to the choice of the fit parametrization, the number of

Uncorrelated errors:	
Signal extraction	1.5%
Track efficiency	4.1%
D^0 meson mass cut	2.0%
Reflections	1.0%
DIS background	0.3%
dE/dx cut	0.5%
Correlated errors:	
Trigger efficiency	6.6%
Model uncertainty	2.0%
Fragmentation	2.5%
Hadronic energy scale	0.6%
Normalization	
Luminosity	5.0%
Branching ratio	1.5%
Sum	10.3%

Table 10.3: *Summary of the systematic uncertainties of the cross section measurement and the typical uncertainty value for each source. The uncertainty sources are grouped into bin-to-bin uncorrelated and bin-to-bin correlated sources.*

D^* mesons is obtained with two different parametrizations for the signal function and the background function. The resulting numbers of D^* mesons have been compared. For the signal the Crystall Ball and the Bukin parametrization [118] have been used. The Bukin parametrization

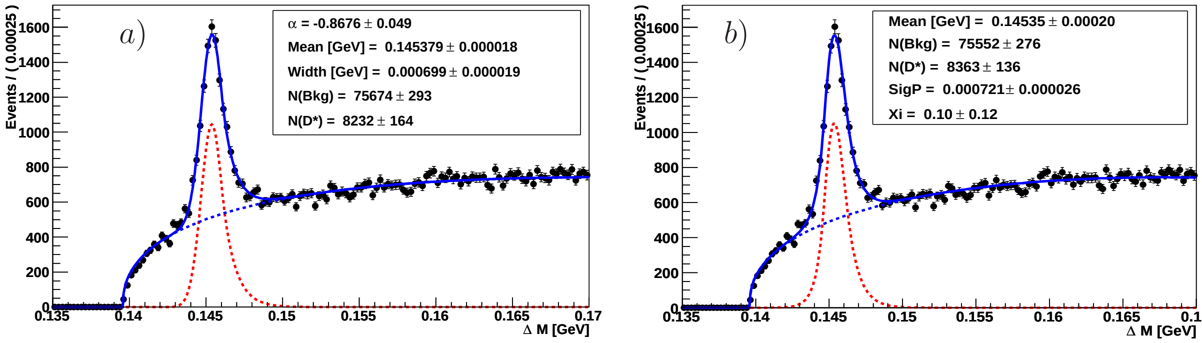

Figure 10.5: *Distribution of ΔM for D^* candidates. The signal and background are fitted with the sum of a Crystal Ball signal function with a Granet background function in a) and the sum of a Bukin signal function with a polynomial background function in b).*

is defined according to [118]

$$f_{Bukin}(x) = A \cdot \exp\left(-(ln2) \cdot \left[\frac{ln(1 + 2\xi\sqrt{\xi^2+1}\frac{m-m_p}{\sigma_p\sqrt{2ln2}})}{ln(1 + 2\xi^2 - 2\xi\sqrt{\xi^2+1}} \right]^2 \right), \tag{10.7}$$

with the peak position m_p, the width of the peak σ_p and the peak asymmetry parameter ξ. A further description of this parametrization is given in [116].

The background is fitted with the Granet parametrization and with a polynomial function

$$f(x) = \begin{cases} (m - m_\pi)^a \cdot (1 - b \cdot m^2) & \text{for } m \geq m_\pi \\ 0 & \text{for } m < m_\pi \end{cases} \tag{10.8}$$

with $m = \Delta M$, the fit parameters a and b and the pion mass m_π. The ΔM distribution of the full data sample is fitted with both signal function in combination with both background parametrizations. The resulting number of D^* mesons for each combination is summarized in table 10.4.

Signal + Background function	N(D^*)
Crystal Ball + Granet	8232 ± 164
Crystal Ball + polyn.	8265 ± 151
Bukin + Granet	8243 ± 140
Bukin + polyn.	8363 ± 136

Table 10.4: *Fit results of fits with different parametrizations for the* ΔM *distribution.*

The combinations of the Crystal Ball signal function with the Granet background parametrization and of the Bukin signal function with a polynomial background parametrization reveal the largest differences. Therefore the relative difference of this combinations which amounts to 1.5% is assigned as uncertainty. The fit results of this two parameterizations is presented in figure 10.5.

Track finding efficiency

Another dominant error source of the cross section measurement originates from the track finding. This uncertainty arises from two contributions:

First the number of measured D^* mesons has to be corrected for detector effects with MC simulations. Hence an uncertainty occurs from possible differences in the track finding efficiency between data and MC simulation. Three effects have to be considered for not finding a track. First, no tracks are found because the particle is absorbed in the dead material. Another effect is that not enough hits were detected to find a non–vertex fitted track. In addition, the algorithm may not find a track although hits are there. The track finding efficiency for low momentum tracks was studied with pion tracks from the decay $K^0 \rightarrow \pi\pi$ which curl inside the Central Jet Chambers [126, 127]. The reconstruction of these tracks has to deal with parts of the track inside the CJC1 and parts of the tracks inside the CJC2 after passing the dead material between

the two jet chambers under shallow angles. It was found that data and MC have differences in the track finding efficiency which have to be taken into account as systematic uncertainty on the track finding. More precisely an error of 2% for the slow pion track and 1% for the kaon and pions [127] from the D^0 decay are assigned. To be conservative the uncertainty is treated as fully correlated between the decay particles of a D^* meson, leading to a total uncertainty of 4% per D^* .
Secondly there is a systematic error originating from the efficiency of fitting a track to the event vertex. This cannot be determined with the method described before due to the long lifetime of the K^0 which results in a secondary vertex. In general the determination of the systematic uncertainty can be done with the following method described in detail in [116]. The ΔM distributions of vertex fitted and non–vertex fitted tracks have been fitted separately and the primary vertex fit efficiency is calculated with the ratio of the number of D^* mesons of the vertex fitted tracks to the number of D^* mesons of the non–vertex fitted tracks. The uncertainty found in [116] amounts to 2.5%. Due to the highly statistical limitation of this method the primary vertex fit efficiency was newly determined for the D^* meson production in deep inelastic scattering with a different method, see [128]. The distribution of the distance of closest approach is the crucial factor if a track is vertex fitted or not. Within a certain range corresponding to 4.47σ around the vertex position of the distribution the tracks are fitted to the vertex, whereas they are not fitted if they are located outside this range. The uncertainty is estimated by comparing tails of the distributions in data and MC simulation. In general a good agreement is observed and the systematic uncertainty is quoted to be approximately 1% [128]. This is added in quadrature. Hence the total systematic uncertainty on the track finding to the cross section measurement amounts to 4.1%.

D^0 mass cut

The cut on the D^0 mass window of $\pm 80\,\mathrm{MeV}$ around the nominal D^0 mass can reduce significantly the huge combinatorial background present in this analysis but has to be regarded as an additional source of systematic error to the cross section measurement. The track resolution in data is observed to be slightly worse than in the MC simulation so that the peak position and width of the D^0 mass peak can be different. This results in a different fraction of D^* mesons which are lost for the further analysis, because they are, due to the tightness of the D^0 mass window, reconstructed outside the allowed D^0 mass window.
The uncertainty on the D^0 mass window is determined by estimating the amount of D^* meson losses for data and MC. First the $M(K\pi)$ distribution in bins of the transverse momentum of the D^* meson is fitted with a Gaussian function for events passing all other selection cuts except the $M(K\pi)$ cut and the peak position and the width of the peak for data and MC are compared.

The upper part of figure 10.6 shows the peak position and width for data and MC simulation in bins of the transverse momentum of the D^* meson. The two outer solid lines represent the D^0 mass window of $\pm 80\,\mathrm{MeV}$ around the nominal D^0 mass and the inner solid line the nominal D^0 mass value. The peak position of the D^0 peak is displayed as data point and the error bars represent the peak width. Overall it is observed that the peak position in data is slightly lower than for the MC simulation. A broadening of the peak width towards higher transverse momentum, which is due to the worsening of the track resolution towards higher p_T, is found in data

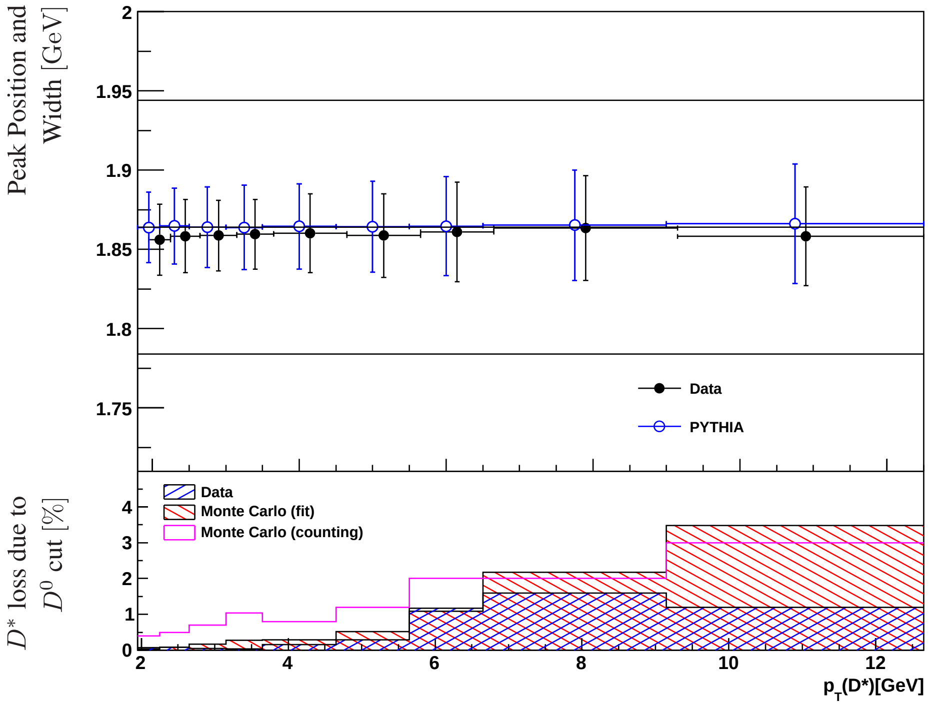

Figure 10.6: *The peak position and width of the* D^0 *signal are presented for data and PYTHIA MC in the upper part of the figure. The* D^* *loss due to the* D^0 *cut is estimated in the lower part with using a fit method for data and MC and by counting the MC events inside and outside the cut.*

and MC simulation. In the former photoproduction analysis of [120] it was observed that the peak width for data increases towards low transverse momentum of the D^* but for MC remains constant towards low p_T. This is not the case in the present analysis and can be explained with the use of the final detector simulation, which includes a new description of dead material which ensures that multiple interaction which dominate in the low transverse momentum regime are properly simulated.

In the lower part of figure 10.6 the amount of D^* meson losses due to the D^0 mass cut are presented for data and MC simulation. The fraction of D^* mesons which have been reconstructed outside the allowed D^0 mass window has been determined with the integral of the Gaussian fit in each p_T bin. In the low transverse momentum region a good agreement is found between data and MC simulation, whereas in the high momentum region difference up to 2% occur. This method assumes that the Gaussian fit gives a good description of the $M(K\pi)$ distribution. Due to large background this assumption cannot be tested in data, but only for MC. A further study was performed using the $M(K\pi)$ distribution of the MC simulation only for events where the kaon and the pion originate from a D^0 decay. The number of D^* mesons reconstructed inside and outside the allowed D^0 mass window is determined by counting events and not with applying a Gaussian fit. The counting result is shown as pink solid line and reveals an agreement with the data within 2%. The 2% difference was assigned as error to the cross section measurement.

Reflections

The cross section formula 10.1 includes a correction due to reflections. The reflections are other decays of the D^0 than $D^0 \rightarrow K^+\pi^-$ in the golden decay channel. They are summarized in table 10.5. Other decay channels of the D^* meson do not contribute, because they would not lead to a peak in the ΔM distribution at the correct value. But other decays of the D^0 can produce a peak in the ΔM histogram and contribute to the signal.

The amount of reflections r was determined in [89] by fitting the ΔM distribution only for events which have been identified as reflections on generator level and comparing the extracted number of D^* mesons with the fit result of the ΔM distribution with all events. The correction factor due to reflections is found to be 3.8% with a constant dependence on kinematic quantities within 1% in the DIS regime [89]. Since the phase space for the D^* meson and the selection cuts for the D^* decay particles are very similar, the values can be used for this analysis. The cross section is corrected for the amount of reflections and 1% is assigned as uncertainty.

decay channel	Branching ratio
$D^0 \rightarrow K^\pm K^\mp$	$(3.94 \pm 0.07) \cdot 10^{-3}$
$D^0 \rightarrow K^\mp \pi^\pm \pi^0$	$(13.9 \pm 0.05)\%$
$D^0 \rightarrow \pi^\mp \pi^\pm$	$(1.397 \pm 0.026) \cdot 10^{-3}$
$D^0 \rightarrow \pi^\mp \pi^\pm \pi^\mp \pi^\pm$	$(7.44 \pm 0.21) \cdot 10^{-3}$
$D^0 \rightarrow \pi^\mp \pi^\pm \pi^0$	$(1.44 \pm 0.06)\%$
$D^0 \rightarrow K^\mp e^\pm (\bar{\nu_e})$	$(3.55 \pm 0.05)\%$
$D^0 \rightarrow K^\mp \mu^\pm (\bar{\nu_\mu})$	$(3.31 \pm 0.13)\%$
$D^0 \rightarrow \pi^\mp e^\pm (\bar{\nu_e})$	$(2.89 \pm 0.08) \cdot 10^{-3}$
$D^0 \rightarrow \pi^\mp \mu^\pm (\bar{\nu_\mu})$	$(2.37 \pm 0.24) \cdot 10^{-3}$

Table 10.5: *Summary of decay channels of the D^0 meson taken into account for the correction of the reflection and the corresponding branching ratios [16]. These decays lead to two or more charged decay particles in the detector.*

Deep inelastic scattering background

The background which originates from deep inelastic scattering events was estimated by studying the fraction of DIS events in the total data sample.

The photoproduction regime in this analysis is defined by demanding $Q^2 < 2\,\mathrm{GeV}^2$. The photoproduction MC from PYTHIA, which is used for the cross section correction, was generated with an upper cut of $Q^2 < 5\,\mathrm{GeV}^2$. The fraction of DIS events in the Q^2 range from $2-5\,\mathrm{GeV}^2$ is taken into account by the reconstruction efficiency using the PYTHIA MC.

It is known that the RAPGAP MC describes the DIS regime properly [89]. To study if the PYTHIA MC gives a sufficient discription of the Q^2 range from $2-5\,\mathrm{GeV}^2$ the generated Q^2_{gen}

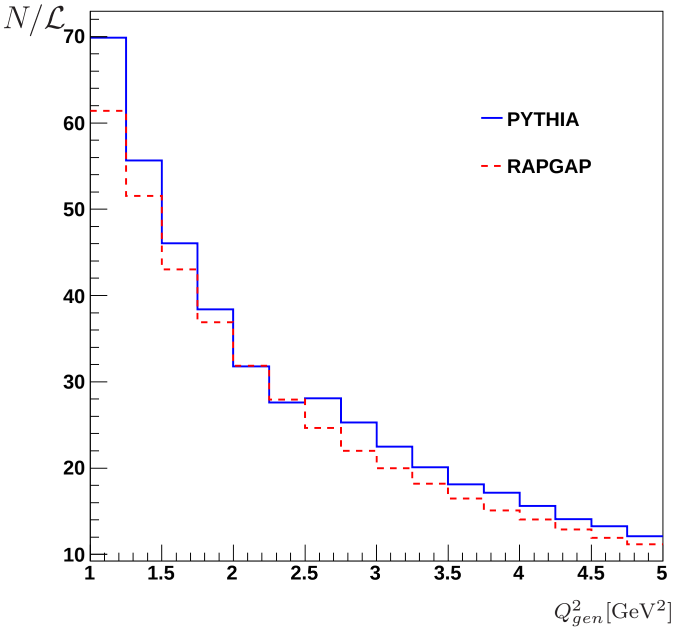

Figure 10.7: *The generated Q^2_{gen} distribution for PYTHIA and RAPGAP.*

distributions of RAPGAP and PYTHIA MC in the range from $2 < Q^2 < 5\,\mathrm{GeV}^2$ are compared. In figure 10.7 the number of events normalized to the luminosity as a function of Q^2_{gen} is depicted. A good agreement between the two MC simulations is observed.
The migration from outside the $Q^2 < 5\,\mathrm{GeV}^2$ range was investigated with an DIS RAPGAP MC which has a lower cut on $Q^2 > 5\,\mathrm{GeV}^2$ and a luminosity of $\mathcal{L}_{rap} = 2647,49\,\mathrm{pb}^{-1}$. After passing all selection and kinematic cuts the number of D^* events is determined with a signal fit, see section 7.3, to $N_{rap}(D^*\ ) = 643.44$ which corresponds to a yield of $\frac{N_{rap}(D^*\ )}{\mathcal{L}_{rap}} = 0.24\,\mathrm{pb}$. This result is compared to total production yield of the photoproduction data integrated over the full phase space $\frac{N_{data}(D^*\ )}{\mathcal{L}_{data}} = 72.76\,\mathrm{pb}$. Hence the uncertainty arising from DIS background events amounts to 0.3%.

dE/dx cut

The huge combinatorial background is suppressed with a cut on the likelihood of the specific energy loss of kaon candidates of $LH_{kaon} > 0.02$. The uncertainty introduced by this cut is estimated with studying the cut efficiency in data and MC simulation.
The cut efficiency in bins of the transverse momentum of the D^* mesons is determined by fitting simultaneously the ΔM distributions of the rejected and accepted events with an additional fit parameter ϵ which is the cut efficiency. This fit procedure was earlier described in section 9.
In figure 10.8 a) the cut efficiency as a function of the transverse momentum of the D^* mesons for data and MC simulation is presented, which is slightly lower for data then for MC. The ratio of the data over MC efficiencies is shown in figure 10.8 b). It is fitted with a polynomial of first

order to 0.985 ± 0.005. Hence the cross section measurement is corrected with a correction factor of 1.015. The fit uncertainty of 0.5% is assigned as systematic uncertainty of the measurement.

Correlated Uncertainties

In the following paragraphs the correlated error sources of the trigger efficiency, the model uncertainty, the fragmentation and the hadronic energy are discussed:

Trigger Efficiency

The source of one of the major uncertainties in this analysis is the trigger efficiency. The trigger efficiency is taken from the MC simulation and was reweighted to the data. The reweighting functions are shown in section 9. For subtriggers s55 and s122 the fit uncertainty of the reweighting function is used to estimate the systematic uncertainty of the trigger efficiency in the corresponding transverse momentum range. Subtrigger s53 was not reweighted because a good agreement between data and MC was observed. For the estimation of the uncertainty for the p_T region of subtrigger s53 the ratio of the trigger efficiency in data and MC is calculated and fitted with a first order polynomial (see figure 10.9), so that the fit uncertainty can be used

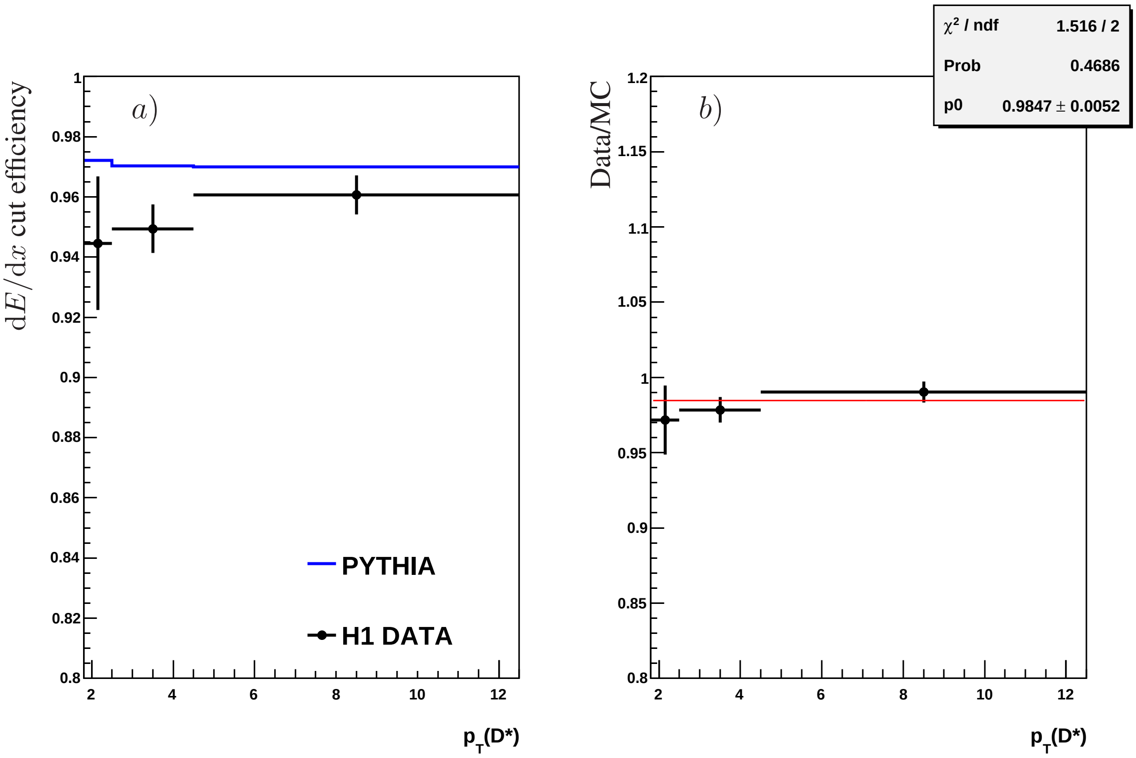

Figure 10.8: *The* $\mathrm{d}E/\mathrm{d}x$ *cut efficiency as a function of the transverse momentum of the* D^* *for data and PYTHIA MC is displayed in a). The resulting ratio of the data to the MC simulation with the fit result is illustrated in b).*

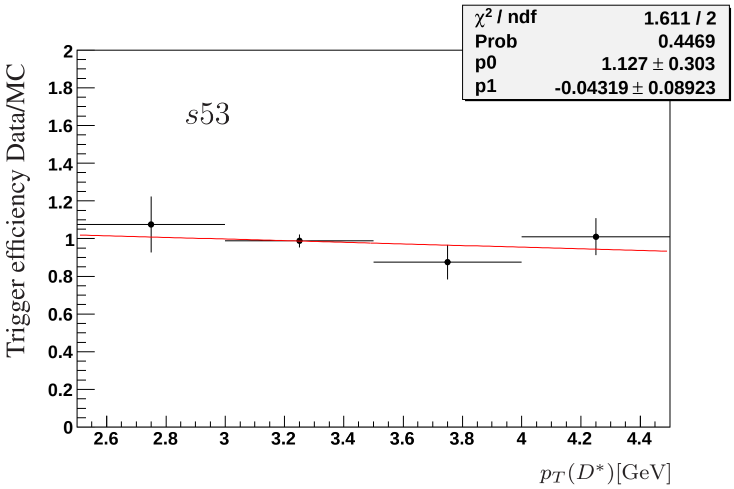

Figure 10.9: *The ratio of the trigger efficiency of s53 in data and MC together with the fit result.*

too.

The relative uncertainty of the cross section measurement due to the trigger efficiency $\delta_{triggeff.}$ is determined by varying the trigger efficiency up- and downwards by the fit uncertainty of the reweighting function and comparing the nominal cross section value σ_{nom} with the cross section value of the variations $\sigma_{var}^{\pm}$:

$$\delta_{triggeff.}^{\pm} = \frac{\sigma_{var}^{\pm} - \sigma_{nom}}{\sigma_{nom}}. \qquad (10.9)$$

In figure 10.10 the relative error of the cross section measurement due to the trigger efficiency as a function of $p_T(D^*)$, $\eta(D^*)$, $W_{\gamma p}$ and $z(D^*)$ is presented. For comparison the relative statistical error of the cross section in data is shown too. For most parts the systematic uncertainty dominates the statistical uncertainty. The uncertainty is nearly independent of pseudorapidity, inelasticity and $W_{\gamma p}$ with an overall uncertainty of around 6.6%.
The uncertainty as a function of the transverse momentum of the D^* meson reveals clear structures corresponding to the subtriggers. The first two bins at low $p_T(D^*)$ correspond to subtrigger s55. The fit of the ratio data to MC trigger efficiency has an uncertainty of more than 10% which leads to a large uncertainty of the trigger efficiency. In the medium $p_T(D^*)$ range in general a smaller uncertainty of around 6% is observed. The uncertainty in the last bin of subtrigger s122 is again increasing to a value of around 10%. The increase of the uncertainty towards low and high transverse momenta is observed in the systematic and statistical error, also in the DIS monitor sample used to determine and correct the trigger efficiency, the statistics is smaller at low and high $p_T(D^*)$. The trigger efficiency uncertainty is assigned binwise to the cross section measurement. In table 10.3 the average value of the trigger efficiency to the cross section value of 6.6% is listed.

Model

The cross section measurement is corrected for detector effects and limited detector acceptance by applying correction factors which have been earlier introduced as reconstruction efficiency

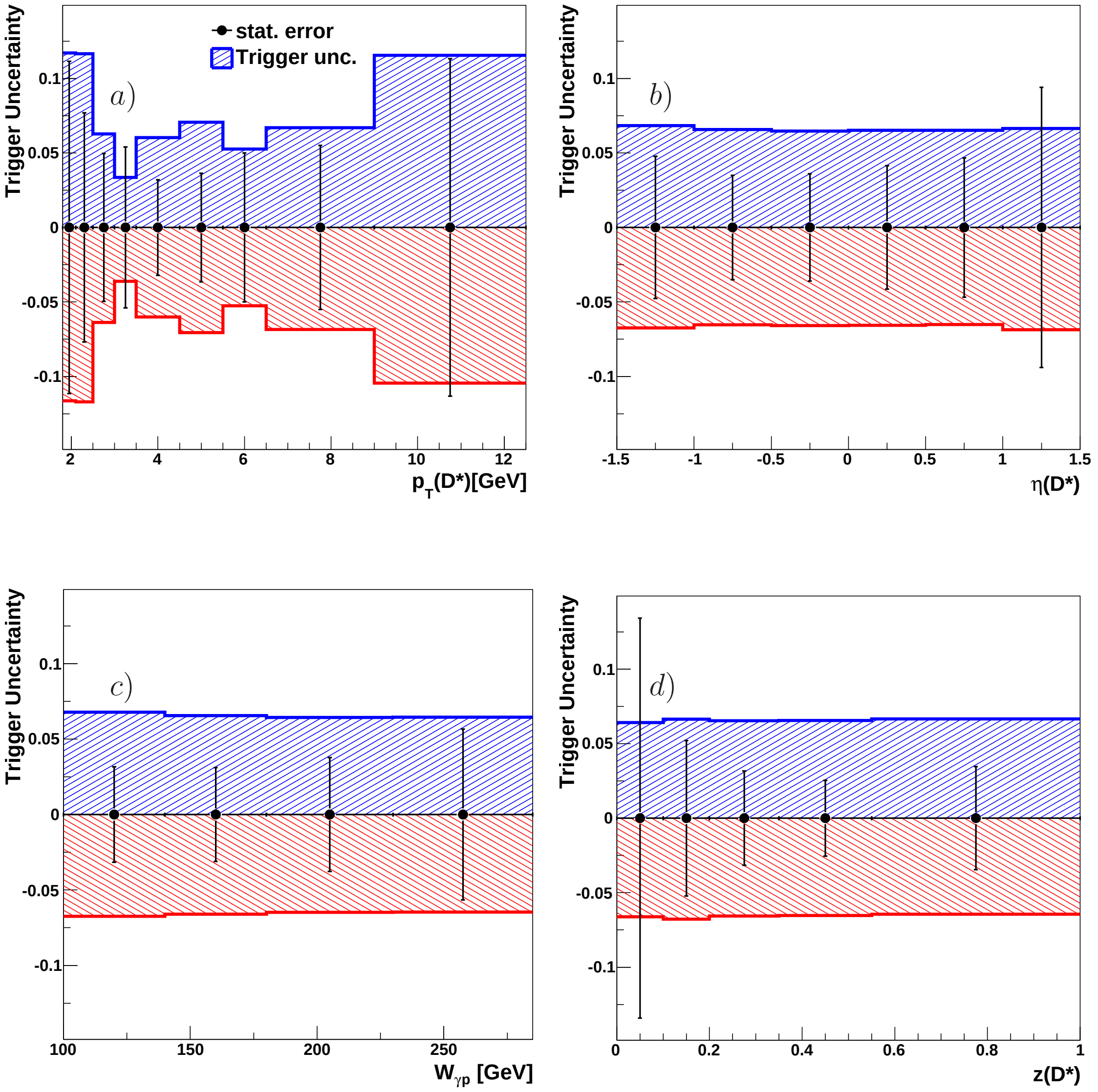

Figure 10.10: *The trigger efficiency uncertainty as a function of* $p_T(D^*)$*,* $\eta(D^*)$*,* $W_{\gamma p}$ *and* $z(D^*)$*. The colors denote the up- (red) and downward (blue) variation by the fit uncertainty of the reweighting function. The relative statistical uncertainty of the data cross section is depicted too.*

and acceptance. The reconstruction efficiency and acceptance in each analysis bin are taken from the PYTHIA MC simulation. To estimate the uncertainty of the cross section extraction due to the MC model which was used, another MC model, CASCADE, has been studied in addition to the PYTHIA MC simulation. These two MC simulations use for example different evolution schemes (DGLAP and CCFM). The relative model uncertainty is estimated by comparing the product of reconstruction efficiency and acceptance for CASCADE MC $U_{CASCADE} = \epsilon_{rec,CASCADE} \cdot A_{CASCADE}$ and PYTHIA MC simulations $U_{PYTHIA} = \epsilon_{rec,PYTHIA} \cdot A_{PYTHIA}$ in all quantities in which a cross section measurement has been performed.
The relative difference of $\pm\delta U = \pm(U_{CASCADE} - U_{PYTHIA})/U_{PYTHIA}$ is assigned as relative model uncertainty to the cross section measurement. In figure 10.11 the relative model uncertainty on the cross section measurement for $p_T(D^*)$, $\eta(D^*)$, $W_{\gamma p}$ and $z(D^*)$ distributions are depicted. Positive values denote an increase of the measured cross section value whereas negative values lead to a decrease. In addition to the systematic uncertainty the relative statistical uncertainty of the data is given for each analysis bin.
The $p_T(D^*)$ dependence reveals the largest uncertainty in the small transverse momentum region. A rather flat distribution is found for $\eta(D^*)$ with an overall uncertainty around 2%. The $W_{\gamma p}$ dependence is small except for the last bin. In the last bin the differences in the reconstruction efficiency and the acceptance between the two MC models cancel out, see figure 10.4 and 10.3, which leads to a smaller model uncertainty. The inelasticity distribution has clear structures. The smallest uncertainties are at medium $z(D^*)$, whereas the largest uncertainty of around 4% occurs at low inelasticities. The determined model uncertainty is assigned binwise to each analysis bin of the cross section measurement. The overall value given in table 10.3 amounts to 2%.

Fragmentation

Two sources of uncertainty are introduced by the reweighting procedure described in section 3.2. On the one hand the position of the $\hat{s}$ threshold is uncertain. For the error estimation the position of the threshold is varied within $\pm 20\,\mathrm{GeV}^2$. For each of the up and down variation the PYTHIA MC events have been grouped with respect to the threshold once again and have been reweighted to the Kartvelishvili parametrization with the α parameters given in table 3.1. The influence to the cross section measurement is studied with the ratio of reconstructed to generated events in the visible region. The difference from the nominal value with the threshold at $\hat{s} = 70\,\mathrm{GeV}^2$ to the variations is assigned as systematic uncertainty to each analysis bin of the cross section measurement. The relative error of the fragmentation due to the threshold variation as a function of $p_T(D^*)$, $\eta(D^*)$, $W_{\gamma p}$ and $z(D^*)$ is depicted in figure 10.12. In all measured variables it is observed that the uncertainty is smaller than 1%.

On the other hand the measured α parameters of the H1 publication [60] have uncertainties. To study the impact on the cross section measurement the $\hat{s}$ threshold is set to the central value and the generated z distributions are reweighted to the Kartvelishvili parametrization but now with varying the α parameter within the uncertainties listed in table 3.1. The systematic uncertainty of the cross section due to the uncertainty of the α parameter is estimated by studying again the ratio of reconstructed to generated events in the visible region of the nominal α value

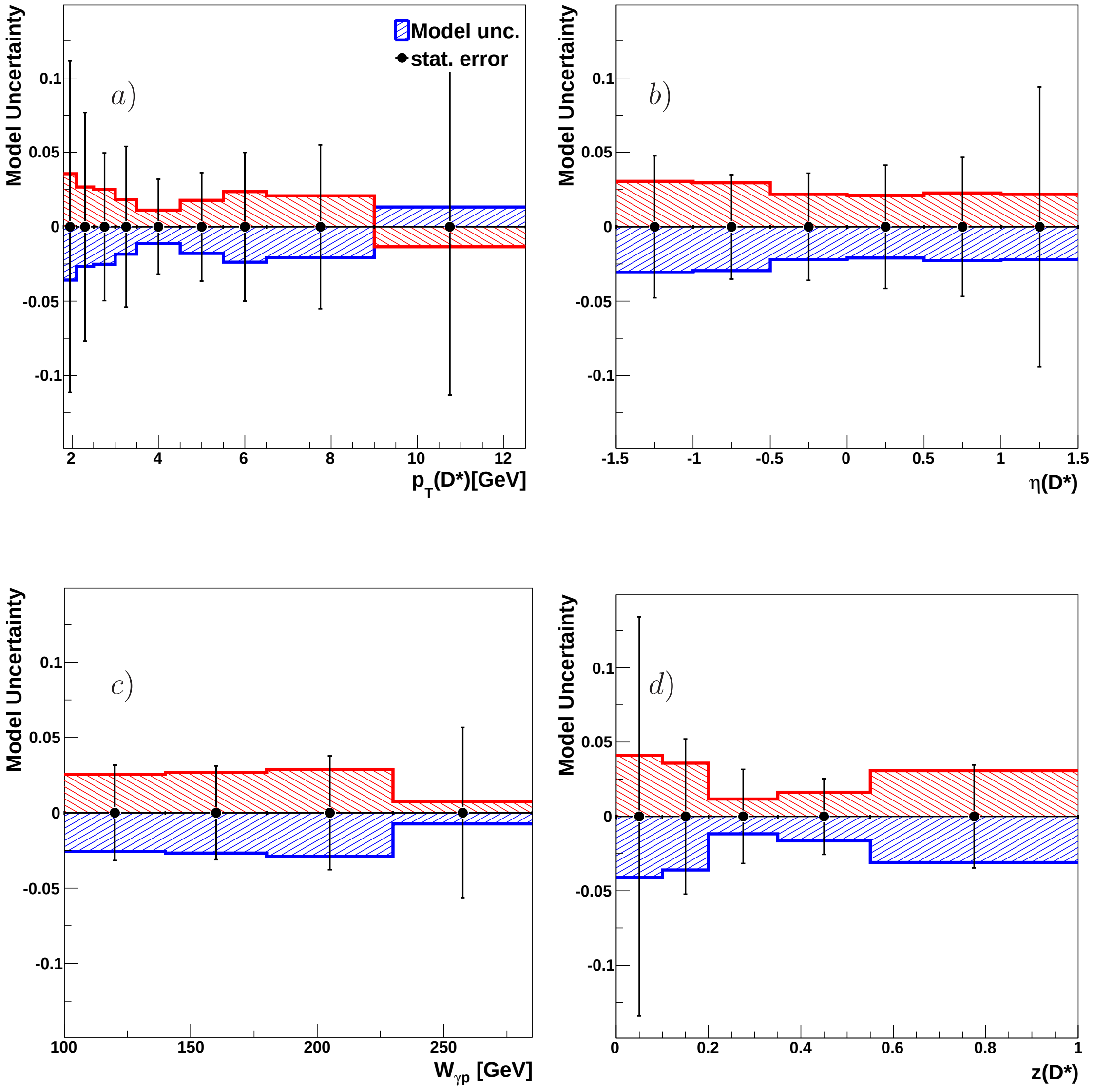

Figure 10.11: *The model uncertainty of the leading order MC simulations PYTHIA and CASCADE as a function of* $p_T(D^*)$, $\eta(D^*)$, $W_{\gamma p}$ *and* $z(D^*)$*. The relative statistical uncertainty of the data is depicted too.*

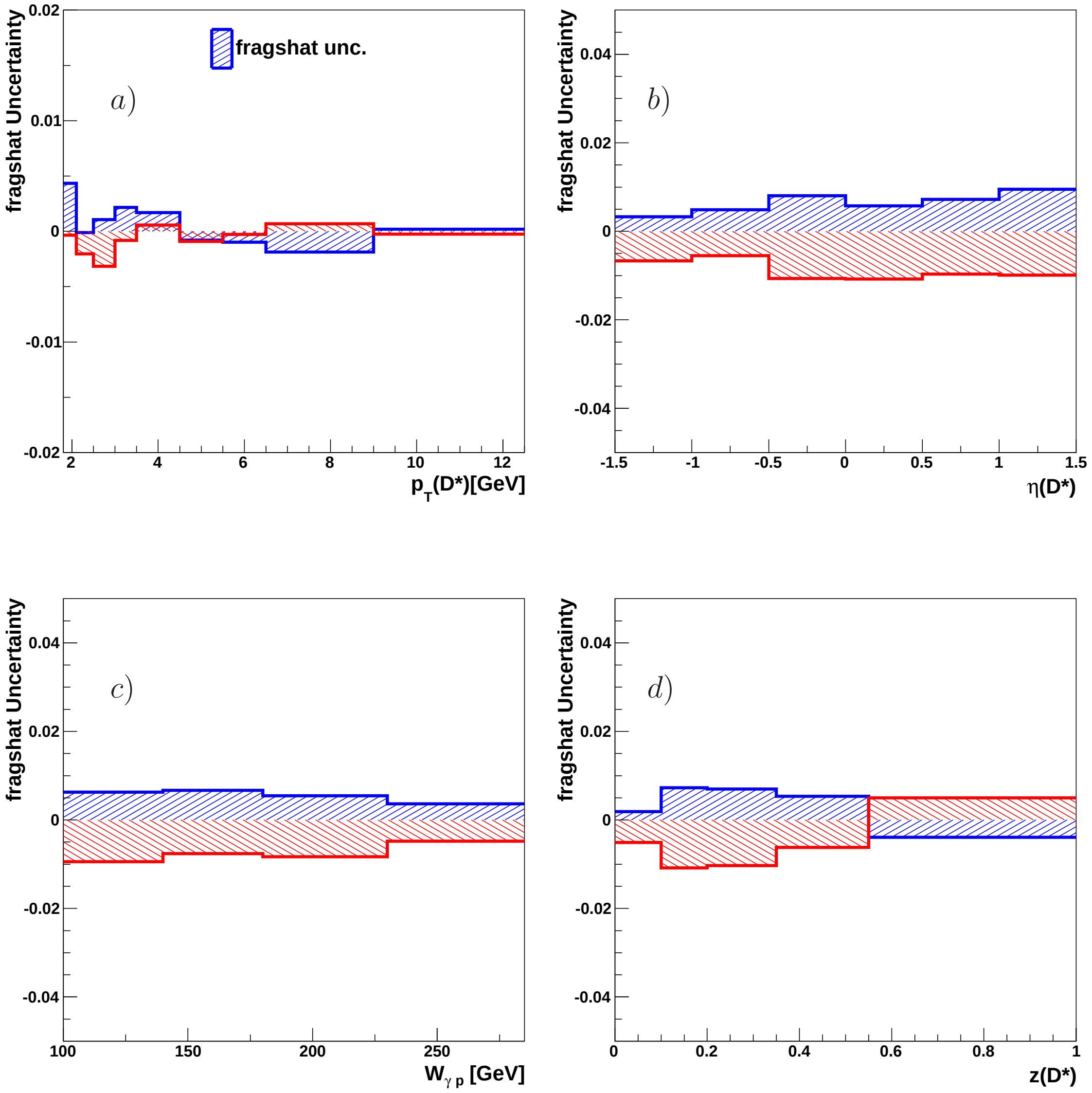

Figure 10.12: *Systematic uncertainty due to the variation of the* $\hat{s}$ *threshold in the* D^* *fragmentation as a function of* $p_T(D^*)$*,* $\eta(D^*)$*,* $W_{\gamma p}$ *and* $z(D^*)$*.*

and of the α variations. The distribution of this relative fragmentation uncertainty as a function of $p_T(D^*)$, $\eta(D^*)$, $W_{\gamma p}$ and $z(D^*)$ is presented in figure 10.13. The overall systematic error, as a consequence of the α variation, is lower than 2%. The full uncertainty of the α and the threshold variation are added in quadrature. Hence the average value for this uncertainty is around 2.5%.

Hadronic energy

At small to moderate energies of the hadronic final state particles as in this analysis, the energy measurement of the HFS has a scale uncertainty of 2% [129]. The effect on the cross section

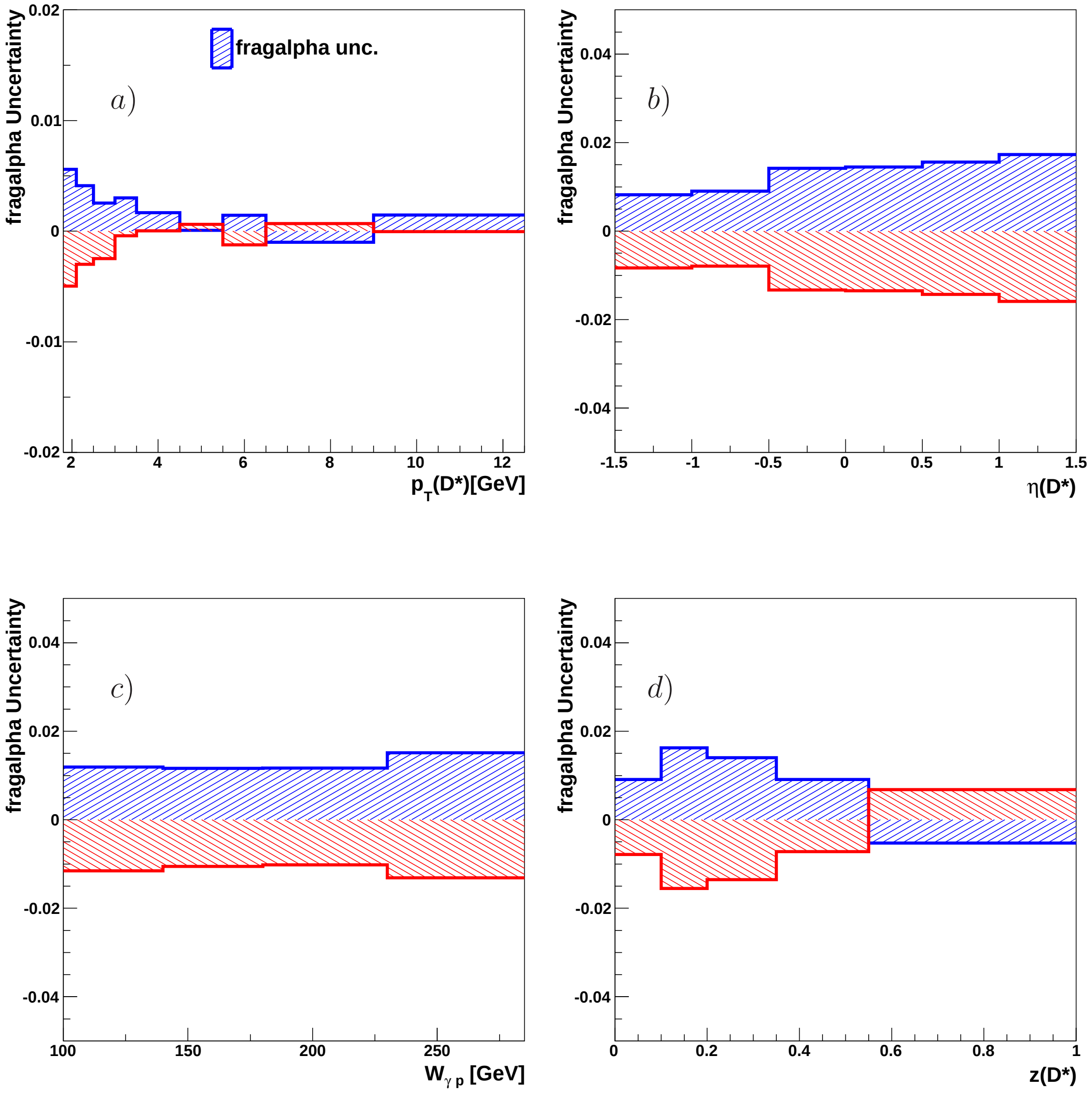

Figure 10.13: *Systematic uncertainty due to the variation of the fragmentation parameter* α *in the Kartvelishvili function as a function of* $p_T(D^*)$, $\eta(D^*)$, $W_{\gamma p}$ *and* $z(D^*)$.

measurement is investigated with a variation of the energy of the HFS particles. In this analysis two cuts in the variables f and y_{had} have been applied which are directly dependent on the HFS energy. Hence the variation of the HFS energy corresponds to a variation of f by

$$f^{\pm} = \frac{p_T(D^*)}{\sum_i^{\theta>10}(E_i + E_i \cdot (\pm 2\%)) \cdot \sin\theta_i} \tag{10.10}$$

and

$$y_{had}^{\pm} = y_{had} + y_{had} \cdot (\pm 2\%). \tag{10.11}$$

Moreover a cross section measurement in the inelasticity $z(D^*)$ was performed which depends directly on the HFS energy because it is reconstructed as $z(D^*) = (E - p_z)_{D^*}/(2yE_e)$. The systematic uncertainty to the cross section measurement is determined by studying the difference of nominal value with no variation to the up- and downward variations.

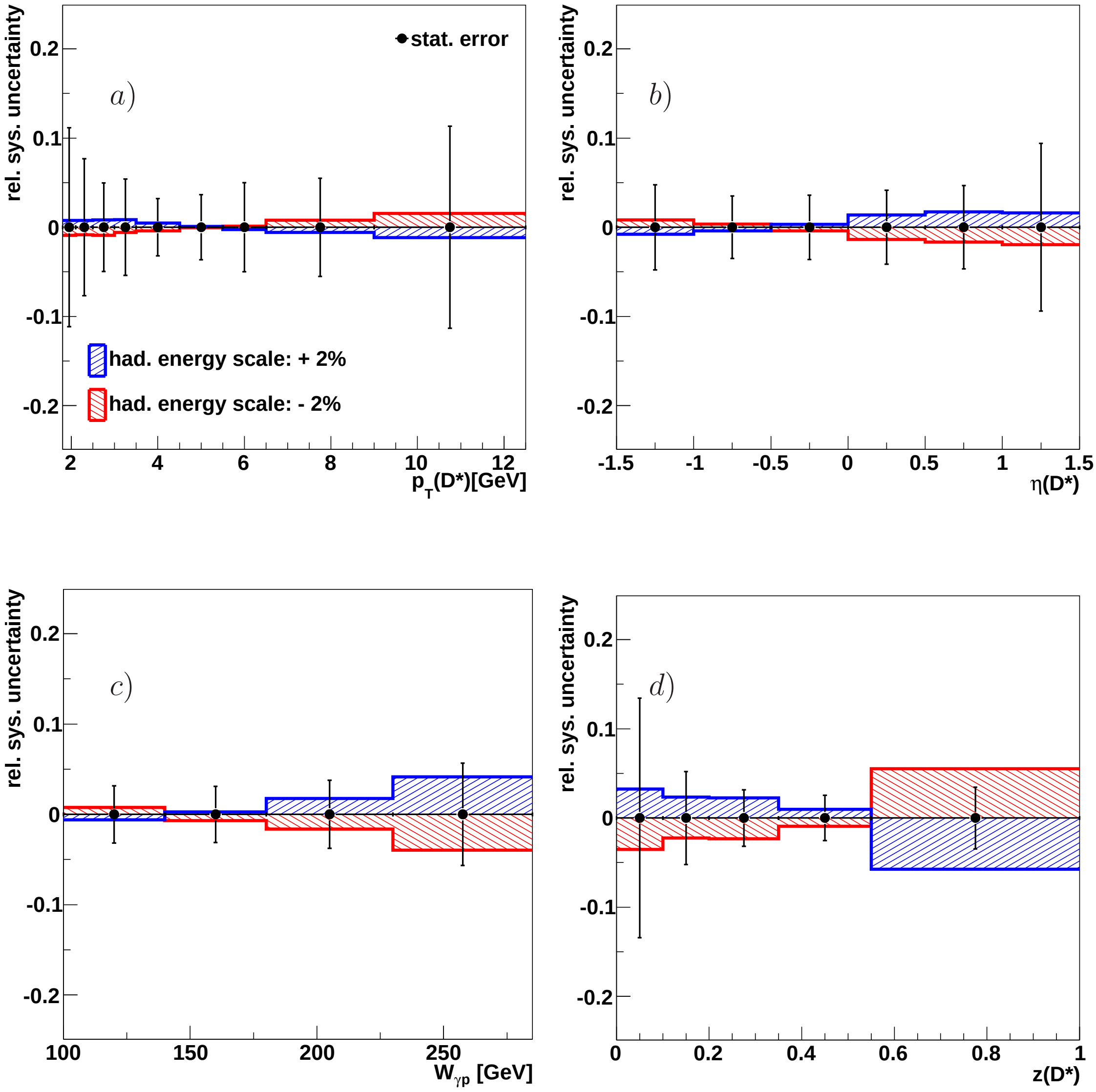

Figure 10.14: *The hadronic energy uncertainty as a function of* $p_T(D^*)$*,* $\eta(D^*)$*,* $W_{\gamma p}$ *and* $z(D^*)$*. The relative statistical uncertainty of the data is depicted too.*

In figure 10.14 the relative error due to the HFS uncertainty as a function of $p_T(D^*)$, $\eta(D^*)$, $W_{\gamma p}$ and $z(D^*)$ is displayed. Again positive values connote an increase of the measured cross section value whereas negative values result in a decrease. The statistical error for each bin is illustrated too.

Since $W_{\gamma p}$ is proportional to y_{had} it is expected that the variation of the HFS energy in y_{had} influences directly the $W_{\gamma p}$ distribution. In the low and medium bins of the photon proton energy $W_{\gamma p}$ the uncertainty is around 2% and shows an increase towards high $W_{\gamma p}$ with an error of around 4% in the highest bin. In the case of the inelasticity $z(D^*)$ the direct dependence on the HFS leads to a higher uncertainty as for the other variables. The uncertainty in the highest $z(D^*)$ bin amounts to $\sim 6\%$ and is a factor two larger than the statistical error. For medium $z(D^*)$ the uncertainty is around 3% with a slightly increase towards small inelasticities. The effect of the HFS energy variation for the variables $p_T(D^*)$, $\eta(D^*)$ which do not depend directly on the HFS energy is not sizeable. For these variables the statistical error dominates the systematic uncertainty. Overall the uncertainty due to the HFS energy scale variation is observed to be a small uncertainty and the influence is on average on the total cross section 0.6%.

Normalization Uncertainty

The uncertainty of the luminosity measurement and of the branching ratio would only influence the normalization of the measurement:

Luminosity measurement

Although in previous analysis the luminosity measurement was a minor source of uncertainty (of around 1.5%), this does not hold for the current analysis. In figure 10.15 the event yield for events with a scattered electron measured in the SpaCal as a function of the run number is shown. Around run number 477000 a jump in the event yield was observed. Until now this feature cannot be explained. Until run number 477000 the overall uncertainty of the luminosity measurement is 2.5%, whereas for later runs it increases to 5%. The photoproduction data which is analyzed in this thesis was recorded in the years 2006 and 2007 in the runs 477240–500611. Therefore an uncertainty of 5% is assigned to the cross section. It is an normalization uncertainty which would shift all measurements in the same direction. The luminosity uncertainty is one of the dominant systematic errors of this analysis.
However the luminosity measurement of the HERAII running period is currently under investigation with a measurement of the QED Compton process, for which the cross section is precisely known and which has a sufficient rate, but the determination of the luminosity correction factors is not final yet [130].

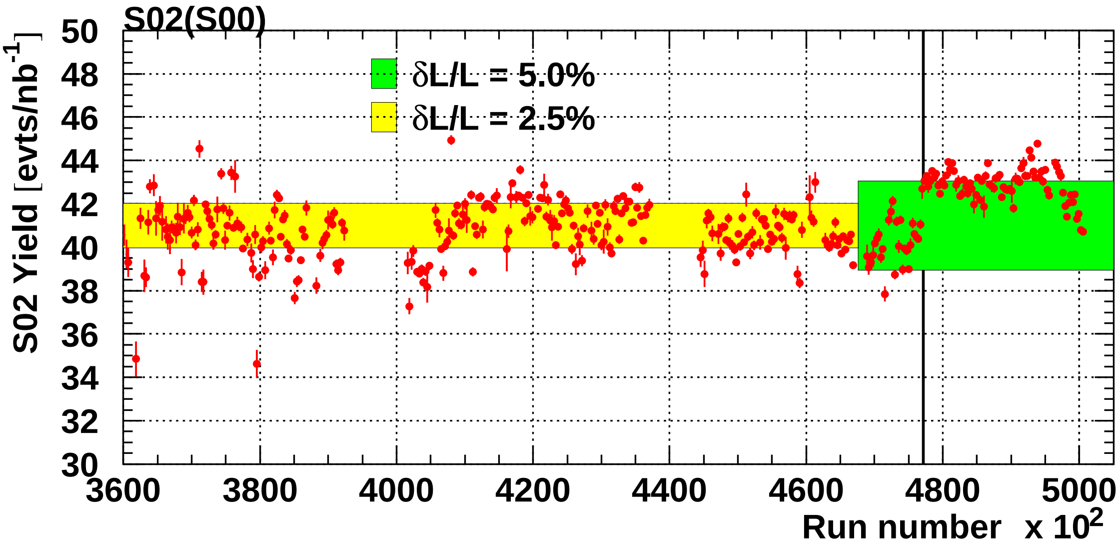

Figure 10.15: *The Luminosity uncertainty is illustrated with shaded bands in the event yield which was measured with the SpaCal for the whole HERAII analysis. The increase of the uncertainty above the run number 477000 is visible. The figure is adopted from [131].*

Branching Ratio

In this analysis D^* mesons which decay in the golden decay channel $D^{*\pm}\rightarrow D^0\pi^\pm \rightarrow K^\pm\pi^\mp\pi^\pm_{slow}$ are studied . The uncertainty on the cross section measurement of the branching ratio of the golden decay channel is taken from [16] and amounts to 1.5%. This uncertainty is a normalization uncertainty like the luminosity.

Chapter 11

Cross Section Results

The total visible D^* photoproduction cross section is measured to be

$$\sigma_{vis}(p \rightarrow eD^*X) = 38.71 \pm 0.76(\mathrm{stat.}) \pm 4.16(\mathrm{sys.})\,\mathrm{nb}.$$

The cross section measurement is restricted to the visible range which is defined with $Q^2 < 2\,\mathrm{GeV}^2$, $100 < W_{\gamma p} < 285\,\mathrm{GeV}$, $|\eta(D^*)| < 1.5$ and $p_T(D^*) > 1.8\,\mathrm{GeV}$.
The cross section was determined with equation 10.1. The data sample was selected with the definition of the selection cuts summarized in table 7.1. The total integrated luminosity of the analyzed data sample amounts to $30.68\,\mathrm{pb}^{-1}$, $68.23\,\mathrm{pb}^{-1}$ and $93.39\,\mathrm{pb}^{-1}$ corresponding to the three subtriggers which have been used in this analysis.
The number of D^* mesons in the visible range which decay in the golden decay channel $D^{*\,\pm} \rightarrow D^0\pi^{\pm}_{slow} \rightarrow K^{\mp}\pi^{\pm}\pi^{\pm}_{slow}$ was extracted by fitting the ΔM distribution and is corrected for detector effects including reconstruction efficiency and acceptance. The kinematic cuts which have been used in this analysis are listed in table 10.1. Further the cross section is corrected for reflections from other D^0 decays. The small contributions of D^* mesons from b quarks have not been subtracted.

The total data cross section can be compared to leading order MC simulations from PYTHIA and CASCADE and to next to leading order calculations from FMNR and GMFVNS provided by [41, 42]. The total cross section prediction from PYTHIA amounts to $42.34\,\mathrm{nb}$ and that from CASCADE to $31.90\,\mathrm{nb}$. The NLO calculations predict $26.37^{+12.63}_{-7.47}\,\mathrm{nb}$ for FMNR and $37.4^{+28.4}_{-13.8}\,\mathrm{nb}$ for GMVFNS both where calculated with HERAPDF1.0 as proton PDF. The uncertainties given for the NLO predictions have been determined with varying the charm mass and the scales, within the values given in table 3.2.
In case of the FMNR prediction the size of the relative theoretical uncertainty of each scale variation was studied in detail. Since the behavior is identical in all variables, here only the scale variation as a function of the transverse momentum of the D^* meson is presented in figure 11.1.

In figure 11.1 a) the charm mass was varied within $m_c = 1.5 \pm 0.2\,\mathrm{GeV}$, in figure 11.1 b) and c) the factorization and renormalization scaled have been varied by a factor of two up and

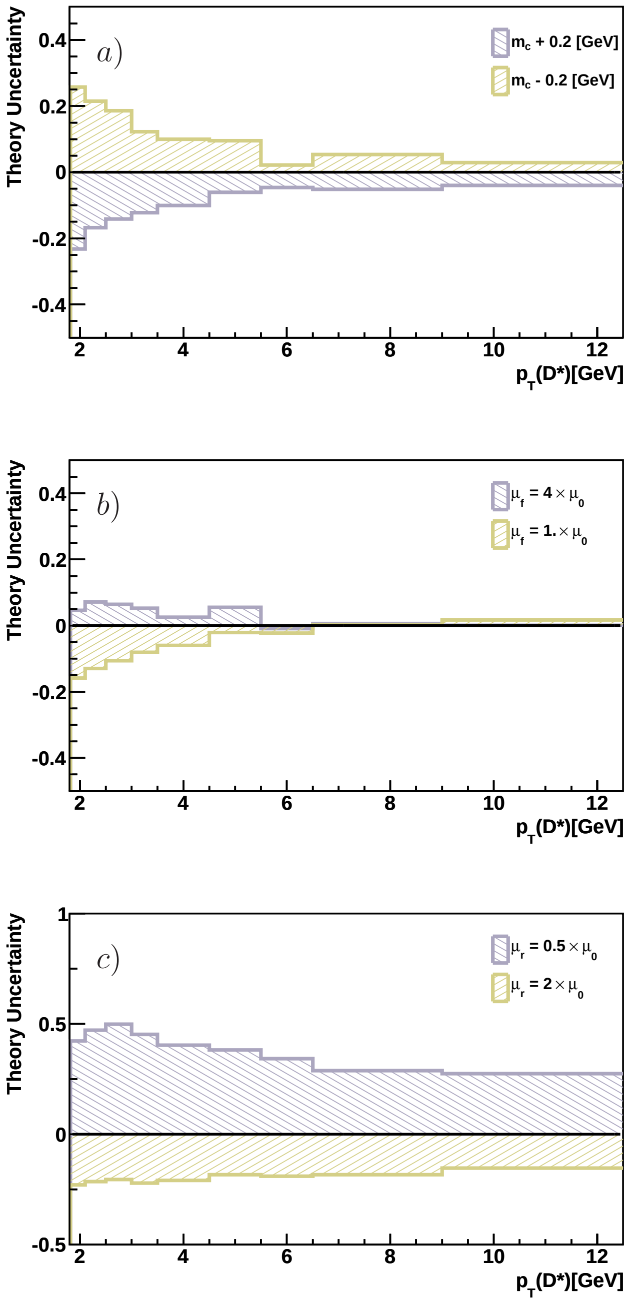

Figure 11.1: *The relative theoretical uncertainties due to the variation of the factorization and the renormalization scale and the charm mass within the FMNR program. The relative size of the variations is similar for all measured quantities, so that here as an example the uncertainties are shown as a function of the transverse momentum of the* D^* *meson.*

down. The charm mass and factorization sale variation are observed to be small, but the renormalization scale variation results in a very large uncertainty. Hence the size of the uncertainty band of the FMNR predictions presented in the following are totally dominated by uncertainty of the renormalization scale.

11.1 Single Differential Cross Sections

The measured single differential cross section as a function of $p_T(D^*)$, $\eta(D^*)$, $W_{\gamma p}$ and $z(D^*)$ are shown in figures 11.2 and 11.3. The cross sections have been corrected with the bin by bin method for detector effects, acceptance and reflections from other D^0 decays. The inner error bar of the data points depicts the statistical errors. The outer error bar is the statistical and systematic uncertainty added in quadrature. The single differential cross section as a function of $p_T(D^*)$ and $\eta(D^*)$ are summarized in table A.1 and as a function of $W_{\gamma p}$ and $z(D^*)$ in table A.2.

In figure 11.2 the data are compared to leading order MC simulations from PYTHIA and CASCADE. The comparison with next to leading order calculations from FMNR and GMVFNS is presented in figures 11.3. The NLO prediction and the band around the central value illustrates the uncertainty band for the calculations which results from the charm mass and scale variations. Because of the huge uncertainty from the renormalization scale variation, see 11.1, the precision of the cross section measurement in all measured quantities presented here is much higher than the accuracy of the calculations from FMNR and GMVFNS. The agreement of the predicted shape and the data shape is studied with the normalized ratio R^{norm} of theory to data which is depicted in the lower part of the figures 11.2 and 11.3. R^{norm} is defined as

$$R^{norm} = \frac{1/\sigma^{calc}_{tot,vis} \cdot \frac{d\sigma^{calc}}{dY}}{1/\sigma^{data}_{tot,vis} \cdot \frac{d\sigma^{data}}{dY}} \tag{11.1}$$

where Y represents the measured variable. For the normalized ratio the value of each variation is normalized with the corresponding total cross section of each variation. An advantage of this normalized ratio is that the uncertainties which leads to change in normalization cancel like the uncertainty of luminosity, the branching ratio and half of the tracking uncertainty of the data.

Cross Section as a Function of $p_T(D^*)$

In figure 11.2 a) the measured single differential cross section in the transverse momentum of the D^* meson is presented in comparison to the leading order predictions. With increasing $p_T(D^*)$ the cross sections falls steeply. A steep decrease towards higher $p_T(D^*)$ is predicted by the LO MCs and the NLO calculations. The leading order MCs PYTHIA and CASCADE give different predictions for $p_T(D^*)$ but none of them predicts a good description of the full $p_T(D^*)$ distribution of the data cross section. A sufficiently good description of the steep increase towards low transverse momenta and the high $p_T(D^*)$ regions is observed for the PYTHIA MC simulation. But here discrepancies to the data cross section occur in the

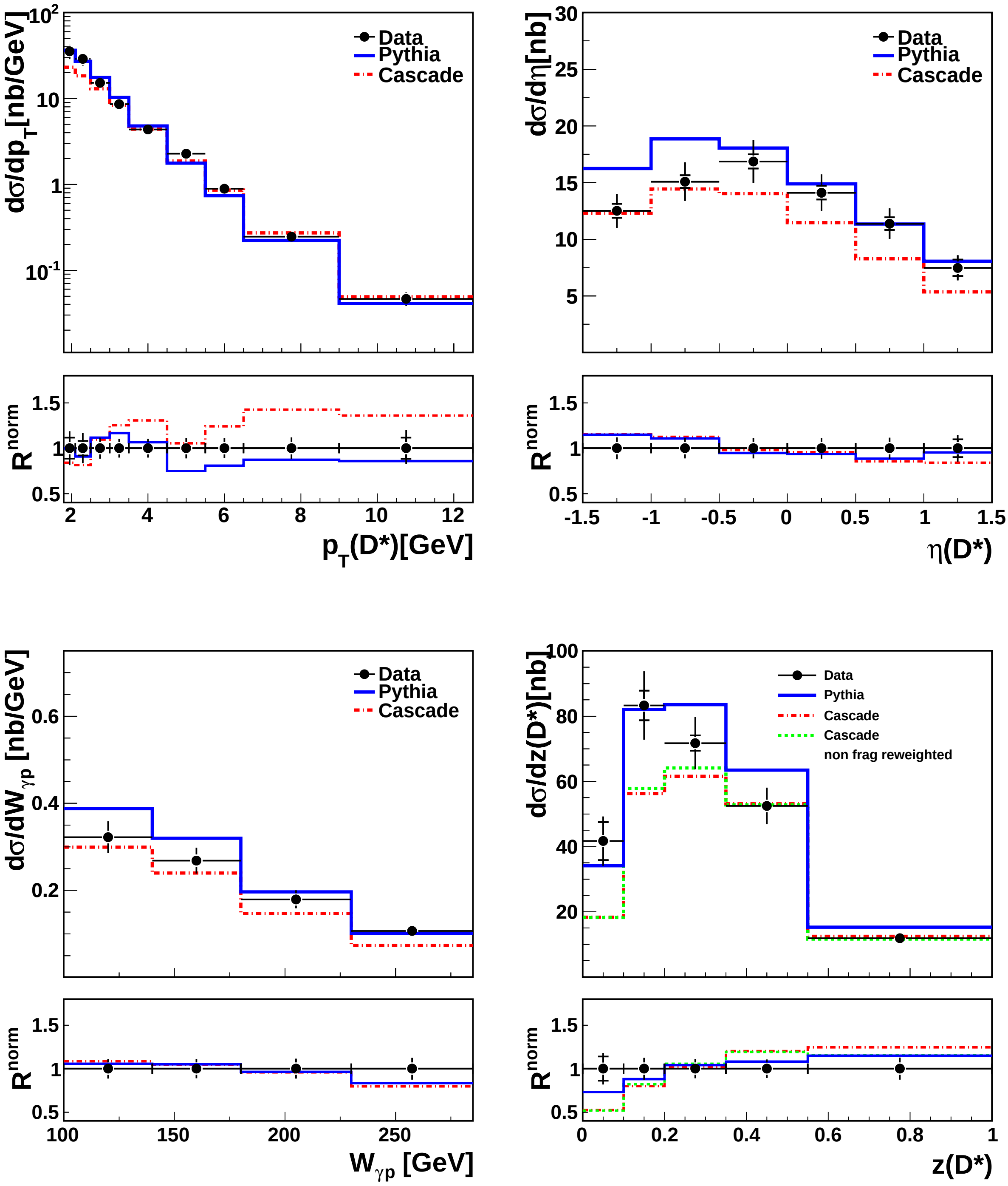

Figure 11.2: *The single differential inclusive D^* cross section in photoproduction in the visible range as a function of $p_T(D^*)$, $\eta(D^*)$, $W_{\gamma p}$, $z(D^*)$. The measurement is compared to PYTHIA and CASCADE MC predictions. The normalized ratio R is shown in the lower part of the figure, too. The CASCADE predictions of the $z(D^*)$ cross section of the CASCADE MC simulation are shown with and without applied fragmentation reweighting. The inner error bar depicts the statistical error and the outer shows the statistical and systematic uncertainty added in quadrature.*

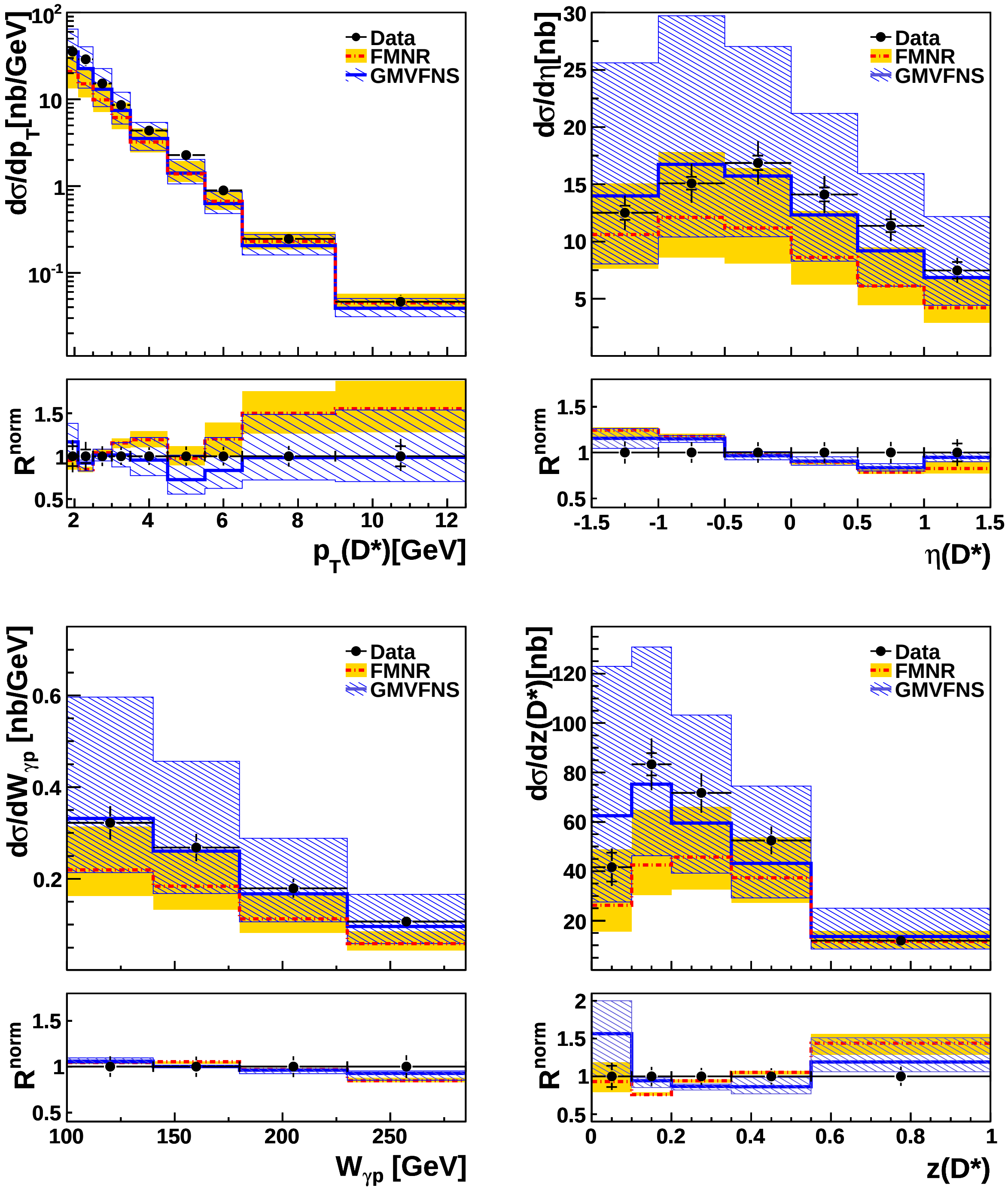

Figure 11.3: *The single differential inclusive* D^* *cross section in photoproduction as a function of* $p_T(D^*)$, $\eta(D^*)$, $W_{\gamma p}$, $z(D^*)$ *in the visible range. The measurement presented in comparison to next to leading order calculations from FMNR and GMVFNS. The normalized ratio* R *is shown in the lower part of the figure, too.*

medium transverse momentum region. The CASCADE MC simulation shows some discrepancies most visible in the upper part of figure 11.2 a) in the low transverse momentum region $1.8 < p_T(D^*) < 2.5\,\mathrm{GeV}$, where the predicted cross section underestimates the data. The differences of PYTHIA and CASCADE in normalization will reoccur in the measurement of the double differential cross sections.
The normalized ratio as a function of $p_T(D^*)$ confirms that the two leading order MCs predict a different cross section behavior as a function of the transverse momentum of the D^* . PYTHIA describes the shape of the data well except in the medium $p_T(D^*)$ region whereas for CASCADE discrepancies over the full distribution are observed.
In addition the cross section in bins of the transverse momentum of the D^* is compared to the next to leading order calculations in figure 11.3 a). The uncertainty band reveals that the uncertainty of the NLO calculations is much larger than the data precision. This is valid for all measured quantities. Within this large uncertainty the cross section measurement as a function of the transverse momentum of the D^* meson is described. The NLO calculation from FMNR predicts at small transverse momenta a much lower cross section normalization than is measured. This has the effect that in all other distribution the normalization is too low. Furthermore the normalized ratio displays that the shape of the cross section distribution has discrepancies to the data shape, which is predicted flatter from FMNR than for data. The GMVFNS calculation predicts the shape of the cross sections sufficiently well.

Cross Section as a Function of $\eta(D^*)$

The single differential cross section as a function of the pseudorapidity of the D^* meson is presented in figure 11.2 b) in comparison to leading order and 11.3 b) in comparison to NLO predictions. The leading order MC simulation from PYTHIA describes the normalization well in the central and forward $\eta(D^*)$ region $-0.5 < \eta(D^*) < 1.5$, but the cross section prediction overestimates the measured cross section in the backward region. In contrast the CASCADE MC is in good agreement with the measurement in the backward region but underestimates the cross section in the other regions.
The normalized ratio illustrates that the shape of the cross section distribution as a function of $\eta(D^*)$ is very similar for both the LO MCs, but different from the data.
Both NLO predictions give a sufficient prediction for the data shape. It is observed that the large normalization uncertainty due to the variation of the renormalization scale leads in this quantity only to small changes in shape. This is also visible for the normalized ratio as a function $W_{\gamma p}$ and $z(D^*)$. The FMNR calculation underestimates the cross section over the full measured $\eta(D^*)$ range which is most visible in the forward region. The other NLO calculation GMVFNS predicts in all bins a higher cross section than the FMNR calculation. In the backward region the data cross section is slightly overestimated whereas it is underestimated in the forward region. The relative contributions in the forward region is too small in all predictions except for the PYTHIA MC simulation.

Cross Section as a Function of $W_{\gamma p}$

In figure 11.2 c) and 11.3 c) the differential cross section as a function of the center of mass energy in the photon proton system is presented. With increasing $W_{\gamma p}$ the distribution is falling. This decrease is expected from the photon flux in the equivalent photon approximation [9–11]. According to equation 2.7 the electron–proton cross section depends on the photon–proton cross section and the photon flux, which is a function of the inelasticity $y = \sqrt{W_{\gamma p}}/s$. With increasing $W_{\gamma p}$ the photon–proton cross section increases slightly, but the photon flux decreases steeply with $W_{\gamma p}$, see equation 2.8. Both leading order MC simulation are not able to describe the normalization of the data. For PYTHIA a overestimation except for the highest $W_{\gamma p}$ bin and for CASCADE an underestimation is observed. Excluding the highest $W_{\gamma p}$ bin the shape of the cross section is in good agreement with the measured shape.

The next to leading order calculation from FMNR undershoots the cross section measurement in the whole measured $W_{\gamma p}$ range but predicts the shape sufficiently well. The cross section measurement is described within the large uncertainties of the GMVFNS prediction. Actually the central value of the GMVFNS calculation depict a very good agreement with the measured $W_{\gamma p}$ distribution and in addition the shape is described as well.

Cross Section as a Function of $z(D^*)$

The measured single differential cross section as function of $z(D^*)$ compared to the predictions is displayed in figure 11.2 d) and figure 11.3 d). None of the leading order MCs gives a sufficiently good description of the data. PYTHIA gives a slightly better prediction of the shape than the CASCADE MC simulation. The biggest deviations are observed in the lowest $z(D^*)$ region. In the data a higher fraction of D^* mesons is produced at small inelasticities than predicted by the leading order MCs.

Further it was expected that the use of a $\hat{s}$ dependent fragmentation leads to a better description of the data but this is not observed.

The next to leading order calculations are able to give a sufficient description of the data within their large uncertainties, although the central values of the predictions show discrepancies in most of the $z(D^*)$ bins. Only in the highest $z(D^*)$ bin the FMNR and GMVFNS calculation are compatible with the size of the extracted cross section. At all lower inelasticities the central value of the FMNR calculation undershoots the measured cross section. The shape of the inelasticity distribution is predicted reasonably well from the FMNR calculation except the highest $z(D^*)$ bin. The central value of the GMVFNS prediction has the largest discrepancy in shape in the lowest $z(D^*)$ bin where it overshoots the data by a lot. At medium $z(D^*)$ overall a good description of the shape is found.

11.2 Double Differential Cross Sections

The single differential cross section measurement as a function of the pseudorapidity of the D^* meson has provided the indication of underestimation of the cross section in the forward region. The dependence between pseudorapidity and the transverse momentum of the D^* meson is further investigated. A double differential measurement in $p_T(D^*)$ and $\eta(D^*)$ is performed. The distribution of the pseudorapidity is studied in three regions of the transverse momentum of the D^* meson. The $p_T(D^*)$ regions correspond to the three different subtriggers used in the present analysis. Because of statistical reasons in the lowest $p_T(D^*)$ region less bins in $\eta(D^*)$ are possible than in the higher $p_T(D^*)$ regions.

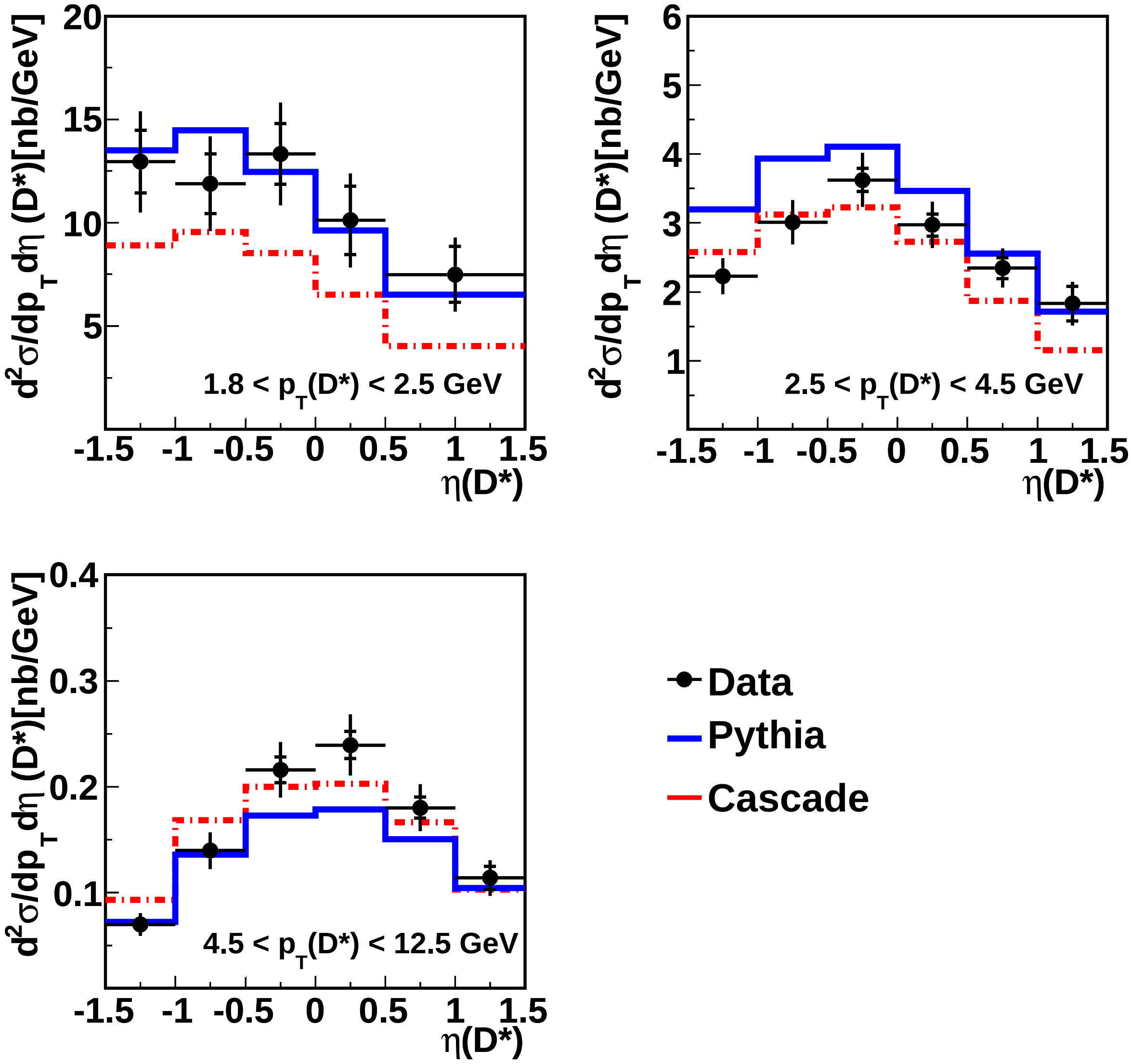

Figure 11.4: *The double differential D^* cross section in photoproduction as a function of $\eta(D^*)$ in three $p_T(D^*)$ regions. The measurement is compared to PYTHIA and CASCADE predictions.*

In figure 11.4 the double differential cross sections is presented together with predictions from the leading order MCs PYTHIA and CASCADE. The different normalization of the MCs PYHTIA and CASCADE in the three $p_T(D^*)$ regions reflect the different $p_T(D^*)$ dependences seen in the single differential cross sections before. In the lowest $p_T(D^*)$ bin the data and the leading order MCs have a falling distribution with rising $\eta(D^*)$. The CASCADE prediction underestimated the measured cross section, whereas the normalization of PYTHIA is compatible with the data. PYTHIA and CASCADE give a reasonable well description of the data shape for the low and medium $p_T(D^*)$ region. Whereas the MCs predict in the highest $p_T(D^*)$ region a too flat shape of the $\eta(D^*)$ distribution and the data show a much more pronounced maximum in the central region. The measured double differential cross sections are summarized in table A.3

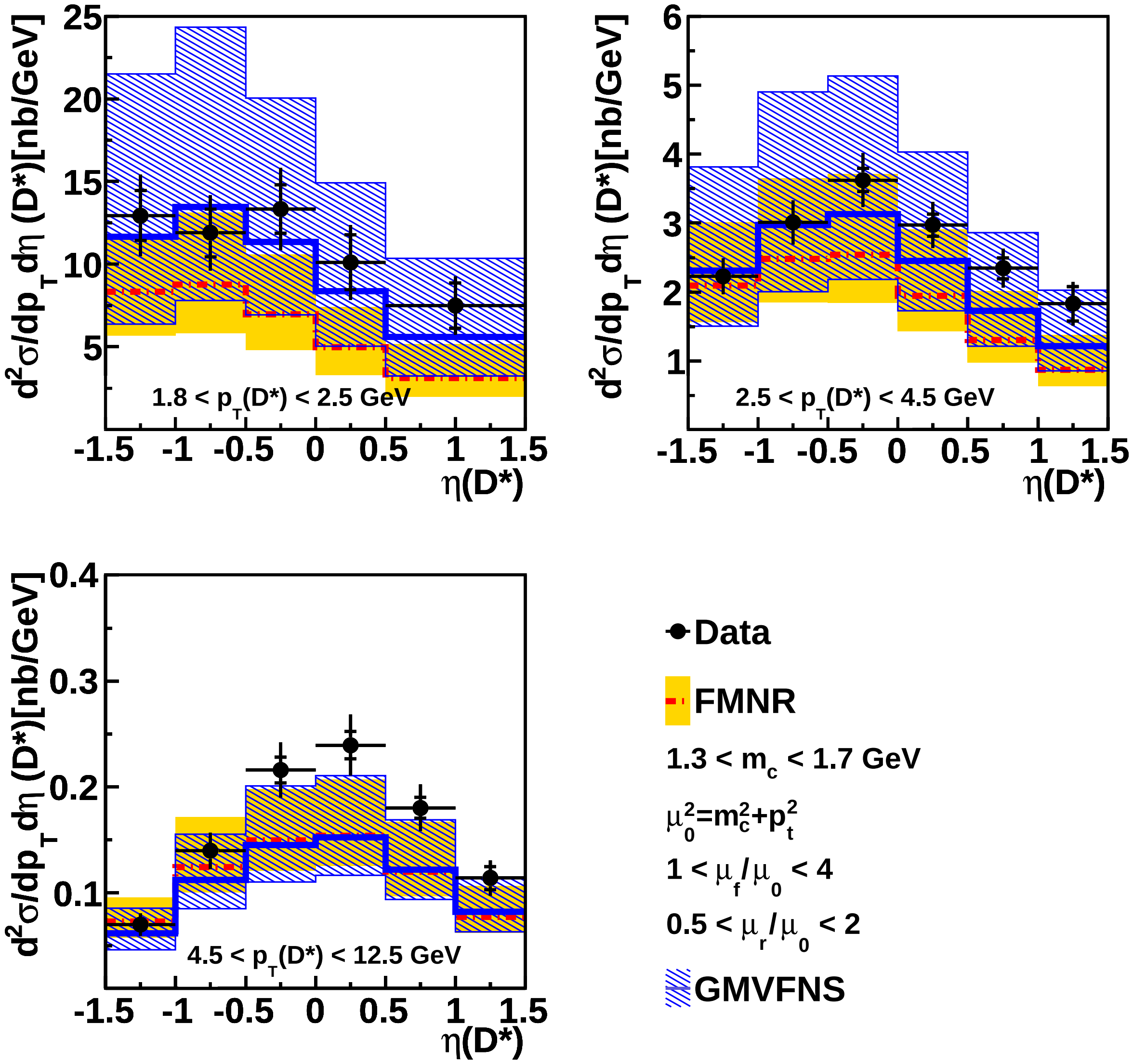

Figure 11.5: *The double differential inclusive D^* cross section in photoproduction as a function of $\eta(D^*)$ in three bins of $p_T(D^*)$. The measurement compared to next to leading order predictions from FMNR and GMVFNS.*

The next to leading order calculations in figure 11.5 show a similar behavior. The lowest $p_T(D^*)$ region shows a falling distribution and the shape is well predicted by the NLO calculations. In the low and medium transverse momentum range the uncertainties of the NLO calculations are much higher than the data precision. The FMNR calculation underestimates over the full $\eta(D^*)$ range the cross section of the data in the lowest transverse momentum region. In the medium $p_T(D^*)$ bin a hint of the underestimation of the cross section in the forward region is found, but the data lies in most cases within the NLO uncertainty. In the low and medium $p_T(D^*)$ regions the GMVFNS calculation agrees well with the data.

In the high $p_T(D^*)$ bin the uncertainties become comparable in size to the data precision. Here all calculations from leading order and NLO predict a similar shape, but the predicted shape does not agree with the shape of the data. The reason for the failure of all predictions in the highest $p_T D^*$ region is not understood yet.

11.3 Comparison with HeraI

The present results are compared to the previous H1 measurement of inclusive D^* cross sections [7]. The analysis covers the data taking period of the years 1999-2000 with a corresponding luminosity of $\mathcal{L} = 51.1\,\mathrm{pb}^{-1}$. The kinematic region was defined with $Q^2 < 0.01\,\mathrm{GeV}^2$ and the inelasticity $0.29 < y < 0.65$. Here the inelasticity was reconstructed as $y = 1 - \frac{E_{e'}}{E_e}$ using the electron beam energy E_e and the positron energy $E_{e'}$ which was measured with the electron tagger. The inelasticity range corresponds to $171 < W_{\gamma p} < 256\,\mathrm{GeV}$. The cut on the transverse momentum of the D^* amounts to $p_T(D^*) \; > 2\,\mathrm{GeV}$.
Since the previous analysis was restricted to a tighter kinematic range, the present analysis must be restricted to this phase space too for comparison. The HERAII cross section is corrected for the different Q^2 regions with the photon flux or with a MC with a Q^2 cut of $Q^2 < 0.01\,\mathrm{GeV}^2$. Both corrections give the same result. The cross section of both analyses have been compared, but do not show sufficient agreement, see figure 11.6.

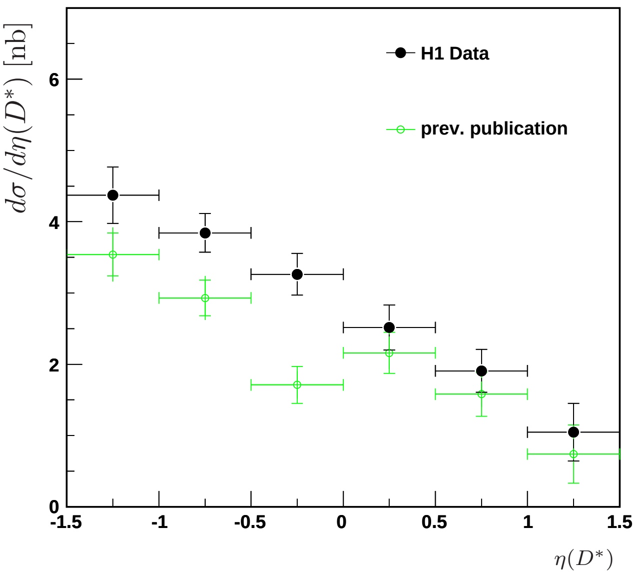

Figure 11.6: *Comparison of the single differential cross sections of the HERAI and HERAII analysis as a function of* $\eta(D^*)$.

Because of that all selection cuts and the fit method of the HeraI analysis are applied to the HERAII data: The background cut in the variable f was applied with the same cut value for both analyses, but the cut on the specific energy loss has to be adjusted to the cut which has been used in the previous publication. The kaon likelihood has to be above 0.002 if the kaon momentum is greater $0.8\,\mathrm{GeV}$ and smaller $2.0\,\mathrm{GeV}$. In all other momentum regions the kaon and pion dE/dx likelihood has to be above 0.01. In addition the signal and background fit has been performed with the same fit functions which have been used in previous measurement. A Gaussian function was used to extract the number of D^* mesons in the signal and a polynomial function to fit the background.
Further the shift of the luminosity measurement which is present after run number 477000 has to be taken into account by shifting up the luminosity of the present measurement by 5%

The comparison of the measured cross sections is presented in figure 11.7 as a function of $p_T(D^*)$ and $\eta(D^*)$. The black points denote the present analysis and the green points the earlier analysis. The error bars illustrate the full statistical and systematical uncertainties on the cross section measurement. Both cross sections are compared to leading order MC predictions from PYTHIA and CASCADE. The two CASCADE predictions shown here have been generated with different fragmentation functions from Peterson and from Bowler.

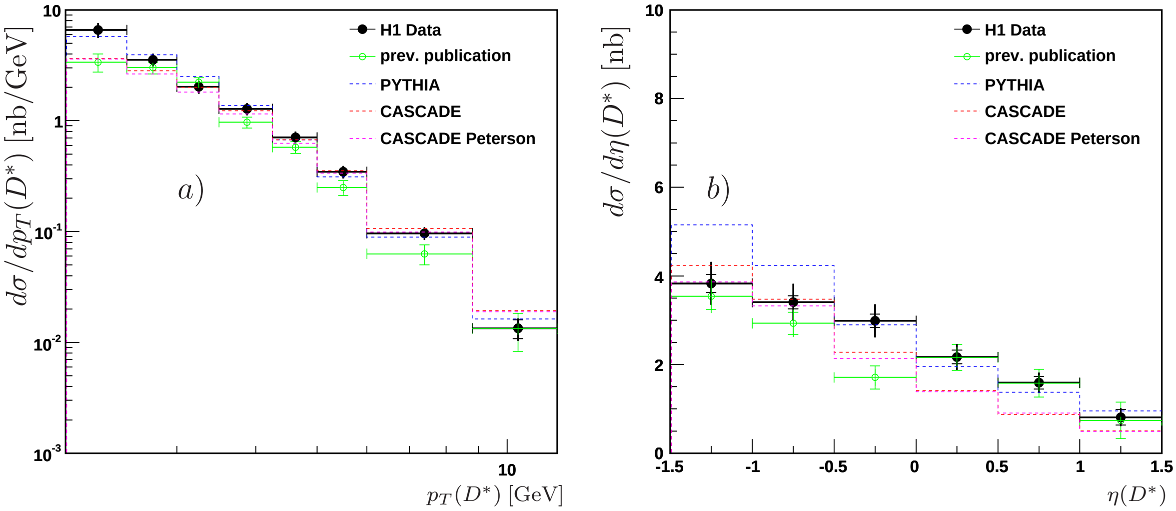

Figure 11.7: *Comparison of the inclusive D^* meson cross section of the present (black points) and previous (green points) H1 analysis. The error bar denotes the systematical and statistical uncertainty. In addition predictions from PYTHIA and CASCADE are presented. CASCADE MC is shown with different fragmentation functions.*

Overall a sufficient agreement is observed. The agreement between the two analyses is observed to be better in the pseudorapidity distribution than in the transverse momentum of the D^* meson. The goodness of the agreement of the cross section value is determined with the integration over the full $p_T(D^*)$ and $\eta(D^*)$ range. The difference in $\eta(D^*)$ between the two

analyses amount to 14%, whereas the differences in $p_T(D^*)$ are around 28%.
However, this large discrepancy of the $p_T(D^*)$ distribution results from the lowest $p_T(D^*)$ bin, where the largest discrepancy is visible. Here the Gaussian signal function fails to fit the ΔM distribution sufficiently. For comparison the statistical uncertainty of the HERAI analysis amounts to 7% and the largest uncertainty of this analysis, the electron tagger acceptance, amounts to 5.8% [7].
The comparison of the total cross sections of the two analyses is depicted in figure 11.8 together with predictions from PYTHIA and CASCADE MC simulations. The total cross section agree within the uncertainties. It is assumed that the differences between the two analyses result from the improper fit function used in the HERA I analysis.

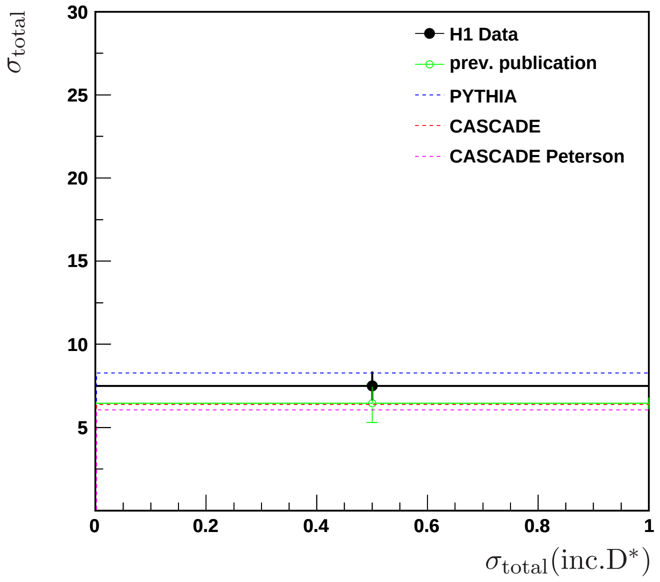

Figure 11.8: *Total cross section of the inclusive D^* cross section measurement of this analysis and of the previous analysis. Predictions from the leading order MC simulations PYTHIA and CASCADE are shown too. CASCADE is generated with two different fragmentation functions.*

Chapter 12

Conclusion

In this thesis the new simulation and calibration of the specific energy loss of particles traversing through the central jet chambers of the H1 detector at HERA was presented. The implementation of the mean specific energy loss simulation in the H1 detector simulation H1SIM was improved. The mean specific energy loss is implemented according to the Bethe–Bloch equation, which depends on the velocity of the particles. The energy loss of particles in an absorber material has a statistical nature and the energy straggling is considered with the usage of four different energy straggling models each valid in a certain range of the thickness of the absorber material. After passing through the full H1 detector response simulation, the specific energy loss of a particle is reconstructed within the software H1REC. The H1 detector response simulation includes several detector effects and the reconstructed specific energy loss needs to be corrected as in data. The necessary corrections and calibrations have been determined in this thesis. The corrected reconstructed energy loss of the MC simulation shows a reasonable agreement with data. The new implementation and correction of the specific energy loss allows particle identification with the specific energy loss measured within the CJC. The specific energy loss distribution after reconstruction requires even after corrections on hit and on track level a slightly different parametrisation as implemented in H1SIM and the resolution has a different dependence on the number of hits in the CJC as determined for data.

The new simulation and calibration is included in the final H1 detector simulation and reconstruction version and is used in particular in this thesis to improve the analysis of D^* mesons in photoproduction. The analysed data sample was recorded during the HERA II run period in the years 2006 and 2007 and corresponds to an integrated luminosity of $30.68\,\mathrm{pb}^{-1}$, $68.23\,\mathrm{pb}^{-1}$, $93.30\,\mathrm{pb}^{-1}$ for the used three subtriggers. In comparison to the previous H1 publication [7] an eight times larger data sample recorded with the H1 experiment was analysed. The D^* mesons have been selected in the golden decay channel $D^* \rightarrow D^0\pi^{\pm}_{slow} \rightarrow K^{\mp}\pi^{\pm}\pi^{\pm}_{slow}$ with a photon virtuality of $Q^2 < 2\,\mathrm{GeV}^2$ and in the range of $100 < W_{\gamma p} < 285\,\mathrm{GeV}$ of the photon–proton center of mass energy. Further restrictions are on the transverse momentum of the D^* meson with $p_T > 1.8\,\mathrm{GeV}$ and on the pseudorapidity of the D^* meson with $\eta(D^*) < |1.5|$. The events have been selected with the Fast Track Trigger of the H1 experiment. The final simulation of the FTT allows to consider the trigger efficiency dependence on different kinematic variables. In this thesis the results of the single and double differential cross section measurement of inclusive D^* mesons in photoproduction have been presented. The single differential cross section have been measured as a function of $p_T(D^*)$, $\eta(D^*)$, $z(D^*)$ and $W_{\gamma p}$. In addition, a double differential cross section measurement was performed in the transverse momentum and the pseudorapidity of the D^* meson. The total D^* meson cross section in the visible region amounts to

$$\sigma_{vis}(p \rightarrow eD^*X) = 38.71 \pm 0.76(\text{stat.}) \pm 4.16(\text{sys.})\text{nb.}$$

The results of the single and double differential cross sections have been compared to leading order QCD models from MC simulation programs of PYTHIA and CASCADE and to next to leading order predictions from FMNR and GMVFNS. In general the predictions describe the data reasonably well. However, two main discrepancies are observed:
The measured single differential cross section as a function of the D^* inelasticity $z(D^*)$ is described by none of the leading order or next to leading order predictions.
Moreover the excess in the highest $p_T(D^*)$ region which was observed by the latest publication of D^* mesons in photoproduction of the ZEUS collaboration [4] is confirmed. All calculations predict a similar $\eta(D^*)$ shape in the highest $p_T(D^*)$ region which differs from the measured shape in the data.

Appendix A

Cross Section Tables

single differential D^* cross section			
$p_T(D^*)$ range [GeV]	$d\sigma/dp_T(D^*)$ [nb/GeV]	stat. [%]	sys. [%]
$1.80 - 2.10$	35.41	± 11.6	$^{+18.8}_{-18.8}$
$2.10 - 2.50$	28.92	± 8.0	$^{+16.6}_{-16.6}$
$2.50 - 3.00$	15.21	± 5.2	$^{+11.6}_{-11.6}$
$3.00 - 3.50$	8.59	± 5.6	$^{+10.3}_{-10.3}$
$3.50 - 4.50$	4.35	± 3.3	$^{+10.4}_{-10.4}$
$4.50 - 5.50$	2.28	± 3.8	$^{+11.3}_{-11.3}$
$5.50 - 6.50$	0.89	± 5.2	$^{+11.0}_{-11.0}$
$6.50 - 9.00$	0.25	± 5.7	$^{+11.9}_{-12.1}$
$9.00 - 12.50$	0.05	± 11.8	$^{+20.1}_{-17.2}$
$\eta(D^*)$ range	$d\sigma/d\eta(D^*)$ [nb]	stat. [%]	sys. [%]
$-1.50 - -1.00$	12.51	± 5.0	$^{+12.0}_{-12.0}$
$-1.00 - -0.50$	15.09	± 3.6	$^{+11.3}_{-11.3}$
$-0.50 - 0.00$	16.86	± 3.7	$^{+11.2}_{-11.2}$
$0.00 - 0.50$	14.10	± 4.3	$^{+11.5}_{-11.5}$
$0.50 - 1.00$	11.38	± 4.9	$^{+11.8}_{-11.8}$
$1.00 - 1.50$	7.48	± 9.8	$^{+14.6}_{-14.7}$

Table A.1: *Summary of the differential cross sections for inclusive D^* production. The central value of the cross section measured in bins of $p_T(D^*)$ and $\eta(D^*)$ with their statistical and systematical uncertainties is shown.*

single differential D^* cross section

$W_{\gamma p}$ range [GeV]	$d\sigma/d(W_{\gamma p})$ [nb/GeV]	stat. [%]	sys. [%]
$100 - 140$	0.32	±3.3	$^{+11.3}_{-11.3}$
$140 - 180$	0.27	±3.2	$^{+11.1}_{-11.1}$
$180 - 230$	0.18	±3.9	$^{+11.5}_{-11.5}$
$230 - 285$	0.11	±5.9	$^{+12.6}_{-12.5}$

$z(D^*)$ range	$d\sigma/d(z(D^*))$ [nb]	stat. [%]	sys. [%]
$0.00 - 0.10$	41.69	±14.0	$^{+18.1}_{-18.2}$
$0.10 - 0.20$	83.27	±5.4	$^{+12.6}_{-12.6}$
$0.20 - 0.35$	71.72	±3.3	$^{+11.1}_{-11.2}$
$0.35 - 0.55$	52.44	±2.6	$^{+10.7}_{-10.7}$
$0.55 - 1.00$	11.90	±3.6	$^{+12.8}_{-12.7}$

Table A.2: *Summary of the differential cross sections for inclusive D^* production. The central value of the cross section in bins of $W_{\gamma p}$ and $z(D^*)$ with their statistical and systematical uncertainties are shown.*

double differential D^* cross section

$1.8 \leq p_T(D^*) < 2.5$ GeV

$\eta(D^*)$ range	$\mathrm{d}^2\sigma/\mathrm{d}\eta\mathrm{d}p_T$ [nb/GeV]	stat. [%]	sys. [%]
$-1.50 - -1.00$	12.95	± 11.73	$^{+18.99}_{-18.97}$
$-1.00 - -0.50$	11.89	± 12.09	$^{+19.23}_{-19.24}$
$-0.50 - 0.00$	13.33	± 11.01	$^{+18.66}_{-18.60}$
$0.00 - 0.50$	10.12	± 16.39	$^{+22.37}_{-22.43}$
$0.50 - 1.50$	7.49	± 18.14	$^{+23.77}_{-23.80}$

$2.5 \leq p_T(D^*) < 4.5$ GeV

$\eta(D^*)$ range	$\mathrm{d}^2\sigma/\mathrm{d}\eta\mathrm{d}p_T$ [nb/GeV]	stat. [%]	sys. [%]
$-1.50 - -1.00$	2.23	± 6.28	$^{+11.73}_{-11.71}$
$-1.00 - -0.50$	3.01	± 4.43	$^{+10.69}_{-10.73}$
$-0.50 - 0.00$	3.62	± 4.61	$^{+10.83}_{-10.81}$
$0.00 - 0.50$	2.97	± 5.32	$^{+11.30}_{-11.29}$
$0.50 - 1.00$	2.34	± 6.64	$^{+12.07}_{-12.07}$
$1.00 - 1.50$	1.83	± 13.76	$^{+17.35}_{-17.33}$

$4.5 \leq p_T(D^*) < 12.5$ GeV

$\eta(D^*)$ range	$\mathrm{d}^2\sigma/\mathrm{d}\eta\mathrm{d}p_T$ [nb/GeV]	stat. [%]	sys. [%]
$-1.50 - -1.00$	0.07	± 10.26	$^{+15.39}_{-15.16}$
$-1.00 - -0.50$	0.14	± 6.02	$^{+12.36}_{-12.31}$
$-0.50 - 0.00$	0.22	± 5.66	$^{+12.14}_{-12.18}$
$0.00 - 0.50$	0.24	± 5.36	$^{+12.12}_{-12.12}$
$0.50 - 1.00$	0.18	± 5.55	$^{+12.17}_{-12.11}$
$1.00 - 1.50$	0.11	± 9.70	$^{+14.73}_{-14.79}$

Table A.3: *Summary of the double differential cross sections for inclusive D^* production. The cross section is determined in bins of $\eta(D^*)$ for three ranges in $p_T(D^*)$ with their statistical and systematical uncertainties*

Appendix B

Database changes due to new H1SIM & H1REC

The new simulation and calibration of the specific energy loss in the CJCs includes changes at the H1 data base. The hit corrections for MC are stored in the data base bank CJQM, see table B.1. The first two parameter are due to the CJC calibration and are taken from the bank CJQC from data. Parameter 5 is due to the CJC staggering. For the correction of the $tan\beta$ dependence of CJC hits the values of parameter 6 to 9 are needed.

CJQM needed in H1SIM for HERAII				
0.044244	0.187218	0.	0.	0.06
0.1474	0.1834	0.1123	0.1591	0.
0.	0.	0.		

Table B.1: *Hit correction parameters of CJQM bank. See text for description.*

The track level corrections for MC simulations of the threshold effect, the $cos\theta$ dependence and the dE/dx resolution are stored in the bank CJDD. A description of the data base bank is presented in table B.2. This correction depend on the CJC gain and the parameters for one constant gain period is shown in table B.3. In total 10 CJDD banks exists on the data base each corresponding to a constant gain period.

TABLE: CJDD, CJC dE/dx Corrections for MC					
Column no.	Parameter name	Format	Min.	Max.	Comments
1	IPAR1	I	-INF	+INF	Parametrization (0: resolutions)
2	IPAR2	I	-INF	+INF	IPAR1=0: 0: Resolution par 1 1: Resolution par 2 IPAR1=3: 0: threshold, gain parameters 1: cos-theta parameters
3	PAR1	F	-INF	+INF	Par 1 (IPAR=0: p resol)
4	PAR2	F	-INF	+INF	Par 2 (IPAR=0: K resol)
5	PAR3	F	-INF	+INF	Par 3 (IPAR=0: pi reso)
6	PAR4	F	-INF	+INF	Par 4 (IPAR=0: mu reso)
7	PAR5	F	-INF	+INF	Par 5 (IPAR=0: e resol)
8	PAR6	F	-INF	+INF	Par 6 (IPAR=0: d resol)
9	PAR7	F	-INF	+INF	Par 7 (IPAR=0: alpha resol)
10	PAR8	F	-INF	+INF	Par 8

Table B.2: *Data base description of the table CJDD.*

CJDD for run range 465088							
$IPAR1 = 0$	$IPAR2 = 0:$						
0.4684	0.4684	0.4684	0.4684	0.4684	0.4684	0.4684	0.
$IPAR1 = 0$	$IPAR2 = 1:$						
0.0055	0.0055	0.0055	0.0055	0.0055	0.0055	0.0055	0.
$IPAR1 = 3$	$IPAR2 = 0:$						
0.	0.	0.	0.213	-1.228	0.	0.	1.395
$IPAR1 = 3$	$IPAR2 = 1:$						
0.9247	-0.0603	0.061	0.137	0.9321	-0.0868	0.1563	0.051

Table B.3: *Example of CJDD parameters.*

Bibliography

[1] C. Kleinwort,“Energy loss measurement with the H1 Central Jet Chamber”, internal H1 note H1-08/08-630, (2008).

[2] M.D. Sauter, “Measurement of Beauty Photoproduction at Threshold Using DI-Electron Events with the H1 Detector at HERA ”, Ph.D. thesis, (2009), Diss. ETH No. 18652, DESY-THESIS-2009-047 (available at http://www-h1.desy.de/publications/theses_list.html).

[3] Andreas W. Jung (H1 Collaboration), “D*+- Meson Production in Deep Inelastic Scattering and Photoproduction with the H1 Detector at HERA”, Proc. of the XVI. International Workshop on Deep-Inelastic Scattering and Related Subjects (2008), London, UK.

[4] J. Breitweg et al. (ZEUS Collaboration), “Measurement of inclusive $D^{*\pm}$and associated di-jet cross sections in photoproduction at HERA”, *Eur. Phys. J.* **C**, **6**, (1999), 67–83, [hep-ex/9807008].

[5] J. Binnewies, B. A. Kniehl and G. Kramer, *Phys. Rev.* **D**, **58**, no. 1, (1998), 014,014. [http://dx.doi.org/10.1103/PhysRevD.58.014014].

[6] M. Cacciari, M. Greco, S. Rolli, A. Tanzini, “Charmed meson fragmentation functions”, *Phys. Rev.* **D**, **55**, (1997), 2736–2740, 10.1103/PhysRevD.55.2736.

[7] A. Aktas *et al.* (H1 Collaboration), “Inclusive $D^{*\pm}$meson cross sections and $D^{*\pm}$jet correlations in photoproduction at HERA”, *Eur. Phys. L.* **C**, **50**, (2007), 251–267, [arXiv:hep-ex/0608042v1].

[8] R. P. Feynman, “Photon-hadron interactions”, Reading 1972, 282.

[9] C. F. von Weizsäcker, “Radiation emitted in collisions of very fast electrons”, *Z. Phys.*, **88**, (1934), 612.

[10] E. J. Williams, “Nature of the high-energy particles of penetrating radiation and status of ionization and radiation formulae”, *Phys. Rev.*, **45**, (1934), 729.

[11] V. M. Budnev, I. F. Ginzburg, G. V. Meledin and V. G. Serbo, “The Two photon particle production mechanism. Physical problems. Applications. Equivalent photon approximation,” *Phys. Rept.*, **15**, (1975), 181.

[12] C. Adloff *et al.* (H1 Collaboration), "Measurement and QCD Analysis of Neutral and Charged Current Cross Sections at HERA ", DESY-03-038, *Eur. Phys. J.* **C**Apr 2003. 54pp. Published in Eur.Phys.J.C, **30**, (2003),1-32, [hep-ex/0304003].

[13] F. D. Aaron *et al.* (H1 Collaboration), "A Precision Measurement of the Inclusive ep Scattering Cross Section at HERA", DESY-09-005, *Eur. Phys. J.* **C**, **64**, (2009), 561-587, [arXiv:0904.3513v2].

[14] F. D. Aaron *et al.* (H1 Collaboration), "Measurement of the Inclusive $e\pm$p Scattering Cross Section at High Inelasticity y and of the Structure Function FL", DESY-10-228, *Eur. Phys. J.* **C**, **71**, (2011),1579, [arXiv:1012.4355].

[15] D. Perkins, "Introduction to High Energy Physics", Cambrige University Press, 4th Edition, (2000).

[16] K. Nakamura *et al.* (Particle Data Group), "Review of particle physics", *J. Phys.* **G**, **37**, (2010), 075021, [http://pdg.lbl.gov].

[17] F. D. Aaron *et al.* (H1 and ZEUS Collaboration), "Combined Measurement and QCD Analysis of the Inclusive ep Scattering Cross Sections at HERA", *JHEP* **1001**, (2010),109, [arXiv:0911.0884].

[18] V. N. Gribov and L. N. Lipatov, "E+ E- Pair Annihilation And Deep Inelastic E P Scattering In Perturbation Theory", *Sov. J. Nucl. Phys.*, **15**, (1972), 675–684, *Yad. Fiz.*, **15**, (1972), 1218–1237.

[19] V. N. Gribov and L. N. Lipatov, "Deep Inelastic E P Scattering In Perturbation Theory", *Sov. J. Nucl. Phys.*, **15**, (1972), 438–450, *Yad. Fiz.*, **15**, (1972), 781–807.

[20] L. N. Lipatov, "The parton model and perturbation theory", *Sov. J. Nucl. Phys.*, **20**, (1975), 94–102, *Yad. Fiz.*, **20**, (1974), 181–198.

[21] Y. L. Dokshitzer, "Calculation Of The Structure Functions For Deep Inelastic Scattering And E+ E- Annihilation By Perturbation Theory In Quantum Chromodynamics. (In Russian)", *Sov. Phys. JETP*, **46**, (1977), 641–653, *Zh. Eksp. Teor. Fiz.*, **73**, (1977), 1216–1240.

[22] G. Altarelli and G. Parisi, "Asymptotic Freedom In Parton Language," *Nucl. Phys.* **B**, **126**, (1977), 298.

[23] I. I. Balitzky and L. N. Lipatov, *Sov. J. Nucl. Phys.*, **28**, (1978), 822-829.

[24] E. A. Kuraev, L. N. Lipatov, and V. S. Fadin, *Sov. Phys. JETP*, **45**, (1977), 199-204.

[25] M. Ciafaloni, "Coherence Effects in Initial Jets at Small q**2 / s", *Nucl. Phys.* **B**, **296**, (1988), 49.

[26] S. Catani, F. Fiorani and G. Marchesini, "QCD Coherence In Initial State Radiation", *Phys. Lett.* **B**,**234**, (1990), 339.

[27] S. Catani, F. Fiorani and G. Marchesini, "Small X Behavior Of Initial State Radiation In Perturbative QCD", *Nucl. Phys.* **B**, **336**, (1990), 18.

[28] G. Marchesini, “QCD coherence in the structure function and associated distributions at small x,” *Nucl. Phys.* **B**, **445** ,(1995), 49 [hep-ph/9412327].

[29] C. Adloff *et al.* (H1 Collaboration), “Measurement and QCD analysis of the neutral and charged current cross sections at HERA”, *Eur. Phys. J.* **C**., **30**, (2003), 1, [hep-ex/0304003].

[30] S. Chekanov *et al.* (ZEUS Collaboration), “High-Q^2 neutral current cross sections in e+ p deep inelastic scattering at $s^{1/2} = 318 - GeV$”, *Phys. Rev.* **D**, **70**, (2004), 052001, [arXiv:hep-ex/0401003v3].

[31] F. D. Aaron *et al.* (H1 Collaboration), ”Three- and Four-jet Production at Low x at HERA”, *Eur. Phys. J.* **C**, **54**, (2008), 389-409, [arXiv:0711.2606v1].

[32] J. Baines *et al.*, “Heavy Quarks: Summary Report”, HERA-LHC Workshop Proceedings, 2007.

[33] C. Adloff *et al.* (H1 Collaboration), “Inclusive D0 and $D^{*\pm}$production in neutral current deep inelastic scattering”, *Z. Phys.* **C**, **72**, (1996), 593, [hep-ex/9607012].

[34] M. L. Mangano and P. Nason, “ Heavy quark multiplicities in gluon jets”, *Phys. Lett.* **B**,**285**, (1992), 160.

[35] J. C. Collins, *Phys. Rev.* **D**, **58**, no. 9, (1998), 094,002, [http//dx.doi.org/10.1103.PhysRevD.58.094002].

[36] S. Frixione, M. L. Mangano, P. Nason and G. Ridolfi, “Heavy-Quark Production”, Adv.Ser.Direct.High Energy Phys., 15, (1998), 609.

[37] S. Frixione, M. L. Mangano, P. Nason and G. Ridolfi, “Total cross sections for heavy flavour production at HERA”, *Phys. Lett.* **D**, **348**, (1995), 633, [hep-ph/9412348].

[38] S. Frixione, P. Nason and G. Ridolfi, “ Differential distributions for heavy flavour production at HERA”, *Nucl. Phys.* **B**, **454**, (1995), 3, [hep-ph/9506226].

[39] M. Cacciari and M. Greco, *Phys. Rev. Lett.*,**73**, no.12, (1994), 1586–1589, [http://dx.doi.org/10.1103/PhysRevLett.73.1586].

[40] W.-K. Tung, S. Kretzer and C. Schmidt, “Open heavy flavour production in QCD: Conceptual framework and implemantation issues”, *J. Phys.***G** , **28**, (2002), 983, [hep-ph/0110247].

[41] G. Kramer and H. Spiesberger, “Inclusive photoproduction of D* mesons with massive charm quarks”, *Eur. Phys. J.* **C**, **38**, (2004) , 309, [hep-ph/0311062].

[42] B. A. Kniehl, “Hadron Production in Hadron Hadron and Lepton Hadron Collisions”, in 14th Topical Conference on Hadron Collider Physics, (2003), [arXiv:hep-ph/0211008v1].

[43] B. Andersson, G. Gustafson, G. Ingelman and T. Sjostrand, ”Parton Fragmentation and String Dynamics“, *Phys. Rept.*, **97**, (1983), 31.

[44] B. Andersson, G. Gustafson and B. Soderberg, *Z. Phys.* **C**, **20**, 317 (1983).

[45] G. Marchesini and B. R. Webber, ”Monte Carlo Simulation of General Hard Processes with Coherent QCD Radiation“, *Nucl. Phys.* **B**, **310**, (1988), 461.

[46] R. D. Field and R. P. Feynman, ” A parametrization of the properties of quark jets“, *Nucl. Phys.* **B**, **136**, (1978), 1.

[47] C. Peterson, D. Schlatter, I. Schmitt and P. M. Zerwas, ”Scaling violations in inclusive e+e- annihilation spectra“, *Phys. Rev.* **D**, **27**, (1983), 105.

[48] M. G. Bowler, “e+ e- Production of Heavy Quarks in the String Modell”, *Z. Phys.* **C11**, (1981), 169.

[49] V. Kartvelishvili, A. Likhoded, and V. Petrov, “On the Fragmentation Functions of Heavy Quarks Into Hadrons”, *Phys. Lett.* **B**, **78**, (1978), 615.

[50] W.-M. Yao *et al.* (Particle Data Group), *J. Phys.* **G**, **33**,(2006), 1, [http://pdg.lbl.gov].

[51] F. D. Aaron *et al.* (H1 Collaboration), ”Study of Charm Fragmentation into $D^{*\pm}$ Mesons in Deep-Inelastic Scattering at HERA”, *Eur. Phys. J.* **C**, **59**, (2009), 589-606, [arXiv:0808.1003v2].

[52] L. Gladilin, ”Charm Hadron Production Fractions“, (1999), [arXiv:hep-ex/9912064v1].

[53] R. Brun *et al.*, *Technical Report CERN-DD/EE-81-1*, (1987),
Application Software Group: “GEANT, detector description and simulation tool,” CERN program library long writeup W5013,
(http://consult.cern.ch/writeup/geant/).

[54] T. Sjöstrand *et al.*, “High-energy-physics event generation with Pythia 6.1”, *Comput. Phys. Commun.*, **135**, (2001), 238.

[55] J. Pumplin, D.R. Stump, J. Huston, H.L. Lai, P. Nadolsky and W.K. Tung, “New Generation of Parton Distributions with Uncertainties from Global QCD Analysis”, *JHEP* **0207**, (2002), 012, [arXiv:hep-ph/0201195v3].

[56] M. Glück, E. Reya and A. Vogt, “Parton Structure Of The Photon Beyond The Leading Order,” *Phys. Rev.* **D**, **45**, (1992), 3986.

[57] M. Glück, E. Reya and A. Vogt, “Photonic Parton Distributions,” *Phys. Rev.* **D**, **46**, (1992), 1973.

[58] H. Jung,“The CCFM Monte Carlo generator CASCADE”, *Comput. Phys. Commun.*, **143**, (2002), 100.

[59] H. Jung, “Un-integrated uPDFs in CCFM,” [arXiv:hep-ph/0411287v1].

[60] F. D. Aaron *et al.*, (H1), “Study of Charm Fragmentation into $D^{*\pm}$ Mesons in Deep-Inelastic Scattering at HERA”, *Eur. Phys. J.* **C59**,(2009), 589, 0808.1003.

[61] K. Lipka and K. Daum, "F2cc from H1 data - Implementation of $\hat{s}$ fragmentation", https://www-h1.desy.de/icgi-h1wiki/moin.cgi/HeavyFlavourWorkingGroup/F2cc_from_D*?action=AttachFile&do=get&target=lipka-080701.pdf, (2008).

[62] W. Marciano, " Flavour thresholds and Lamda in the modified minimal-substraction scheme", *Phys. Rev.*, Volume 29, No. 3.

[63] private communication with Stefano Frixione.

[64] B. A. Kniehl, G. Kramer, I. Schienbein and H. Spiesberger, "Inclusive photoproduction of D*+- mesons at next-to-leading order in the General-Mass Variable-Flavor-Number Scheme," *Eur. Phys. J.* **C**, **62**, (2009), 365, [arXiv:0902.3166].

[65] T. Kneesch, B. A. Kniehl, G. Kramer and I. Schienbein, "Charmed-Meson Fragmentation Functions with Finite-Mass Corrections," *Nucl. Phys.* **B**, **799**, (2008), 34, [arXiv:0712.0481].

[66] P. Aurenche, M. Fontannaz and J. P. Guillet, "New NLO parametrizations of the parton distributions in real photons," EPJC **44**, (2005), 395 [hep-ph/0503259].

[67] H1 *et al.* (H1 Collaboration), H1 Fast Navigator, [http://www-h1.desy.de/general/home/intra_home.html], (2007).

[68] F. D. Aaron *et al.* (H1 Collaboration), "Measurement of the Proton Structure Function F_L at Low x", *Phys. Lett.* **B**, **665**, (2008), 139-146.

[69] I. Abt *et al.* (H1 Collaboration], "The H1 Detector at HERA", *Nucl. Instrum. Methods* **A**, **386**, (1997), 310,
Nucl. Instrum. Methods **A386**, (1997), 348.

[70] R.-D. Appuhn *et al.* (H1 SpaCal Group], "The H1 Lead/Scintillating-Fibre Calorimeter", *Nucl. Instrum. Methods* **A386**, (1997), 397.

[71] D. Pitzl *et al.*, "The H1 silicon vertex detector", *Nucl. Instrum. Methods* **A454**, (2000), 334,
B. List, "The H1 central silicon tracker", *Nucl. Instrum. Methods* **A**, **501**, (2001), 49.

[72] J. Becker *et al.*, "A Vertex trigger based on cylindrical multiwire proportional chambers", *Nucl. Instrum. Methods* **A**, **586**, (2008), 190.

[73] Th. Wolff *et al.*, "A drift chamber track finder for the first level trigger of the H1 experiment," *Nucl. Instrum. Methods* **A**, **323**, (1992), 537.

[74] A. Baird *et al.*,"A fast high resolution track trigger for the H1 experiment", *IEEE Trans. Nucl. Sci.*, **48**, (2001), 1276, [hep-ex/0104010].

[75] D. Meer *et al.*, "A multifunctional processing board for the fast track trigger of the H1 experiment", *IEEE Trans. Nucl. Sci.* , **49**, (2002), 357, [hep-ex/0107010].

[76] V. Blobel, “New developements in track finding and fitting”, [https://www-h1.desy.de/idet/itracker/TrackingGroup/AgnMin/Meet050824/blobel050824.pdf], (2005).

[77] D. Pitzl, H1 Cross Talks 2008, https://www-h1.desy.de/h1/iww/ipublications/crosstalk /2008/talks/xtalk-DPitzl.pdf.

[78] B. Andrieu *et al.* (H1 Calorimeter Group), “Electron / pion separation with the H1 LAr calorimeters”, *Nucl. Instrum. Methods* **A**, **344**, (1994), 492.

[79] B. Andrieu *et al.* (H1 Calorimeter Group), “Beam tests and calibration of the H1 liquid argon calorimeter with electrons”, *Nucl. Instrum. Methods* **A**, **350**, (1994), 57.

[80] T. Nicholls *et al.* (H1 SpaCal Group), “Performance of an electromagnetic lead / scintillating fiber calorimeter for the H1 detector”, *Nucl. Instrum. Methods* **A**, **374**, (1996), 149.

[81] H1 *et al.* (H1 Collaboration)., H1 Luminosity system, https://www-h1.desy.de/h1/www/h1det/lumi/figures/lumi_hera2_setup.html.

[82] F. Sefkow *et al.*, 1994 Nuclear Science Symposium, Norfolk, Virginia, USA, October 1994, IEEE Trans. Nucl. Sci., Vol 42, No. 4, (1994), 900.

[83] J. Naumann, ”Entwicklung und Test der dritten H1-Triggerstufe”, Ph.D. thesis, Universität Dortmund, Germany, (2003), https://www-h1.desy.de/psfiles/theses/h1th-305.ps.

[84] T. Nicholls *et al.*, “Concept, Design and Performance of the Second Level Trigger of the H1 Detector”, IEEE Transactions on Nuclear Science, vol. 45, (1998), 810.

[85] J. C. Bizot *et al.*, ”Strategy studies for the H1 topological L2 trigger (L2TT)”, (1997).

[86] J. K. Köhne *et al.*, *Nucl. Instrum. Methods* **A**, A89, (1997), 128-133.

[87] A. W. Jung, “Inbetriebnahme der dritten Stufe des schnellen Spurtriggers für das H1-Experiment”, [https://www-h1.desy.de/psfiles/thesis/h1th-367.pdf], (2004), Diploma thesis.

[88] A. W. Jung *et al.*, Proc. of the 2007 IEEE NPSS RealTime Conference, ISBN 1-4244-0867-9, (Oct. 2007), IEEE Catalog Number: 07EX1643C.

[89] A. W. Jung, “Measurement of the $D*^{\pm}$ Meson Cross Section and Extraction of the Charm Contribution, $F_2^c(x, Q^2)$, to the Proton Structure in Deep Inelastic ep Scattering with the H1 Detector at HERA”, Ph.D. thesis, Univ. Heidelberg (2009), HD-KIP-09-01, DESY-THESIS-2009-001 (available at http://www-h1.desy.de/publications/theses_list.html).

[90] A. Schöning, (H1),“A fast track trigger for the H1 collaboration”, *Nucl. Instrum. Methods* **A**, **518**, (2004), 542–543.

[91] N. Berger *et al.*, “First results from the first level of the h1 fast track trigger”, In IEEE Nuclear Sience Symposium Conference Record, volume 3, (2004), 1976–1979.

[92] A. Schöning, (H1), “ The Fast Track Trigger at the H1 experiment design concepts and algorithms”, *Nucl. Instrum. Methods* **A**, **566**, (2006), 130–132.

[93] A. W. Jung *et al.*, “First results from the third level of the h1 fast track trigger”, In Proc. 15th IEEE-NPSS Real-Time Conference, pages 1-7, (2007).

[94] V. Karimäki, *Nucl. Instrum. Methods* **A**, **305**, (1991), 187.

[95] A. W. Jung, “FTT L3 Website encoding L3 Trigger Changes”, https://www-h1.desy.de/idet/upgrade/trigger/ftt/level3/l3te_definition.html, (2007).

[96] H. Bethe, “Zur Theorie des Durchgangs schneller Korpuskularstrahlen durch Materie,” *Annalen Phys.*, **5**, (1930), 325.

[97] F. Bloch, “Bremsvermögen von Atomen mit mehreren Elektronen,” *Z. Phys.*, **81**, (1933), 363.

[98] Particle Data Group: “Review of particle physics”, *Eur. Phys. J.* **C**, **15**, (2000), 1,[http://pdg.lbl.gov].

[99] R.M. Sternheimer: “Density effect for the ionisation loss of charged particles,” *Phys. Rev.*, **145**, (1966), 247–250.

[100] M. Hauschild *et al.*, “Particle identification with the OPAL jet chamber,” *Nucl. Instrum. Methods* **A**, **314**, (1992), 74.

[101] J. Steinhart, “Die Messung des totalen $c\bar{c}$ Photoproduktions-Wirkungsquerschnittes durch die Rekonstruktion von Λ_c-Baryonen unter Verwendung der verbesserten $\mathrm{d}E/\mathrm{d}x$-Teilchenidentifikation am H1 Experiment bei HERA,” Ph.D. thesis, Univ. Hamburg, (1999), DESY-THESIS-1999-029.

[102] W. R. Leo, “Techniques for nuclear and particle physics experiments (2nd ed.),” Berlin (Springer), (1994), 378pp.

[103] S. Hancock *et al.*, “Energy loss distributions for single particles and several particles in a thin silicon absorber”, *Nucl. Instrum. Methods* **B**, **1**, (1984), 16.

[104] L. Landau, “On the energy loss of fast particles by ionisation”, *J.Phys. (USSR)*, **8**, (1944), 201–205.

[105] B. List private communication.

[106] Application Software Group, “CERN library,” (http://consult.cern.ch/shortwrups/), (http://wwwinfo.cern.ch/asdoc/cernlib.html).

[107] K. S. Kölbig and B. Schorr, “A program package for the Landau distribution,” *Comp. Phys. Commun.*, **31**, (1984), 97–111.

[108] K. Lassila-Perini and L. Urban, “Energy loss in thin layers in GEANT,” *Nucl. Instrum. Methods* **A**, **362**, (1995), 416.

[109] P. V. Vavilov, “Ionisation losses of high energy heavy particles,” *Zh. Exper. Teor. Fis.*, **32**, (1957), 920–923, translation in *JETP*, **5** (1957) 749–751.

[110] B. List, E. Hennekemper and K. Krüger, ”Energy loss for the CJC“, H1 Tracking Meeting, (12.11.2008),
https://www-h1.desy.de/idet/itracker/TrackingGroup/AgnMin/Meet0811/benno.pdf.

[111] B. Schorr, “Programs for the Landau and Vavilov distributions and corresponding random numbers,” *Comp. Phys. Commun.*, **7**, (1974), 215–224.

[112] A. Rotondi and P. Montagna, “Fast calculation of Vavilov distribution,” *Nucl. Instrum. Methods* **B47**, (1990), 215–223.

[113] picture provided by C. Kleinwort.

[114] I. Lehraus, “Progress in particle identification by ionization sampling,” *Nucl. Instrum. Methods*, **217**, (1983), 43.

[115] F. J. A. Blondel, “Proceedings of the Study of an ep facility for Europe, ed. Amaldi”, DESY 79/48 , (1979).

[116] M.-O. Boenig, “Messung des D^* -Meson-Produktionsquerschnitts in tiefinelastischer Streuung mit dem H1-Experiment”, PhD thesis, University Dortmund, (2007).

[117] J. E. Gaiser, ”Charmonium Spectroscopy from radiative Decays of the J/Ψ and Ψ'^*“, PhD thesis, Stanford University, (1982).

[118] W. Verkerke and D. Kirkby, “The RooFit toolkit for data modeling”, User Manual, (2006), (avaiable at http://roofit.sourceforge.net).

[119] P. Granet *et al.* (French-Soviet Collaboration), “Inclusive Production Cross-Sections of Resonances in 32-GeV/c K+ p Interactions”, *Nucl. Phys.* **B140**, (1978), 389.

[120] K.Urban, “Measurement of Inclusive and DiJet D*-Meson Photoproduction at the H1-Experiment at HERAthe”, Ph.D. thesis, Univ. Heidelberg ,(2009), HD-KIP-09-13, DESY-THESIS-2009-010 (available at http://www-h1.desy.de/publications/theses_list.html).

[121] N. E. Berger, “Measurement of Diffractive ϕ Meson Photoproduction at HERA with the H1 Fast Track Trigger”, Ph.D. thesis, ETH Zürich, (2007), ETHZ-IPP Internal Report 2007-01, (available at http://www-h1.desy.de/publications/theses_list.html).

[122] V. Lendermann, J. Haller, M. Herbst, K. Krüger,H.C. Schultz–Coulon, R. Stamen, “Combining Triggers in HEP data Analysis”, *Nucl. Instrum. Methods* **A**, **604**, (2009), 707, [arXiv:0901.4118v1].

[123] A. Schöning, “FTT L1 Website encoding L1 Trigger Changes”, https://www-h1.desy.de/idet/upgrade/trigger/ftt/level1/l1te_definition.html, (2005).

[124] A. W. Jung, “FTT L2 Website encoding L2 Trigger Changes”, https://www-h1.desy.de/idet/upgrade/trigger/ftt/level2/l2te_definition.html, (2009).

[125] S. Schmitt, “Correction of detector effects: bin-by-bin and unfolding”, H1 internal note, H1-IN-633(03/2011), (2011).

[126] M. Brinkmann, “ D^* production at high Q^2 with the H1 detector”, Ph.D. thesis, Universität Hamburg, (2010), DESY-THESIS-2010-016, (available at http://www-h1.desy.de/publications/theses_list.html).

[127] K. Daum, H1 Tracking Meeting, https://www-h1.desy.de/idet/itracker/TrackingGroup /AgnMin/Meet1001/daum.pdf,(2010).

[128] A. W. Jung, Status Report in H1 Heavy Flavour Meeting, https://www-h1.desy.de/icgi-h1wiki/moin.cgi/HeavyFlavourWorkingGroup/Meeting2010-01-19?action= AttachFile&do=get&target=jung100119.pdf, (2010).

[129] R. Kogler, ”Measurement of Jet Production in Deep-Inelastic *ep* Scattering at HERA“, Ph.D. thesis Univ. Hamburg, (2010), DESY-THESIS-2011-003 , MPP-2010-175.

[130] S. Schmitt, H1 Physics Plenary, 18.11.2010.

[131] S. Schmitt, “Lumi Status Report”, H1 Physics Plenary Meeting, (2008)

Danksagung

Nun bin ich tatsächlich auf der letzten Seite meiner Arbeit angekommen und meine Doktorandenzeit ist fast zu Ende. Ich danke allen, die mich in dieser Zeit unterstützt und motiviert haben. Ein besonderer Dank geht hierbei an meinen Doktorvater Herrn Prof. Dr. Hans–Christian Schultz–Coulon, der es mir ermöglicht hat meine Doktorarbeit in der H1 Kollaboration in Hamburg zu schreiben. Ich danke ihm für seine Motivation und für seine tolle Betreuung auch aus dem 'fernen' Heidelberg.
Herrn Professor André Schöning danke ich für die hilfreichen Diskussionen zur Triggereffizienz des Fast Track Trigger und die Bereitschaft die Zweitkorrektur dieser Arbeit zu übernehmen.
Besonders bedanken möchte ich mich auch bei Frau Katja Krüger, die alle Höhen und Tiefen dieser Arbeit mit mir erlebt hat und immer, ob in einer stressigen H1 Woche oder in ihrem Urlaub, bereit war sich 'seltsame' Plots anzuschauen, zu diskutieren und Lösungsmöglichkeiten zu entwickeln. Ihre Motivation auch in langen Durststrecken hat entscheidend zum Gelingen dieser Arbeit beigetragen.
Herrn Benno List danke ich zuerst für seine Idee im Rahmen dieser Doktorarbeit die Simulation des spezifischen Energieverlust in der CJC zu verbessern und dann dafür mich dabei mit viel Zeit und Wissen unterstützt zu haben. Die Simulation und Kalibration des spezifischen Energieverlust wurde weiter durch die Hinweise und Erfahrungen von Claus Kleinwort unterstützt, dem ich für seine Erklärungen zur CJC danke.
Außerdem möchte ich mich bei Karin Daum und Katerina Lipka aus der H1 'Heavy Flavour' Gruppe für die zahlreichen Ideen und Diskussionen zu meiner Analyse bedanken. Meinen Heidelberger Mit–Doktoranden, Klaus, Andy, Michi, Michel, Hayk und Florian, danke ich für eine tolle Zeit in Hamburg. Ein besonderer Dank geht hierbei an Klaus Urban und Andreas Jung für ihre Hilfe und Bereitschaft mir die Welt der D* Analysen zu erklären. Meinen Heidelberger Bürokollegen Micha, Veit, Felix und Thorsten danke ich für die nette Aufnahme in ihr Büro und dafür mir immer einen Schreibtischplatz freigehalten zu haben.
Schließlich danke ich meiner Familie, die auch in dieser Zeit der wichtigste Rückhalt für mich war.